



A University of Sussex DPhil thesis

Available online via Sussex Research Online:

<http://sro.sussex.ac.uk/>

This thesis is protected by copyright which belongs to the author.

This thesis cannot be reproduced or quoted extensively from without first obtaining permission in writing from the Author

The content must not be changed in any way or sold commercially in any format or medium without the formal permission of the Author

When referring to this work, full bibliographic details including the author, title, awarding institution and date of the thesis must be given

Please visit Sussex Research Online for more information and further details



**The Use of Electric Potential Sensors in
Nuclear Magnetic Resonance and Particle
Detection Applications**

Philip Goulding

Submitted for the degree of Doctor of Philosophy

University of Sussex

September 2014

Declaration

I hereby declare that this thesis has not been and will not be submitted in whole or in part to another University for the award of any other degree.

Signature:

Philip Goulding

UNIVERSITY OF SUSSEX

PHILIP GOULDING, DOCTOR OF PHILOSOPHY

SUMMARY

The work in this thesis extends the applications of the Electric Potential Sensor (EPS) designed by the Sensor Research Technology Centre. Combined is work undertaken in two areas related by their application in security systems: low-field nuclear magnetic resonance with electric-field acquisition, and particle detection for alpha, beta and neutron radiation. In both these areas the EPS is used as to acquire signals.

The first half of the thesis consists of the work undertaken to design a low-field Nuclear Magnetic Resonance spectrometer to detect drugs and explosives. In doing so, the use of the electric field detection technique - patented by Sussex University - is extended to low-field NMR work. The eventual negative results in this field lead first to the design of a simpler proton magnetometer apparatus, a design which would confirm the use of the EPS at low frequencies, and eventually to a change in direction of the research: particle detection. Detailed in this first section are a theoretical explanation of NMR in chapter 2, and a chapter covering the design and testing of the equipment in chapter 3.

The particle detection part of the thesis covers modifications made to the EPS in order to detect particles and experiments conducted to confirm their operation. As in the NMR section, the work is split into a theory chapter which underpins the work, providing context for the experiments chapter. Chapter 5 covers the detection of alpha, beta and neutron radiation and the use of feedback to control the RC time constant of the front end of the sensor.

The work in this thesis concludes negative results in the NMR area, but proves the EPS particle detector as a viable, cost effective alternative to conventional detectors.

Acknowledgements

Over the years I have spent in higher education, my friends and family have kept me company, cheered me laughed with me and endured me. A special mention must go to my Mother and Father, Gill and Frank, for gently buffering my bad moods with unwavering support and secondly to my grandmother Meg, whose kind words of encouragement nurtured confidence in my academic and personal life.

A sincere thank you also to Helen and Robert Prance, my supervisors, who were always willing to give me their time, support and guidance. All the skills and knowledge I accrued along the way I owe in part to them. Martin Nock, for his assistance solving problems and his advice on technical matters, his humour and generosity have made the laboratory a more colourful place in which to work. Anna Barnett, whose advice in the last stages of writing this thesis was invaluable and lastly to all my colleagues in the group, past and present, who have enriched my time at Sussex.

Contents

Contents	v
List of Figures	viii
List of Tables	xi
1 Introduction	1
1.1 Introduction	1
1.1.1 Short History of Nuclear Magnetic Resonance	2
1.1.2 Short History of Particle detection	7
1.1.3 Neutron Detection	9
1.1.4 The Sussex EPS sensor	11
1.2 Thesis Breakdown	13
2 Theory of Magnetic Resonance	15
2.1 Nuclear Paramagnetism	15
2.1.1 Spin and Magnetism	15
2.1.2 Zeeman Splitting	17
2.1.3 Thermal Equilibrium	18
2.1.4 Larmor Precession	19
2.1.5 Free Induction Decay	20
2.1.6 T_1 and T_2 Processes	22
2.1.7 Spin Echoes and the CPMG Sequence	23
2.2 NMR Methods	25
2.2.1 Continuous Wave	26
2.2.2 Proton Magnetometer	27
2.3 The Pulsed NMR Experiment	27
2.3.1 DC Magnet	28
2.3.2 Tank Circuit	29
2.3.3 Amplifiers and Filtering	29
2.3.4 Pulse Sequencing	30
2.3.5 Quadrature Detector	31
2.3.6 FFT Analysis	31
2.4 The EPS in NMR Techniques	32
2.4.1 Noise	33
2.4.2 Low Noise Design	34
2.4.3 Noise Testing	36

3	Design of the NMR Experiment	37
3.1	Overview	38
3.2	Ispin	40
3.3	Tank Circuit	41
3.3.1	Analysis of the Tank Circuit	43
3.4	Tuned Trap	45
3.5	Transformer	47
3.6	Helmholtz Coil	48
3.6.1	Magnetic Field Inhomogeneity	49
3.7	Electrometers	50
3.7.1	Noise	51
3.8	Preliminary Testing	54
3.9	System Testing	54
3.9.1	Averaging Tests	57
3.9.2	Labview Virtual Instruments	57
3.9.3	Proton Magnetometer	59
3.9.4	Results of Proton Magnetometer Tests	61
3.10	Conclusions	63
4	Particle Detection Theory	66
4.1	Overview	66
4.2	Design of Particle Detectors	67
4.3	Charged Particle Detection in Ionisation Chambers	68
4.4	Mechanisms of Ionisation Chambers	71
4.4.1	Ionisation and Excitation	71
4.4.2	Separation of the Ion Pairs	73
4.4.3	Recombination Effects and the Saturation Region	74
4.4.4	Signal in Ionisation Chambers	76
4.4.5	RC Time Constant and Pulse-Mode ionisation Chambers	80
4.4.6	More Factors Affecting the Efficiency of Ionisation Chambers	80
4.5	Mathematical Analysis of the Saturation Region	81
4.5.1	Boag and Wilson's analysis	81
4.5.2	The Value of m	84
4.6	Neutron Detection	84
4.6.1	Scattering and Absorption	85
4.6.2	Behaviour of Fast Neutrons in Converter Layers	87
4.6.3	Determination of Neutron Energy	88
4.7	EPS as a particle detector	88
4.7.1	EPS as an Ionisation Chamber	90
4.7.2	Calculation of Radiation Activity	91
4.7.3	EPS in Neutron Measurements	92
5	Experimental Results	93
5.1	Detection of Ionic Current due to Ionisation of Air	93
5.1.1	Results	94
5.1.2	Analysis	94
5.2	Effect of Altering Grid Voltage	96
5.2.1	Measurements	96

5.2.2	Discussion	98
5.2.3	Comparison of Data to Theory	99
5.3	Rise and Fall Times	101
5.3.1	Testing	101
5.3.2	Results	102
5.4	Direct Detection of Beta Particles	103
5.4.1	Results	104
5.4.2	Analysis	106
5.5	Direct Detection of Alpha Particles	106
5.5.1	Results	108
5.5.2	Discussion	108
5.6	Neutron Detection	111
5.6.1	Results	112
5.6.2	Analysis	113
6	Conclusions	121
6.1	Conclusions	121
6.2	Low Field NMR	121
6.3	Particle Detection	123
6.4	Further Work	126
A	Labview VIs	141
B	Start-Stop Oscillator Design	156

List of Figures

1.1	The NMR experiment	3
1.2	The NMR-mole	5
1.3	The 900 MHz spectrometer at the Universität Düsseldorf	5
1.4	Simple ionisation chamber	8
1.5	The Plessey sensor chip	11
1.6	Generic EPS sensor topology	12
2.1	Quark composition of particles	16
2.2	Zeeman Splitting of particle with $1/2$ spin	18
2.3	Precession of dipole	19
2.4	Free induction decay of the magnetisation vector	21
2.5	NMR spectrum of glycerol sample	24
2.6	The spin echo and CPMG sequence	24
2.7	The spin echo in stages	25
2.8	Apparatus for the continuous wave experiment	26
2.9	Apparatus for the pulsed NMR experiment	28
2.10	The pulsed NMR sequence	30
2.11	The workings of the quadrature detector	32
2.12	Noise in op-amp circuits	34
3.1	Schematic diagram of a custom NMR experiment	39
3.2	Tank circuit schematic	41
3.3	Bode plots of tank circuit	44
3.4	Basic tuned trap schematic	45
3.5	Tuned tuned trap schematic with labelled components	46
3.6	Equivalent reactances loading the tank circuit	47
3.7	Homogeneity of field in the Helmholtz coil	50
3.8	Generic EPS sensor topology	51
3.9	Input capacitances associated with the electrometers	52
3.10	Full electrometer schematic	52
3.11	Power spectral density of OP657 electrometer	54
3.12	Testing the ISpin NMR system	55
3.13	Proton magnetometer experiment	60
3.14	Field inside proton magnetometer coil	61
3.15	Proton magnetometer assembly	62
3.16	Results of proton magnetometer experiment	63
3.17	Results of proton magnetometer experiment	64
4.1	Parallel plate ionisation detector	68

4.2	Operational regions of conventional ion chambers	70
4.3	Bragg curve of charged particles	73
4.4	Distribution of ions in parallel plate ionisation chambers	75
4.5	Weighting field inside particle detector	78
4.6	Charging of the front end RC network by induced charges	79
4.7	Ionisation curve with experimental data	83
4.8	Pulse height spectrum	89
4.9	Modifications to the EPS to allow particle detection	90
5.1	Diagram of experiment to detect ionic current with the EPS	94
5.2	Results of experiment to detect ionic current with the EPS	95
5.3	Output of EPS as a function of grid voltage when irradiated with Americium	97
5.4	Output of EPS as a function of grid voltage when irradiated by Americium - large range	97
5.5	Boag and Wilson's ionisation curve compared with measured data	100
5.6	Experiment to test the effect of AC feedback on rise and fall times of the EPS	101
5.7	Results of experiment to test the effect of AC feedback on rise and fall times of the EPS	102
5.8	Diagram of experimental setup for the direct detection of beta particles	103
5.9	Results of experiment for the direct detection of beta particles	105
5.10	Experimental setup to verify direct detection of alpha particles with the EPS	106
5.11	Results of experiment to verify direct detection of alpha particles with the EPS	107
5.12	Diagram of experimental setup for the direct detection of neutrons	113
5.13	Neutron detection data for Lithium-Flouride and Boron-Carbide converter layers	114
5.14	Neutron detection data for copper and niobium electrodes	115
5.15	Pulse height spectrums for Lithium Fluoride neutron detection data	116
5.16	Close up of Lithium Fluoride pulse height spectrum	119
5.17	Marsh' neutron spectrum for Am-Be source	119
A.1	Front view of the Labview VI designed to control the low-field NMR experiment. Section 1 of 3.	142
A.2	Front view of the Labview VI designed to control the low-field NMR experiment. Section 2 of 3.	143
A.3	Front view of the Labview VI designed to control the low-field NMR experiment. Section 3 of 3.	144
A.4	Top shell of the Labview VI created to control the NMR experiment. Sections 1 to 6 are pictured in the next pages.	145
A.5	Top shell of the Labview VI created to control the NMR experiment. Sections 1 of 6	146
A.6	Top shell of the Labview VI created to control the NMR experiment. Sections 2 of 6	147
A.7	Top shell of the Labview VI created to control the NMR experiment. Sections 3 of 6	148
A.8	Top shell of the Labview VI created to control the NMR experiment. Sections 4 of 6	149
A.9	Top shell of the Labview VI created to control the NMR experiment. Sections 5 of 6	150

A.10	Top shell of the Labview VI created to control the NMR experiment. Sections 6 of 6	151
A.11	Inner shell of the Labview VI designed to control the low-field NMR experiment. 1 and 2 are shown in the following pages	152
A.12	Inner shell of the Labview VI designed to control the low-field NMR experiment. Section 1 of 2	153
A.13	Inner shell of the Labview VI designed to control the low-field NMR experiment. Section 2 of 2	154
A.14	Most inner shell of the Labview VI designed to control the low-field NMR experiment.	155
B.1	Start stop oscillator program. Built on an Atmel328p to test the function of the ispin averaging.	157
B.2	Start stop oscillator schematic. Built on an Atmel328p to test the function of the ispin averaging.	158

List of Tables

2.1	Quark properties	16
3.1	Proton Magnetometer Coil Measurements	60
4.1	Ionisation energy for gasses	72
4.2	Neutron cross sections	86
5.1	Converter layer properties	111
5.2	Neutron Counts	118
5.3	Neutron Source peaks	118

Chapter 1

Introduction

1.1 Introduction

On-going advances in manufacturing processes precipitate the design of ever higher specification integrated circuits. The advent of field effect transistor operational amplifiers in particular has led to the design of the Electric Potential Sensor (EPS) by researchers at Sussex University Sensor Technology Research Centre. The work collected in this thesis is part of the continual research into the design and applications of the EPS, research which produces tools for measurement in such disparate fields as medical, security and forensics.

This thesis aims to address two aspects of security systems, although the research contained may have implications in many fields besides. The first half of the thesis covers work undertaken to use the EPS sensor to detect low-field NMR signals. NMR has for decades been an important tool in drug detection; providing a method by which the molecular structure of compounds can be analysed. In recent years interest in a lower energy, more portable variant of the NMR technique - low-field NMR - has grown, with much research directed toward the discovery of drugs and explosives. A key factor in the design of such systems is preservation of the inherently low signal levels. The EPS sensor has previously been shown to detect high-field NMR signals with higher signal-to-noise ratio than traditional magnetic detection systems. This thesis aims to extend this

research, addressing the design of a low-field NMR system with EPS electrometer signal acquisition.

The original mandate of the thesis was to investigate NMR systems for the detection of drugs and explosives, although unsuccessful results in this field ultimately lead to the more fruitful research of the EPS as a particle detector. The need for modern, rugged, low-cost particle detectors is - along with NMR detection systems - prescient in the field of security, recent world events having tightened security in public spaces. The second part of this thesis proves the EPS to behave as a particle detector capable of detecting alpha, beta and neutron radiation. The performance of the EPS makes it a viable alternative to other more complicated, expensive systems and provides the basis for much further work on the subject.

1.1.1 Short History of Nuclear Magnetic Resonance

Nuclear Magnetic Resonance (NMR) is a phenomenon which enables non-destructive testing of materials. NMR is used to analyse and identify materials and forms the basis of Magnetic Resonance Imaging, a technique in which data from many NMR scans are combined to image the inside of complex samples, most often used in medical imaging and diagnosis (magnetic resonance imaging - MRI). The process of NMR is analogous to the technique of finding the acoustic dispersion characteristics of a room. A stimulus is provided to give the system energy and then the response is captured. In the case of acoustic dispersion an impulse is provided by a transducer and the reflections are recorded in the time that follows. In NMR the stimulus and response are less tangible: electromagnetic waves - rather than sound - excite a sample and are measured in response.

Figure 1.1 shows the basic NMR set-up. A sample sits inside a coil which forms part of a resonant circuit. The coil and the sample sit inside the field from a static DC magnet. An RF field is applied by pulsing the resonant coil at the resonant frequency. The pulses are timed to produce the free induction decay response where the magnetic moments inside the sample align and precess in unison. This magnetic oscillation is detected with a magnetic pick-up coil, often the same coil as used to apply the RF energy.

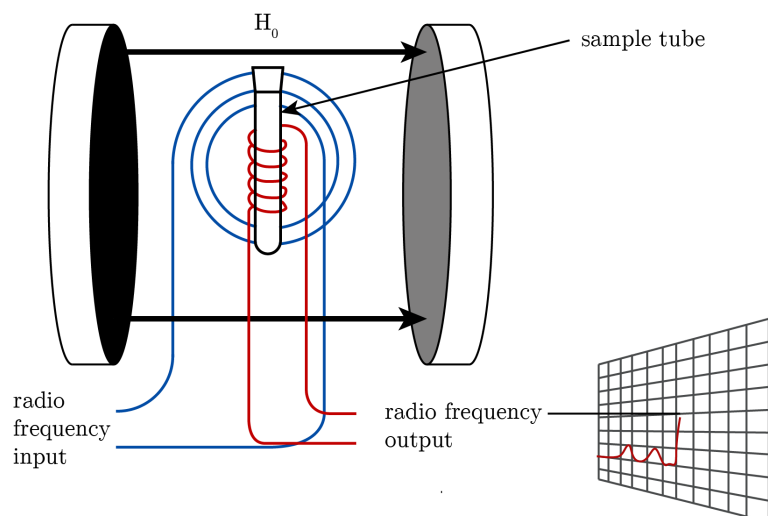


FIGURE 1.1: The NMR experiment. The sample tube sits inside the magnetic field from a static magnet and excited by the energy through the coil. This induces an oscillating magnetic moment in the sample.

Much of the pioneering work on NMR was conducted in the early 20th century, when techniques were devised to test the properties of atomic particles. Quantum theory was in its infancy and providing promising explanations of absorption and emission phenomena defined by Kirchoff and Planck. The technique came about incrementally; the first experiments to explore the properties of charge and magnetism in particles prompted techniques to verify the existence of nuclear magnetic moments [1]. In 1936 Gorter and Broer [2] conducted a (non-functioning) experiment into the resonance property of particles with spin in magnetic fields. In 1936 Rabi became the first person to observe the phenomenon of nuclear magnetic resonance [3]. Purcell, Torrey and Pound [4] detail a functional continuous wave experiment the same year. The continuous wave experiment detects changes in the magnetic susceptibility of a sample. The signal-to-noise ratio of the obtained signal is very low and it cannot be used to study the decay effects (T_1 and T_2 effects) associated with free induction decay (FID) signals - the signals studied in modern day NMR.

In 1946 Bloch [5],[6] and Purcell [4] outlined the basis of the modern day pulsed NMR technique, which differs from the continuous wave experiment in that a short pulse of RF energy is used to precipitate an oscillating magnetic moment inside the sample (an FID), observed directly by a magnetic pick-up coil. Also outlined in these Bloch papers were the mathematics which have been used extensively to interpret NMR. The pulsed NMR experiment uses a permanent magnet to provide a static magnetic field, causing nuclear

magnetic moments to align. The resultant moment is very small and much effort is taken in the design of the equipment and how the experiment is carried out to preserve the tiny signals. The pulsed NMR technique improves the signal-to-noise ratio and allows FIDs to be analysed via the Fourier transform to determine samples by their frequency spectrum. It was some time before this practice was common-place: the poor field homogeneity of magnets prohibited detailed spectra and it would also be some time before enough data was gathered to recognise NMR signatures. By the 1950's techniques were being developed to enable determination of the T_1 and T_2 times - these terms are given to various factors which affect the decay time of FIDs and are indicative of properties of the sample. The spin echo described by Hahn [7] is used to re-phase the NMR signal, separating T_1 and T_2 effects and mitigating the effect of poor magnetic homogeneity somewhat, leading to better signal-to-noise ratio.

The later half of the 20th century refined the NMR equipment significantly while the technique changed little. The use of NMR became a mainstay in testing of materials, capable of determining the chemical composition of samples without the need to reduce them with chemicals. The advances made in the field were related to the performance of the equipment used - improvements in magnet homogeneity gave rise to highly sensitive NMR systems capable of obtaining detailed chemical spectra in materials, and MRI - a technique where many NMR scans are performed with complex perturbations in the applied field, producing information about the distribution of isotopes but also their position in a sample. As of 2014, MRI is the foremost medical diagnostic technique. Both NMR and MRI are incredibly useful tools but high quality NMR relies on exquisitely sensitive measurement equipment, super-cooled magnets and extensive calibration and as such is reserved for well funded institutions with experienced staff on hand to manage them. Research in the field continues to drive NMR magnets to further extremes of homogeneity - producing ever stronger, more homogeneous magnets capable of producing more detailed spectra and better signal-to-noise ratio (One example of a high field spectrometer is that belonging to the centre for high-field NMR, having a 1 GHz frequency, corresponding to a magnetic field strength of 23.5 T [8]) but also sees funding devoted to the study of other particles such as quadrupoles and electrons [9],[10]. What drives all of these techniques is the desire to gather information about ever finer spatial resolution and more difficult to

measure phenomena.



FIGURE 1.2: The NMR-mole, an example of a small scale NMR system that can be used for portable NMR work. [11]



FIGURE 1.3: The 900 MHz spectrometer at the Universität Düsseldorf. An example of one of the larger NMR spectrometers that require special facilities and constant maintenance. [12]

The work in the first part of this thesis concerning NMR is a far cry from the high-tech engineering needed to produce late 20th century NMR spectrometers. Instead, the work takes a different approach - attempting to measure NMR spectra in low fields. The technology used in comparison to laboratory spectrometers is minimal and lightweight but produces

far inferior signals (the inherent problem with low-field NMR is that of signal-to-noise ratio, which declines with the DC magnetic field). Contrast the 900 MHz spectrometer at the Universität Düsseldorf requiring a specially designed facility and full time staff to house and maintain it (figure 1.3), with the NMR-mole - a 3.3 MHz, a low resolution NMR system approximately 25 cm wide (figure 1.2) [11]. The NMRmole cannot hope to provide as detailed spectra or as high signal-to-noise ratio, but can offer portable medical diagnostics [13]. In recent years, research into so called "miniaturised" NMR has grown considerably [14] and typically focuses on the design of portable or low field magnets, or of high performance NMR and MRI in low-field strengths. Typically those researching the former will use magnetic pick-up coils for signal detection[15][16], whereas those researching latter will use cryogenically cooled quantum interference devices (SQUIDs) in laboratory conditions [17],[18],[19]. However, this is not the only way to improve the signal-to-noise ratio of the signal. Aydin [20] showed that the detection of free induction decay signal was possible by detecting the electric field associated with the time changing magnetic field, the resulting signal having improved signal-to-noise ratio. The method is patented by Sussex University on behalf of the Sensor Technology Research group. The Electric Potential Sensor (EPS) gives better signal-to-noise ratio than magnetic pick-up coils without the prohibitive cost and practical considerations of super cooled devices. Consequently it might become possible to conduct low-field strength experiments with the electric field detection technique and obtain better signals than are traditionally possible, paving the way for improved mobile NMR systems capable of on site tests to detect drugs or explosives [21], [22].

The research in this thesis focuses on expanding the work started by Aydin. As the EPS sensor is proven to enable better signal-to-noise ratio than that of traditional magnetic field detection, this will enable better low-field NMR systems. The additional use of pulse sequences such as the CPMG sequence can be used to mitigate the effects of low-field homogeneity. A low-field NMR system that combine both electric field acquisition with pulse sequencing is hitherto unknown. The original mandate of the thesis was as a method of detection for explosives in hidden cavities.

1.1.2 Short History of Particle detection

This thesis also covers the design and testing of modifications made to the EPS to tailor it to the purpose of particle detection. This design branches into two areas: a charged particle detector similar to an ionisation chamber and a neutron detector which utilises a converter layer to convert neutrons into charged particles which are then collected.

Like NMR the roots of particle detection can be traced back to the late 1800's and early 1900's, when much research was devoted to understanding radiation and the structure and properties of atoms. Some of the earliest ionisation chambers were built in the late 1800's by the Curies during their research into radioactive materials. Ionisation chambers are the most common type of particle detector and many of the modern types of detector can be understood by extending their principle of operation. Figure 1.4 shows a schematic ion chamber, incident particles ionise air molecules between the plates creating electrons and positively charged ions. A voltage applied to the cathode produces a field between it and the anode which separates the positive and negative charges, moving them in either direction. The movement of electrons causes a voltage over R and C which is measured and the rate of incident particles inferred.

The theoretical basis for gas particle detectors was laid by Röntgen who discovered in 1895 that air conducts electricity when irradiated with x-rays. J.J. Thompson investigated and analysed the conduction of ions in gasses, forming the theory on which much later analysis is based [23]. Early ionisation chambers were used along with fluorescent screens, radioactive plates and gold leaf electrosopes. Visually based detection systems, i.e. the spinthariscopes and cloud chamber used mediums which interacted with particles, enabling researchers to see the arrival of individual particles but relied on the counts being recorded manually. In contrast ionisation chambers are used to measure high rates of irradiation, but were not used to detect the arrival of individual particles until much later. Later detectors adapted the ionisation chamber but used high voltages, such as the Geiger-Müller detector, designed in 1928, in which the voltage applied between the plates is much higher and causes gas amplification. This causes a very high output at the arrival of a particle, which enables individual counts to be recorded. Such detectors cannot be used for high rates of irradiation and cannot distinguish between the energy of incident particles.

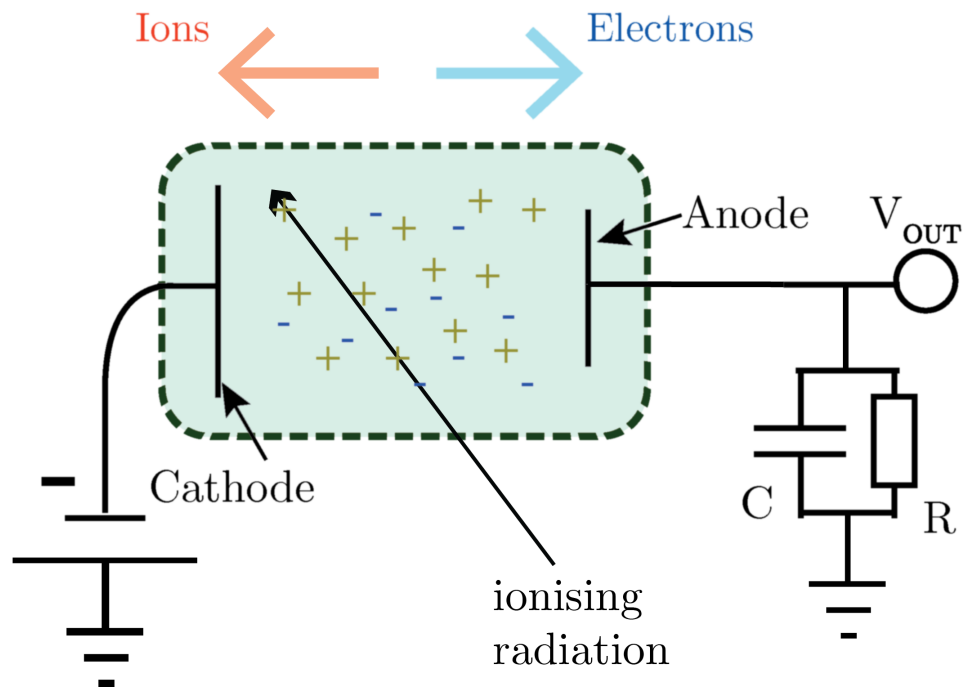


FIGURE 1.4: Simple ionisation chamber. The dashed box represents an enclosed region of gas over which an electric field is created by voltage applied between the plates. Charges move toward either plate and are measured by an electrometer attached to V_{out} .

The proportional detector, working in a voltage region between the saturation and Geiger-Müller regions, was designed in the late 40's. It is less sensitive than the Geiger Müller, able to distinguish between particles but still largely unsuitable for high irradiation. These two types of detector are referred to as "pulse mode" detectors, whereas ionisation detectors are referred to as "current mode" or "integrating" detectors. Pulse mode detectors will detect individual particles - pulses - of radiation. Current mode detectors produce a DC level proportional to the rate of ionisation inside the chamber. Pulse mode counters might be used for detection and determination of particles, current mode ionisation chambers to determine energy and activity of a source. One notable development in pulse mode detector design is the Frish grid (1944 [24]). This grid enables better measurement of individual particles by shielding the detection equipment from the initial ionising event, and is also used with solid state detectors to achieve the same purpose [25].

Ionisation chambers do appear in modern research [26], along with proportional and Geiger-Müller detectors, [27] [28], as they present a robust and often cost-effective way of measuring radiation for general measurement devices. When measuring high energy

radiation, ionisation chambers are often used as they are more robust than modern solid state detectors -

"In contrast to solid state detectors gas-ionization detectors are not affected by radiation damage due to heavy ion bombardment"[29]

Hence gas based ionisation detectors are frequently used [30], for measuring radiotherapy beams [31], for x-ray absorption spectroscopy [32], or to measure beam losses in particle accelerators [33]. Depending on the application, chambers might employ gridded designs. According to Steinmeyer -

"G-M (Geiger-Müller) detectors can be found in virtually all facilities where radioactive materials are used, from commercial nuclear reactors to hospitals and from research institutions to machine shops"[34]

The theory which underpins particle detection is also covered in this thesis (see chapter 4). Thompson's 1899 paper [23] describes the equations which govern the movement of ions through air. They are insoluble without some simplification and there are numerous attempts at deriving solutions with simplifications or by addressing only part of the behaviour, notably by Mie [35], Seeliger [36] and Townsend [37]. Boag and Wilson's analysis of the behaviour of ionisation chambers [38] is a more recent paper freely available in English that examines the behaviour of parallel plate ionisation chambers at high ionisation intensity. Sprinkle and Tate's 1965 paper [39] discusses the same phenomenon in cylindrical and circular chambers. Further work by Rosen and George [40] and Bielajew [41] focuses on an explicit solution for the entire saturation curve, neglecting the space term of Thompson's paper. Boag and Wilson's paper ignores the space charge term and focuses on the saturation region.

1.1.3 Neutron Detection

Neutrons have no charge and consequently neutron radiation does not ionise. Various detector designs - recoil detectors, Bonner spheres, scintillation devices - all work in roughly the same manner as the ionisation chamber by converting the energy of the incident particle into a different type of particle which is then measured. In neutron detectors the

converter material must be specially chosen to stand the most chance of interacting with an incident neutron, a process called "absorption". Absorption occurs when a neutron collides with other particles, creating a variety of decay products. Usually gamma rays, charged particles and neutrons are created in the process of absorption and there are different detectors which operate by detecting different particles - scintillation devices detect the gamma products whilst recoil detectors work by detecting charged particles. Techniques to maximise the collection of the particles are often used - reflectors for scintillation detectors or a field applied over the converter to repel or attract charged particles.

The first documented scintillation device was the Spintaroscope, documented in 1903 by William Crookes [42] and consisted of a zinc sulphide screen which fluoresced in response to radium decay. In 1941 Krebs described the photon-tube scintillation counter which would electronically count scintillations [43], automating a previously laborious process, and in 1944 Curran and Baker invented the first photomultiplier scintillation counter [44]. These two designs became the standard types of scintillation detectors for decades. Modern scintillation devices often use solid converter layers, and might combine a converter layer with charge-coupled detectors (CCDs) [45] or photo-diodes [46]. Liquid [47] and crystal scintillators [48] are often used.

The research in this thesis details a type of detector most similar to a proton recoil detector - these detectors measure the positive charge created when neutrons are absorbed. Other types of proton recoil or charge based neutron detectors are documented in scientific literature [49], [50] but scintillation detectors are far more common.

The EPS particle detector - using either a grid to separate charges or a converter layer for neutron detection - is a simple, rugged design that does not use large amount of expensive converter materials and has no moving parts. The sensor offers control over the capacitance and can be engineered to fit into very small spaces, requiring only enough space for an electrode, while the accompanying sensor technology has been integrated to fit on to a chip measuring only 1 cm² (see figure 1.5).

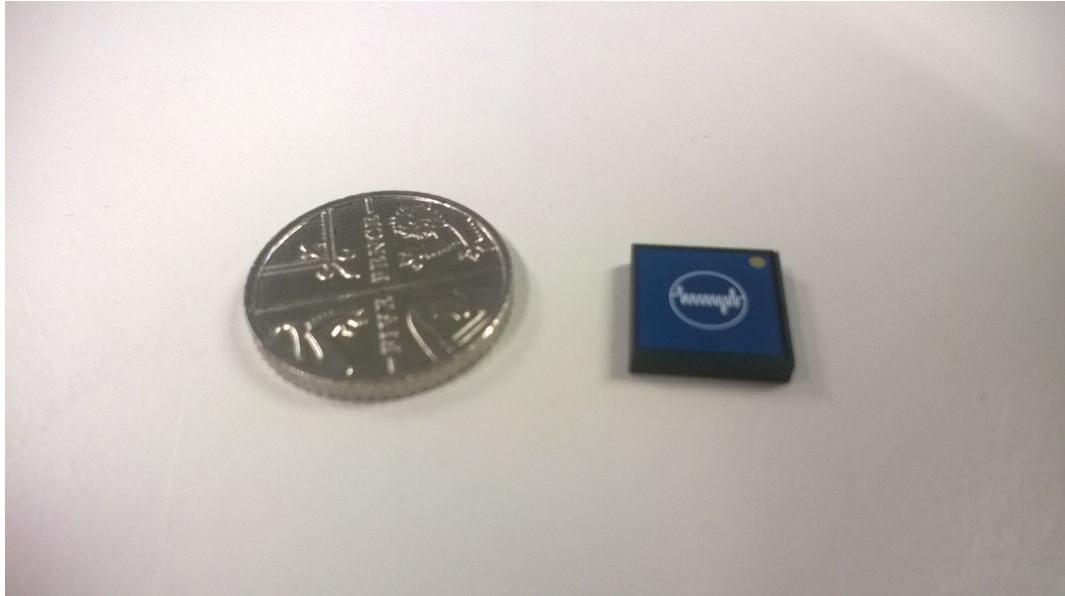


FIGURE 1.5: Plessey semiconductor have integrated the EPS into a 1 cm^2 chip, shown here on the right compared to a five pence piece. Sensors using the EPS technology can be made very small and robust.

1.1.4 The Sussex EPS sensor

The Sussex Electric Potential Sensor was designed to replace the existing sensors used in the Sussex Sensor Technology Research Centre - which were super-cooled quantum interference devices (SQUIDs). These SQUIDs detect very small magnetic fields but require cryogenic cooling and are therefore very expensive. The first EPS sensors were designed to detect the same signals but by detecting the electric field associated with time changing magnetic fields. EPS sensors can also detect DC fields, replacing the need for devices like the field mill [51]. Since its inception the EPS design has been adapted mainly to detecting physiological signals such as ECG [52], EEG [53], EMG [54] and EOG [55]; materials testing [56]; nuclear magnetic resonance [20]; quadrupole resonance [57]; and static charge sensing [58].

The EPS is often regarded as a perfect voltmeter - measuring voltages whilst drawing effectively no current from the source. This enables the measurement of signals that would otherwise be loaded and attenuated by the measurement equipment. Figure 1.6 shows a schematic interpretation of the design of the EPS. The sensor is most commonly AC coupled via a high impedance electrode, but further high input impedance is made possible

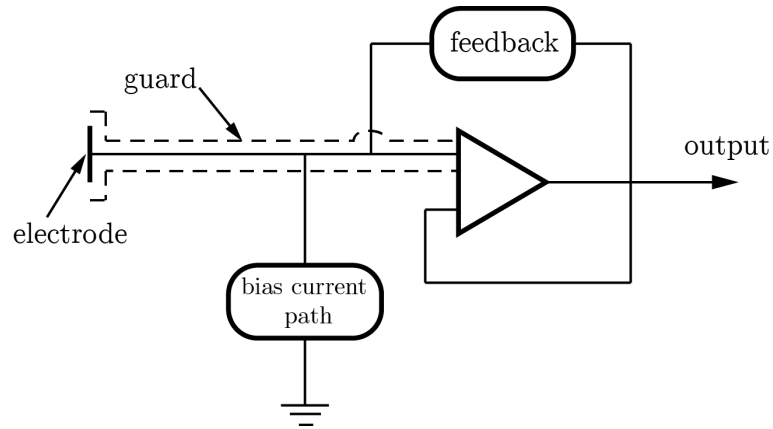


FIGURE 1.6: Generic EPS sensor topology. A bias current path is provided by a high resistance path to ground. Positive feedback is used to reduce the capacitance of the front-end, which prevents attenuation of signals.

by FET input op-amps which require very small bias currents (some of the sensors designed in this thesis use the OP657 op amp which requires only 2 pA of bias current [59]). A bias resistor is provided to ensure this bias condition is met and also that charge deposited on the front end of the sensor has a discharge path, making the EPS stable where many other electrometers would rail. The resistor can be in the order of tera ohms. As well as careful choice of op-amp, bootstrapping is used to boost the impedance of the front: the voltage over the input impedance is minimised by applying positive feedback, making the input resistor seem even higher in resistance without interfering with the bias current. The second feedback technique involves the use of neutralisation: as the sensor is often capacitively coupled, the coupling of the electrode forms a capacitor which in turn forms a capacitive voltage divider with the parasitic capacitance of the sensor. Sensors must be designed using op-amps with small input capacitance, but further reduction of the parasitic input capacitance inherent in the circuit layout is minimised by applying feedback to minimise the capacitance (neutralisation) [60].

Previous research with the EPS has typically focused on the detection of electric fields [61],[62],[55] but as a particle detector the EPS detects the presence of charged particles on the front end of the sensor. This is made possible by the extremely high resistance ($\approx 20 \text{ G}\Omega$) of the front end. It is the exceptional sensitivity to charge that makes the sensor useful for detecting what is referred to as ionic currents - currents created by the movement of free electrons. These are currents are typically very small ($\approx \text{fA}$) and require very

high impedance equipment ($> G\Omega$) in order to detect them. The feedback techniques traditionally used in the EPS can be used to broaden the bandwidth of the sensor, which enables the detection of individual particles.

1.2 Thesis Breakdown

- *Introduction* - this introduction.
- *Theory of Magnetic Resonance* - theory which underpins the NMR experiment is discussed. This chapter is included to provide the relevant theory upon which the NMR section of this thesis is based. Consequently much of the information concerns the classical physical interpretation of the experiment. The chapter discusses the existence of magnetic moments on an atomic level, then explains how these create paramagnetic moments and how these moments are manipulated to create a precessing macroscopic moment. The chapter discusses the various different techniques that exist for studying nuclear paramagnetism and gives a short appraisal of their various benefits and shortcomings before discussing the pulsed NMR technique - the technique used in this thesis - and outlining the various different parts of the experiment and what they do. This leads to the introduction of NMR spectroscopy being introduced. The last section in the chapter gives a short explanation of the particular design considerations for the EPS sensors designed in the NMR research.
- *Design of the NMR experiment* - This chapter discusses the custom made apparatus designed to capture NMR signals with the EPS in low-field conditions. Traditionally magnetic field detection is used to capture these signals, here the experiment designed uses both magnetic pick up coils, first at 1.84 MHz on a previously existing system, then at 48.5 kHz to test the operation of the system, before the patented electric field detection technique is implemented. The work by Aydin [20] is used as a basis for the design. It was intended that both of these methods could then be compared for differences in signal to noise ratio, but eventually the low-field NMR work was not successful. The chapter is composed of design criteria and measurements of the various parts of the system - setup built to test low-field NMR uses a Helmholtz coil to apply the static DC field, relevant signal amplification to drive the

system, a custom made tank circuit with and provisions for damping and operating the system via a commercially available, computer operated computer system - the ISpin NMR. A short section on the successful system testing at high frequency with single pulse and CPMG pulse sequences is included. Discussions of the potential reasons for the ultimate failure of the system are made.

- *Particle Detection Theory* - Theory of particle detection, this chapter serves to underpin the experimental design of the particle detection experiments. The basis for the research is the design of an EPS modification which allows the operation of the chamber in the same fashion as a traditional ionisation chamber. The operation of the ionisation chamber is covered extensively, as well as the mechanisms of conduction in gasses. It covers the different types of detector behaviour and secondly Boag and Wilson's theoretical treatment of saturation. Also outlined is the theory of neutron detection, which relies on the selection of appropriate converter materials to convert incident neutron energy to charge. The mechanisms which allow this conversion to take place and the criterion for selection of a converter materials are discussed. The chapter ends with a short section detailing the particular design requirements for the EPS as particle detectors.
- *Experimental Design and Results* - This chapter documents the design, results and analysis of experiments conducted to characterise the behaviour of the EPS as a particle detector. Detailed in this chapter is the direct detection of alpha and beta particles, detection of ionic current produced by alpha particles in air (analogous to a traditional ionisation chamber), manipulation of rise and fall times by the use of feedback and neutron detection conducted with appropriate converter layers on the front electrode. The analysis of the results introduces some new theoretical ground in order to explain some of the anomalous effects observed in the results.
- *Conclusions* - Conclusions of the thesis. Reflections on the work undertaken and scientific method, and idea for new areas of research.

Chapter 2

Theory of Magnetic Resonance

This chapter will explain the theory behind the NMR technique and the reasons for its occurrence, in order to provide a basis for the next chapter which covers design of an NMR experiment. Also covered is the pulse sequencing often used in NMR spectroscopy, brief explanations of the continuous wave experiment, the proton magnetometer and a comprehensive breakdown of the pulsed NMR technique which discusses each part of the experiment and Fourier transform NMR. The chapter ends with a section outlining the design criteria for EPS electrometers in the e-field NMR experiment.

2.1 Nuclear Paramagnetism

NMR is the interaction of an externally applied signal with nuclei which exhibit paramagnetism in the presence of a magnetic field.

2.1.1 Spin and Magnetism

Magnetism is created by the movement of particles with charge. When electrons conduct through a wire a magnetic field is created, but fields are also created by the intrinsic property of spin which causes particles to have some angular momentum. Spin is a fundamental property of quarks, the subatomic building blocks that constitute particles and the amount of spin all types of quarks have is defined as $1/2$ (table 2.1 [63]) shows different

quark properties). Different quarks pair together to form larger particles like the proton and neutron, and spins or charges can be cancelled out. Figure 2.1 shows how quarks pair to form the proton and the neutron (the electron is a fundamental particle) - all have spin, but the neutron has no charge. When neutrons and protons combine to form nuclei their spins often cancel due to the way they pair together. Consequently, around a third of isotopes have non-zero spin [64, p.2].

TABLE 2.1: Quark properties

Quark	Spin	Charge	Mass
up	1/2	+2/3	1.7-3.3 MeV
down	1/2	-1/3	4.1-5.8 MeV
charm	1/2	+2/3	1270 MeV
strange	1/2	-1/3	101 MeV
top	1/2	+2/3	127 GeV
bottom	1/2	-1/3	4.19 GeV

Most forms of magnetism are created by the orbits of electrons, but nuclei that have non-zero net spin also create small fields - where the moment of the nuclei is parallel to an applied field. Nuclear paramagnetism is the name given to this effect. Paramagnetic fields are much smaller than those associated with electrons and differentiating between them and other forms of magnetism is difficult. However, the NMR technique uses electromagnetic radiation to interact directly with paramagnetic moments generated by the nuclei of spin-exhibiting isotopes.

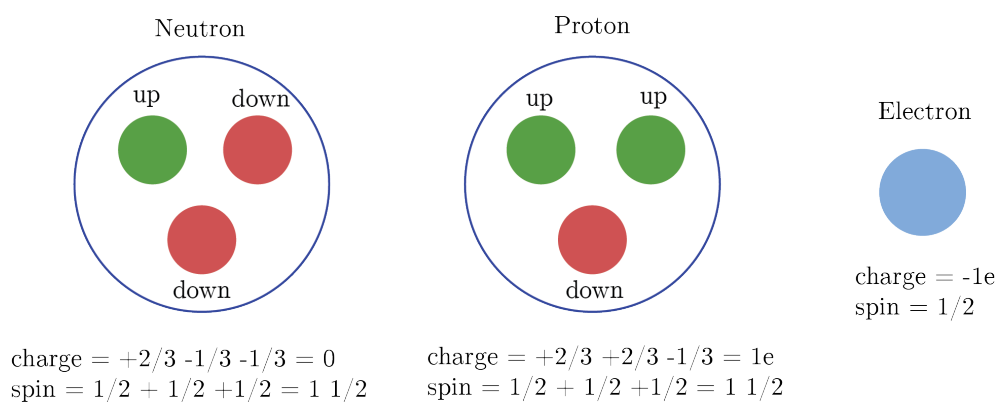


FIGURE 2.1: Quark composition and characteristics of the neutron, proton and electron. NMR can be performed on elements with both charge and spin. [63]

Spin refers to the angular momentum of a particle or nucleus: a body with spin is turning

around a central axis. In a body with non zero spin, finite charge and mass create a magnetic moment defined by a vector μ (see fig 2.3) and angular momentum, parallel with μ . The magnetic moment is measured in nuclear magnetons and is given by

$$\mu = g \frac{e}{2m} I \quad (2.1)$$

I = spin (dimensionless)

e = charge of the particle (eV)

g = nuclear g factor (dimensionless)

m = mass of particle (kg)

2.1.2 Zeeman Splitting

If a particle with spin of $\frac{1}{2}$ - and a magnetic moment μ - is placed in a magnetic field \mathbf{B} , there are two different positions which the particle can assume: either μ is parallel to, or anti-parallel to \mathbf{B} . The orientation that it will take depends on the energy of the particle. The lowest energy position is with μ parallel to \mathbf{B} : +1/2 orientation, and the highest energy orientation is when μ and \mathbf{B} are anti parallel: -1/2 orientation. If the particle is to change orientation, it needs to either lose or gain energy. The energy difference between these two states is proportional to \mathbf{B} . Particles often have spin numbers of greater than 1/2, which affects the amount of states the particle can be in. If the spin is I , the amount of possible orientations in relation to spin number is

$$2I + 1 \quad (2.2)$$

Therefore when a nucleus with $I=1\frac{1}{2}$ is influenced by \mathbf{B} there are 4 orientations it may take. As a field B_0 is increased, a particle with a spin of 1/2 which sits inside that field aligns itself in one of two states: 1/2 or -1/2 (represented by the two dashed lines) this can be thought of as whether the particle is aligned or opposed to the field and depends on how much energy the particle has. This quantisation of states is called Zeeman splitting and

is pictured in figure 2.2. The difference in the energy levels is equal to

$$h\nu = \frac{-\mu B_0}{I} \quad (2.3)$$

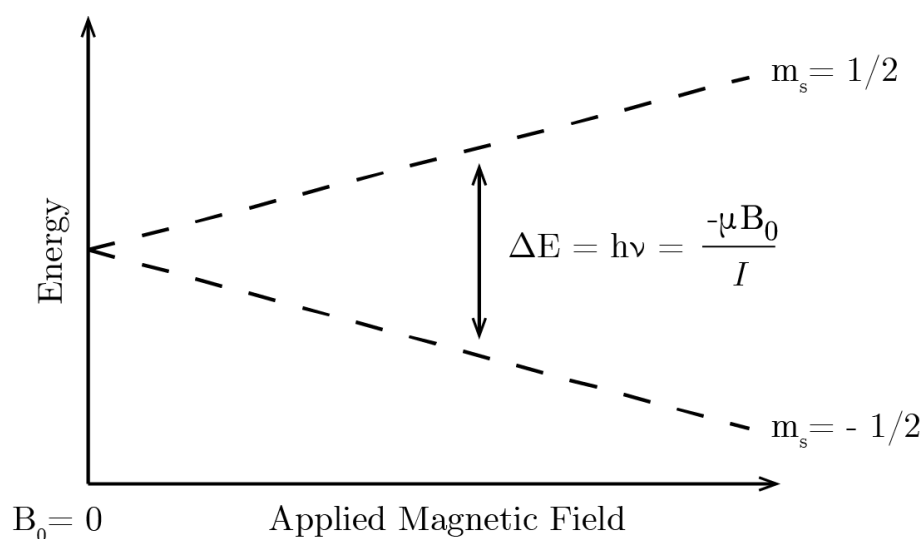


FIGURE 2.2: Zeeman effect - splitting of a particle with spin 1/2 in the presence of a magnetic field. As the field B_0 increases, so does the energy difference between the states. [65]

2.1.3 Thermal Equilibrium

A substance at room temperature has thermodynamic energy. Consequently when a material with spin exhibiting nuclei sits in a magnetic field the distribution of spin states is roughly equal parallel and anti-parallel, but there is a very small imbalance between them. If the temperature were reduced to absolute zero all spin states would be in the low energy position producing an overall magnetic moment. As the strength of the magnet increases the energy needed to produce an anti parallel state also rises and the number of moments in the low energy state increases, giving rise to a net magnetic moment. For a sample at room temperature the vector \mathbf{M}_0 is used to refer to the thermal equilibrium paramagnetic moment.

2.1.4 Larmor Precession

The most common example of precession is the motion of a spinning top when it starts to fall: the angular momentum vector rotates around the field of gravity vector. This happens because gravity presents torque on the top but the angular momentum resists the force of gravity, slowing the return of the top to equilibrium. Precession is important in NMR as

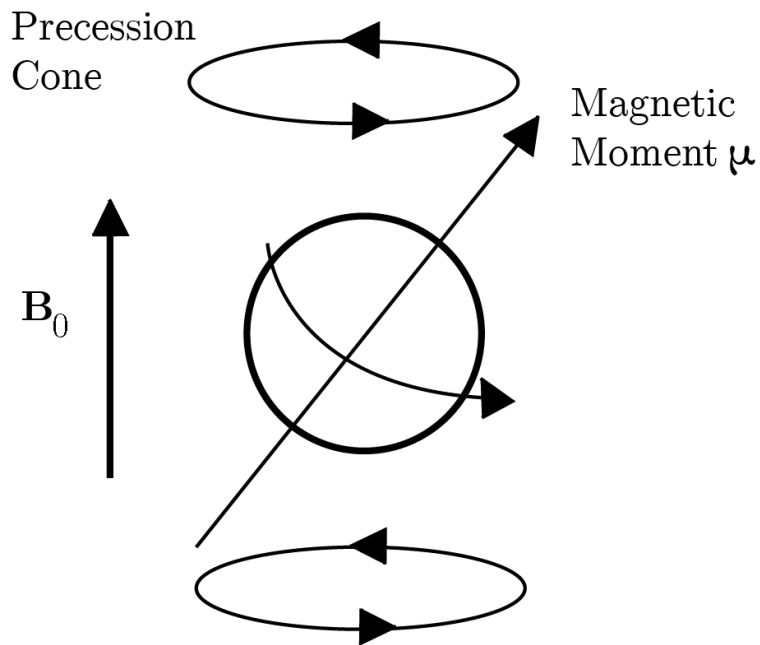


FIGURE 2.3: Precession of particle around the field B_0 creating magnetic dipole. The magnetic moment μ precesses around an externally applied field denoted by B_0 , forming a precession cone [66]

the same effect occurs on a microscopic level to the individual nuclear magnetic moments μ precessing in an applied field, and on a macroscopic level - electromagnetic radiation is used to supply torque to the magnetic moment μ , causing it to precess.

An applied field B_0 will produce an angular acceleration on the magnetic moment, causing it to precess. The orientation of the central axis around which the body spins moves in a circle when precessing, this is the precession cone or precession orbit (see figure 2.3). The magnetic moment and angular momentum vectors point in the same direction, but rotate around the field at an angle. The ratio of these two vectors is called the gyromagnetic ratio γ .

$$\gamma = \mu / I\hbar \quad (2.4)$$

This ratio determines an important factor in NMR: the frequency of precession, or the Larmor frequency. From equation 2.1 particles with a larger mass have lower magnetic moment hence the angular acceleration on them is smaller and their precession frequency lower. From [67, p.6], the Larmor frequency ω_0 is equal to

$$\omega_0 = -\gamma \mathbf{B}_0 \quad (2.5)$$

(the negative sign here is a mathematical construction to indicate in which direction the moment is precessing)

2.1.5 Free Induction Decay

When considered on a macroscopic scale, the sum of all the nuclear magnetic moments individually precessing at ω_0 will create a moment \mathbf{M} in the direction of an applied field. The orientation of \mathbf{M} can be changed and caused to precess by applying a torque which is the same frequency as and perpendicular to \mathbf{B}_0 . Over time \mathbf{M} will precess back to its original position. This effect is achieved by using electromagnetic radiation to supply the torque. The precession of \mathbf{M} around z is called free induction decay (FID).

The quantum interpretation holds that as the movement of individual magnetic moments transition between Zeeman energy levels \mathbf{M} changes orientation. By combining eq. 2.3 with 2.4 gives 2.5, meaning that a wave at the frequency of precession is exactly the amount of energy needed to transport moments between Zeeman levels. This wave is "pulsed" for a short amount of time, during which moments gain energy and move to the next energy state. When they move back they give out photons at the same frequency, causing a measurable electromagnetic signal.

Figure 2.4 1.a) shows the path that \mathbf{M} takes when a field parallel with the z axis is used to polarise the nuclear spins, generating the moment \mathbf{M}_0 also parallel with z . The field \mathbf{H}_0 is a time varying electromagnetic field with frequency ω_0 . When \mathbf{H}_0 is applied \mathbf{M} twists round the z axis. 1.a) shows the movement in 2d, showing the component vectors \mathbf{M}_y and \mathbf{M}_z , in this 2d view \mathbf{M} moves around the x until parallel with y . 1.b) shows the same movement in 3d, showing the movement \mathbf{M} makes around the z axis. 2.a) and 2.b)

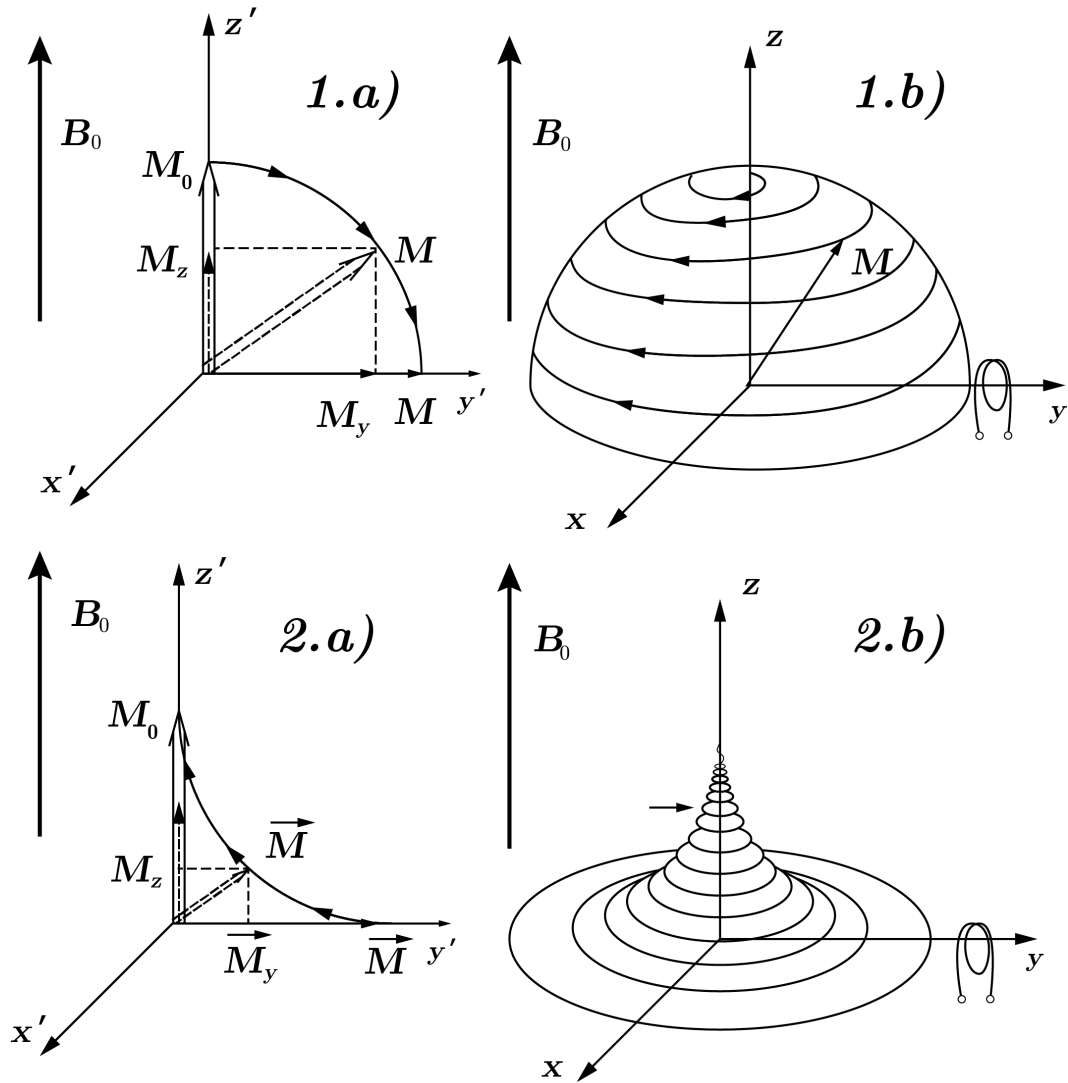


FIGURE 2.4: Movement of the vector \mathbf{M} during (figure 1) and after (figure 2) a $\pi/2$ pulse. Figures 1.a and 2.a show the movement in 2d, while 1.b and 2.b show the movement in 3d [68]

picture free induction decay. 2.a) shows movement limited to the z,y plane and 2.b) shows the precession of \mathbf{M} back to its thermal equilibrium \mathbf{M}_0 . The figures show the magnetic pick-up coil around the y axis.

The movement of the \mathbf{M} vector around the x axis (1) takes time. The longer the pulse is applied for, the more \mathbf{M} will move. It is logical to move \mathbf{M} to the point where the largest precession cone is seen. This point is when \mathbf{M} is $\pi/2$ radians from the x axis. The movement of \mathbf{M} in the $x-y$ plane is called the transverse magnetisation vector \mathbf{M}_{xy} . When there is thermal equilibrium, \mathbf{M}_{xy} is 0, an immediately after the $\pi/2$ pulse, \mathbf{M}_{xy} is at a

maximum, and a pick-up coil oriented in the y axis will detect this vector. Pulses are often referred to by the angle through which they move the magnetisation vector.

The behaviour of all spins inside a material - their position in relation to other moments and how free they are to move - governs how magnetic or non-magnetic a material is. Usually this concerns the electrons, while the nucleus itself has no net spin. Electrons are more difficult to detect in NMR because of their high precession frequencies compared to protons, NMR usually concerns itself with spin exhibiting isotopes. MRI equipment most often detects water, the hydrogen isotope H^2 molecule being the most abundant spin isotope.

2.1.6 T_1 and T_2 Processes

Immediately after a $\pi/2$ pulse the magnetic moment of the sample is perpendicular to B_0 . M_{xy} will eventually decay to 0. Of the factors which vitiate M_{xy} , there are two processes, T_1 and T_2 , which are the most significant.

- T_1 , or longitudinal relaxation refers to the relaxation of \mathbf{M} from perpendicular to the field \mathbf{B}_0 to parallel with it, representing a vector which grows along the z axis with time. M_z approaches M_0 as t increases -

$$M_z = M_0(1 - e^{-t/T_1})[69] \quad (2.6)$$

as discussed previously, the relaxation of the magnetisation vector is due to the spins inside the sample returning to their thermal equilibrium.

- T_2 : The field over the sample is not perfectly homogeneous: firstly, the distribution of nuclear dipoles inside the sample causes a given nuclear moment to experience varying magnetic field. Secondly, the magnetisation field \mathbf{B}_0 will always vary in field strength. Both conditions cause moments to precess at different speeds. Over time they de-phase and the signal is lost. The time the distribution of dipoles takes to decrease M_0 to 0 is called the T_2 time, and the time taken for both effects to reduce M_{xy} to 0 is the T_2' time.

The effect of field inhomogeneity is undesirable in NMR but the decay caused by nuclear effects can be analysed for information about the chemical structure of the sample, and as such the measurement of T_2 is the subject of much research [70], [71], [72]. A pulse sequence called a spin echo is sometimes used to reverse the effects of B_0 inhomogeneities which leaves the irreversible T_2 decay visible. Where M_{xy0} is the initial value of the transverse magnetisation, M_{xy} approaches 0 as time increases -

$$M_{XY} = M_{xy}e^{-t/T_2} [69] \quad (2.7)$$

Varying fields cause nuclear moments to precess at different frequencies. To model this effect it is assumed that inhomogeneities will even out over the body of the sample and hence the distribution of precession frequencies is usually thought to be Gaussian or Lorentzian, centred on the Larmor frequency. The internal magnetic moments can be approximated by two vectors which represent the extremes of the curve, +/- a given proportion of (ω). These two vectors represent the two extremes of the Gaussian curve. When viewed in a rotating co-ordinate scheme - where the frame of reference is rotating around z at the Larmor frequency - the vectors diverge, weakening the overall moment.

When free induction decay is viewed in the frequency domain, the different Larmor precession frequencies inside a sample are evident (figure 2.5). These are referred to as Parts Per Million shifts (parts per million refers to Hz shift / Larmor frequency). Due to unique molecular composition substances exhibit signature shifts. These are used to identify samples in NMR spectroscopy.

2.1.7 Spin Echoes and the CPMG Sequence

The spin echo and CPMG scans (Carr-Purcell-Meiboom-Gill, after the pioneers of the technique) are variations on pulsed NMR where multiple pulses are applied to manipulate the moments [74]. Spin echoes harness the de-phasing magnetic moments to produce a repeated "echoes" of signal. A series of pulses are used to "flip" the magnetisation vector causing the moments to partially re-phase causing an "echo". Multiple pulses can be applied to produce a chain of echoes. This is useful when determining the T_2 as the effect of inhomogeneities in B_0 are reversed, and the T_2 decay envelope becomes visible in the time

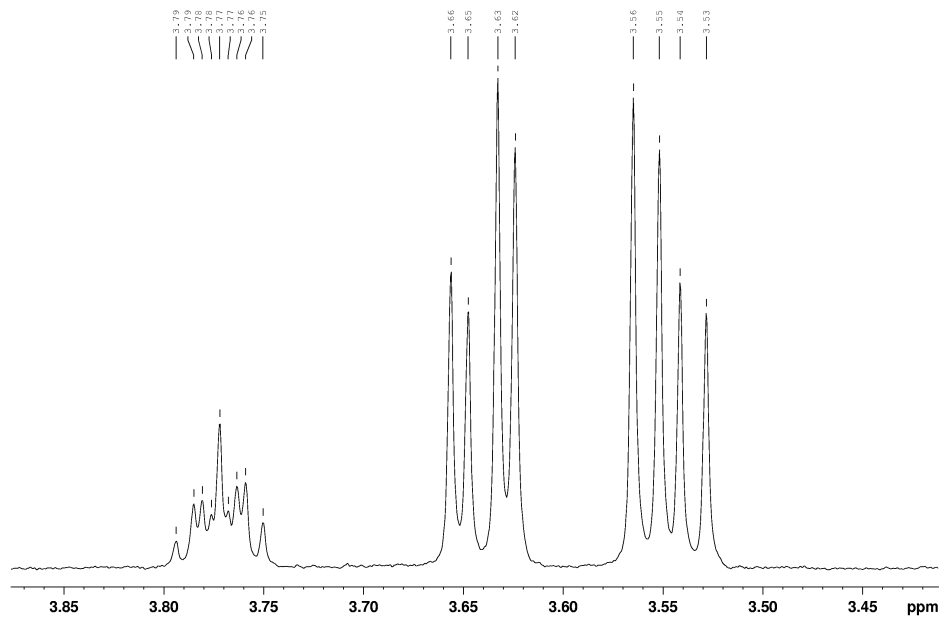


FIGURE 2.5: A typical NMR signature of glycerol. The plot is a frequency spectrum, the X-axis represents frequency in terms of parts-per-million shift from the Larmor frequency and the Y-axis represents relative intensity (%) of the frequency content. Parts Per Million shifts are marked on each peak [73]

domain. The spin echo was first documented by Erwin Hahn [7] in 1950, later Carr and Purcell [75] and Meiboom and Gill [76] used multiple 180° pulses to refocus the precession (the sequence is referred to as a CPMG sequence) Figure 2.6 shows the pulse sequence and resulting echo.

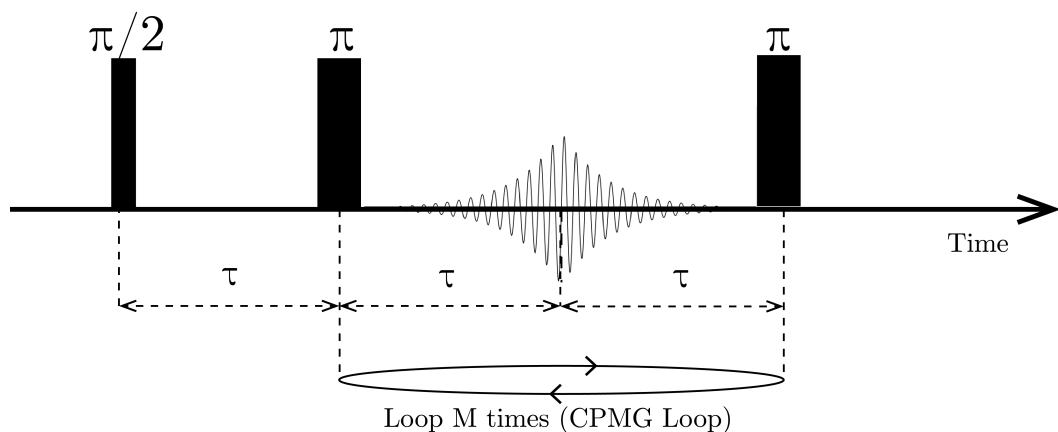


FIGURE 2.6: The spin echo sequence. A $\pi/2$ pulse is provided, and later after a time τ a π pulse is used to re-phase the spins producing an echo at time 2τ , then at time 2τ another π pulse may be applied [77]

The spin echo works by applying a $\pi/2$ pulse, then at a time larger than T_2' and smaller than T_2 a further 180° pulse. Figure 2.7 (a) shows the magnetization vector \mathbf{M} along the same axis as B_0 . The $\pi/2$ pulse is applied, then at a time larger than T_2' and smaller than T_2 a further 180° pulse. (A) shows the magnetization vector \mathbf{M} parallel with B_0 . The 90° pulse is applied, generating a torque and turning \mathbf{M} (B) until it is parallel with y (C). Here the precession can be detected by a receiver coil. The T_2' processes de-phase the spins (D) and at some time τ a 180° pulse is applied, which flips the spins around the x axis (E). Now the directions of the spins are reversed (F), and they gradually re-combine to produce an echo (G). The spins then again de-phase (H).

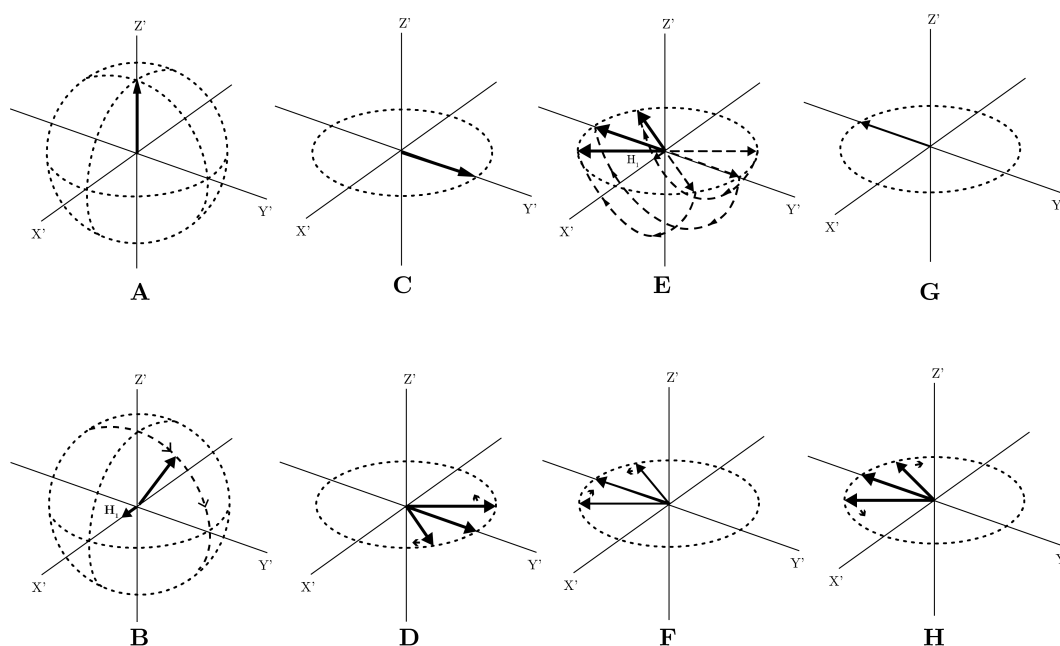


FIGURE 2.7: The different stages of the spin echo process are shown as different pictures A-H in the rotating system of coordinates described by Bloch [75]

2.2 NMR Methods

The first investigations of nuclear paramagnetism were used to verify the existence of nuclear magnetic moments [1] and by 1942 Gorter and Broer [2] were conducting a (non-functioning) experiment recognisable as the early continuous wave experiment on solids and Purcell, Torrey and Pound [4] detail a functional continuous wave experiment the same year. In 1946 Bloch [5],[6] outlined a technique where free induction decay could be

directly observed. Also outlined were the mathematics which have been used extensively to interpret FIDs. The pulsed NMR technique has already been discussed extensively but there are other, slightly different techniques also used to study nuclear paramagnetism.

2.2.1 Continuous Wave

The continuous wave setup is pictured in figure 2.8, a resonant circuit or tank circuit sits in the field of a static magnet. This magnet supplies the field needed to polarise the nuclear paramagnetic moments, but modulation coils are used to "sweep" the field. When the field causes the nuclei in the sample to precess at the same frequency as the 30 MHz oscillator, there is a small change in the magnetic susceptibility of the sample. The resonant circuit is connected to a receiver via a matched coaxial cable. A lock-in amplifier is used to reduce the noise in the system and detect the NMR signal. This technique does not observe FID but the change in magnetic susceptibility related to resonance. The continuous wave experiment reveals limited information about the sample and it is also time consuming to run. Much more information can be obtained from the pulsed NMR technique.

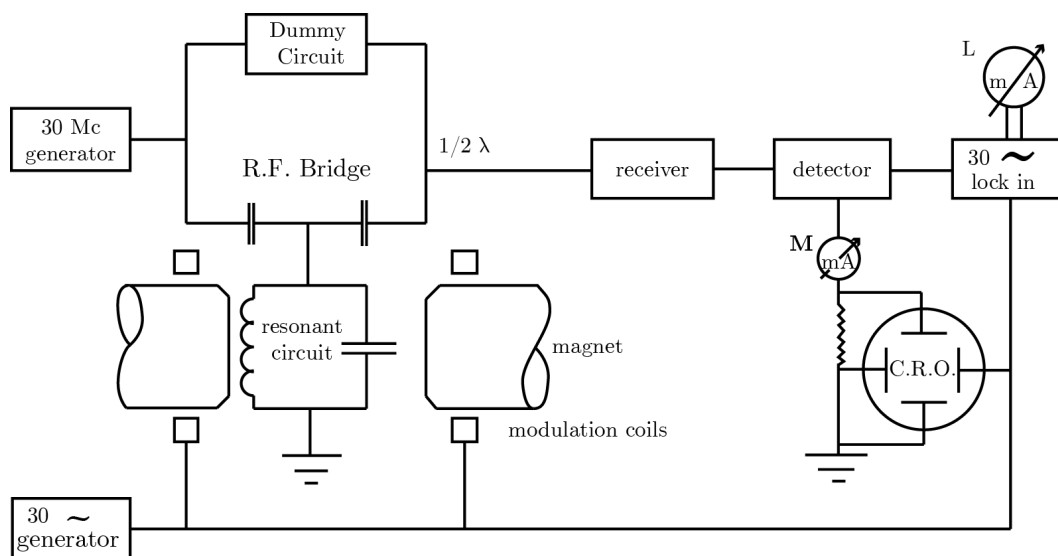


FIGURE 2.8: Continuous wave experiment. When a resonance is induced there is a small change in the magnetic susceptibility of the sample, causing the impedance of the tank circuit to change and the signal at the receiver to dip [78]

2.2.2 Proton Magnetometer

The proton magnetometer is the simplest apparatus capable of detecting free induction decay. The magnetometer uses the earth's magnetic field to develop the thermal equilibrium magnetisation and a coil positioned orthogonally to the Earth's field to provide the 90 degree pulse. The vector \mathbf{M} aligns itself with the field and after a few seconds the current through the coil is stopped, causing \mathbf{M} to precess back to \mathbf{M}_0 . Because the Earth's magnetic field is used as the polarising field the Larmor frequency is low and the signal detected is small, owing to the rate of change of flux through the pick-up coil

$$V = -N \frac{d\Phi}{dt} \quad (2.8)$$

The paramagnetic moment \mathbf{M} is also small due to the small field strength of the Earth ($\approx 20 \mu\text{T}$), as the nuclear paramagnetisation is proportional to the applied field.

2.3 The Pulsed NMR Experiment

The work in this thesis is conducted on a custom made pulsed NMR setup. The setup is tested with a magnetic pickup coil at $\omega_0 \approx 1.84 \text{ MHz}$ with the single pulse sequence and the spin echo sequence. A free induction decay is induced in the sample by the pulse and is mixed down to a lower frequency and stored in memory for analysis. The schematic of the experiment is pictured in figure 2.9, a sample sits inside the inductor of a resonant circuit, which sits in the magnetic field provided by a static magnet. The magnetic field causes the spins to precess at a Larmor frequency and the tank is tuned to this frequency. The pulse generator provides short bursts of energy at the Larmor frequency, filling the tank with energy and causing an oscillating magnetic-field through the sample, which causes the magnetic moment to change its orientation. During this phase the amplifier protection blocks the signal from damaging the amplifier. Between pulses the tank is prepared to detect signals - the blanking signal damps the tank circuit - "draining" the energy from it. The sample recovers, creating an oscillating magnetic field of its own which is amplified by the tank. This signal is mixed down by the quadrature detector and stored in memory. and the rest of this section will detail each part of the experiment in turn.

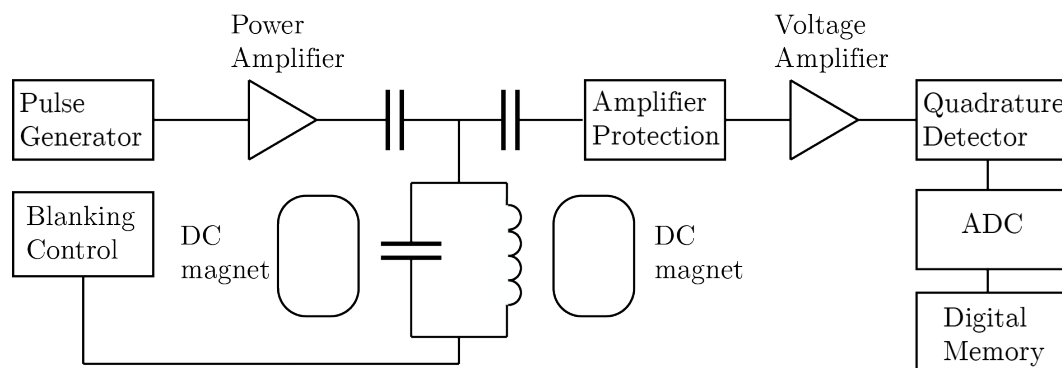


FIGURE 2.9: Schematic diagram of the pulsed NMR experiment. The Pulse generator and blanking control the experiment, while the detector, ADC and memory are used to acquire the signals.

2.3.1 DC Magnet

A DC magnet provides the field which tilts the orientation of the moment inside the sample. The sample and tank circuit are situated inside this field. The energy needed to change spin states is directly proportional to the magnet strength, which relates to a particular frequency through equation 2.5

The strength of the magnet therefore also dictates the speed of precession. The higher the strength of the magnet, the better the resolution of the FID decay and the clearer the resolution of any fourier transform NMR. The homogeneity of the magnet will also affect the relaxation time of the sample. Higher precession frequencies also lead to higher signal to noise ratios in the detected signal, as the signal induced in a coil is proportional to the rate of change of magnetic flux. Research NMR magnets are often in the order of Tesla, with values such as 4.7 T common. Design of the DC magnet is one of the biggest performance-defining factors in the design and many of the improvements in NMR over the past decades are due to the design of powerful homogeneous magnets.

The effect of inhomogeneity in the magnet can be considered either in the frequency domain or the time domain. In the time domain, the effect of magnet inhomogeneity is to shorten the T_2 time. In the frequency domain the spectral peak due to the FID is broadened, or rather the more homogeneous the magnet is, the more fine the resolution of the FFT is, allowing smaller variations in the FID to be measured.

2.3.2 Tank Circuit

The tank circuit is used for two purposes, to produce the excitation field \mathbf{H}_0 and also to detect the free induction decay signal. In figure 2.9 the tank circuit is the arrangement of the parallel inductor and capacitor in between the DC magnets. Additional circuitry is used to prepare the tank between the pulse and read phases. Tank circuit refers to a inductor and capacitor which when coupled together transfer energy between each other in a manner analagous to a pendulum: if a signal is induced over the inductor at the resonant frequency ω_0 , charge will accumulate in the tank transferring back and forth between the capacitor and inductor which amplifies the signal. Free Induction Decay signals are of the order of micro volts and require extensive amplification. The reactance of the tank at ω_0 is high but either side of this peak reduces rapidly with frequency, attenuating background EM radiation from the signal. ω_0 is tuned by selecting the values of L and C, to match the Larmor frequency.

In the pulse phase the tank produces a large (hundreds of volts) signal. The direction of the magnetic field lines inside the inductor must be oriented orthogonally to \mathbf{B}_0 to produce the desired torque on the magnetic moment. Between the excitation and read phase, charge must be drained from the circuit in preparation for detecting the FID, the large movements of charge involved would otherwise swamp the comparatively tiny FID signal. The charge is drained by critically damping the circuit by means of a FET which switches for a short time after the excitation cycle. Modern NMR experiments often use separate coils for exciting the sample and detecting the signal; in this thesis the experimental setup was validated with a single tank circuit for both.

2.3.3 Amplifiers and Filtering

There are two amplifiers shown in figure 2.9. The first is the power amplifier, used to provide energy to the tank circuit during the excitation phase. This amplifier drives the tank with the signal from the pulse generator.

Amplification of the FID signal requires high gain and filtering. The signal levels need to be amplified from the micro volt level without adding significant noise. There are different ways of achieving this: in high frequency systems RF amplifiers are used and the system is matched to $50\ \Omega$. This minimises noise and stops reflections which degrade the signal. In this thesis the experiments are conducted at a low precession frequency and the amplifiers are designed with low noise op-amps. The amplification is protected from the excitation pulses by circuitry which prevents large voltages appearing at the front end of the amplifiers. Filtering can be provided either by hardware or in software after the signal has been digitised, this allows for fully automated control of cut-off characteristics.

2.3.4 Pulse Sequencing

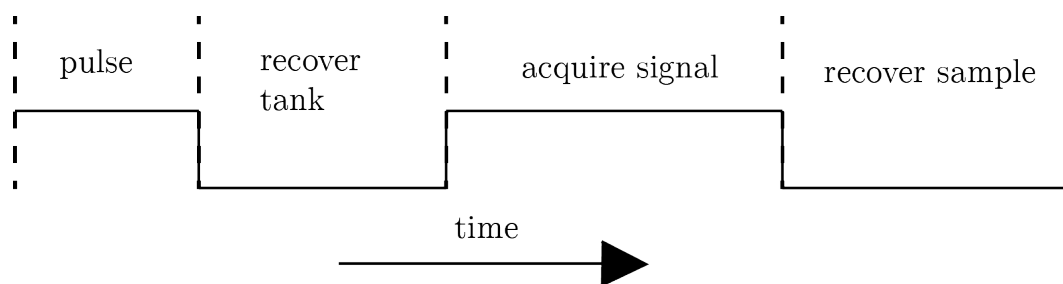


FIGURE 2.10: The pulsed NMR sequence. The pulse is used to excite the sample, after which the tank must be "drained" of energy. In the acquire stage the signal from the tank is detected, digitised and stored in memory. After the read stage there is a period of time for any residual oscillation to fade.

The control of pulses and system timing is controlled by computer or some control unit capable of producing controllable timed pulses to initiate various phases of the experiment. The NMR experiment relies on careful timing to control the pulse sequence, the damping required by the tank, the protection of the amplifiers and the signal acquisition.

For the one pulse experiment, a typical pulse sequence is pictured in figure 2.10

- *pulse phase* the signal generator emits the excitation signal, the blanking on the tank stays off, giving the tank maximum Q and the signal amplifier protection is enabled.
- *recovery phase* the pulse generator is now off, the blanking for the tank is enabled and energy drains from the tank. The amplifier protection is left on.

- *read phase* the signal generator stays off, the blanking switches off maximising the Q of the tank. The amplifier protection shuts off so that signals can be read, and the ADC digitises the FID from the quadrature detector.
- *recover sample* A short time is allowed for the sample to recover from any residual effects (T_1 is always greater than T_2 , meaning that although the transverse magnetisation has died away, there still may be precession of groups of nuclear moments.)

2.3.5 Quadrature Detector

The quadrature detector is used to alter the frequency of the wave for computer analysis. The detector mixes the incoming precession signal with a second signal, the output is the difference in frequency between the two. The detector down-shifts the frequency of the signal. Detection is necessary because precession frequencies are often in the MHz range which causes problems with computer storage and analogue-to-digital conversion; if the frequencies are shifted down then the ADCs needed to adequately convert the signal become cheaper and the amount of memory needed to store the signals becomes smaller.

The operation of the detector is pictured in figure 2.11. Input signals are the signal (f_{sig}) and an operating frequency (f_{osz}). The outputs are sine and cosine, both are necessary for correct reconfiguration of the input. If the input signal is 10 MHz and the detector frequency is also 10 MHz, the output will be 0 Hz - if the signal is a decaying sinusoid, the output will show only the envelope of the signal. Supposing that there was a 10 Hz difference between ω_{op} and S_{FID} , the output would be 10 Hz, but there would be no way of telling if ω_{op} was higher or lower frequency than S_{FID} . This is the problem to which the use of two outputs - sine and cosine - is the solution. When both are used together, the phase information between the two can be used to indicate whether ω_{op} is smaller or larger than S_{FID} .

2.3.6 FFT Analysis

The signals from the quadrature detector are digitised and stored in memory. These real and imaginary signals are used to generate a power spectrum through the use of a Fourier

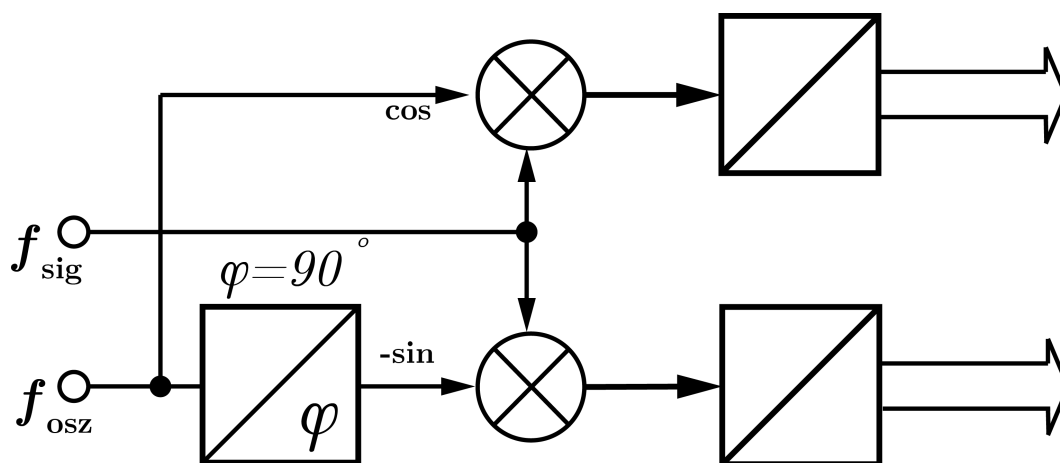


FIGURE 2.11: The operation of a quadrature detector. The quadrature detector is useful in experiments such as the NMR experiment, as it can be used to shift high frequency signals to low frequencies in preparation for digitisation. [79]

transform. Inspection of the power spectral density reveals the frequencies present in the data. This can be used to determine the molecular structure of the sample and is the basis of NMR spectroscopy. A typical FFT can be examined for the signatures of materials and the constituents of the samples can be determined.

Successive scans are often averaged by a computer to reduce noise. Averaging lowers the noise floor of the signal enabling much smaller signals to be detected.

2.4 The EPS in NMR Techniques

In this thesis the EPS is used instead of the magnetic pick-up coil to detect free induction decay signals, but the EPS is used to capture the electric field component of these signals rather than the magnetic field. The existence of this signal is known from Faraday's law which states that time varying magnetic fields are always accompanied by electric fields.

$$\nabla \times \mathbf{E} = \frac{\partial \mathbf{B}}{\partial t} \quad (2.9)$$

As free induction decay is a precessing magnetic moment, by Faraday's law there exists an associated electric field. The measurement of this field was verified by Aydin [20].

In the pulse phase of the experiment a very large electromagnetic field is present in the vicinity of the electrode. Without precaution this pulse would destroy the front end of the sensor, depositing enough charge to short the input gates of the op-amp. There are a number of precautions taken to mitigate this effect to an operable level: the first involves the use of a tuned trap, which will be covered later. The second is the use of gating in order to protect the op amp. This gating can be provided by extra circuitry or there are op-amps (for example the EL8100 [80]) that provide gated on-chip protection.

2.4.1 Noise

The NMR FID signal is very small ($\approx \mu\text{V}$) and diminishes further with low field strengths (see eq. 2.3). The limiting factor when measuring very small signals is the noise floor, hence the EPS sensors are designed for low noise performance.

There are multiple sources of electrical noise. These are caused by various factors which affect the movement of electrons creating small, unpredictable currents. The main sources of noise inside a circuit are -

- *Shot noise* is the name given to the fluctuations in voltage caused by the movement of electrons. Since one electron has one electron volt, a voltage is the result of electrons, individual pulses in the same place integrated to give a DC response. There will always be a small deviation from the DC value caused by random movement of electrons. Within semiconductors shot noise is larger because of the movement of electrons through the silicon lattice.
- *Johnson noise* occurs as a result of random thermal motion of the electrons inside a material. Johnson noise or thermal noise increases with temperature and resistance. Its absolute value is given by [81, p.39]

$$\overline{v_t^2} = 4kTBR \quad (2.10)$$

T = temperature (k)

k = Boltzman's constant (dimensionless)

B = system bandwidth (Hz)

R = resistance (Ω)

Hence large resistances generate more noise

- $1/f$ noise rises at low frequencies. Op-amps are characterised with a $1/f$ corner, below which the noise rises. Experiments in this thesis are conducted above the $1/f$ corner of most op-amps, and the $1/f$ noise is not considered in the design process.

2.4.2 Low Noise Design

FET type op-amps are used in the EPS. The low bias current enables the design of sensors which draw effectively no real current. Because of this high input impedance, shot noise is dramatically reduced due to the very small amount of electrons moving through the front end.

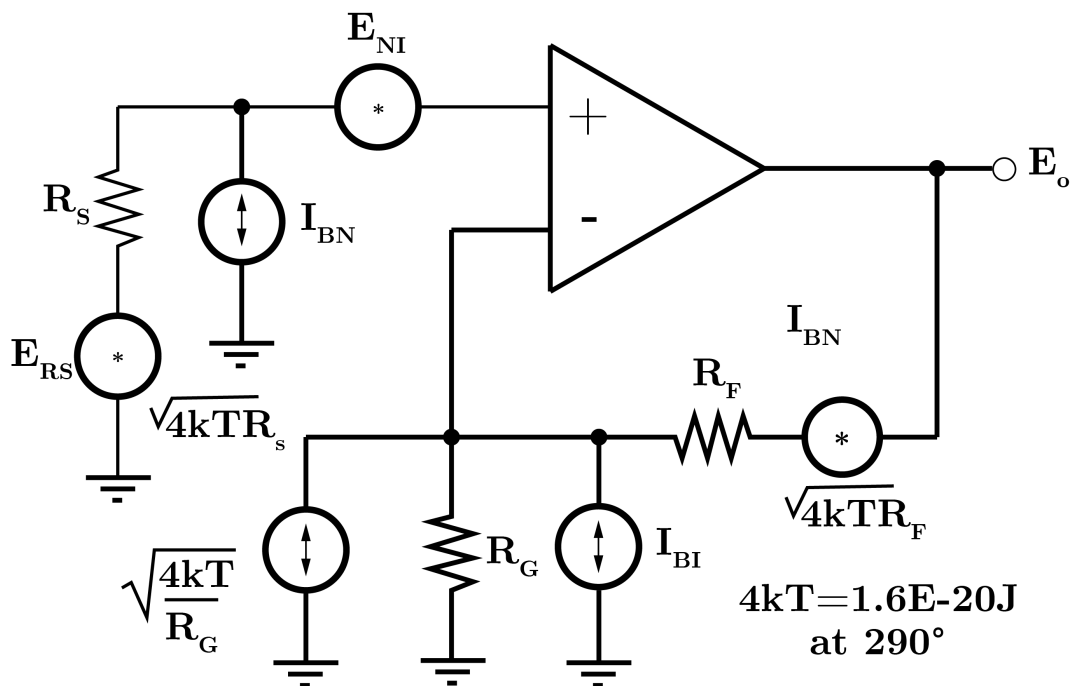


FIGURE 2.12: Noise in op-amp circuits. Electrometers for NMR must be very low noise, and the above picture provides a useful reference when designing such circuits. Noise sources are represented as current and voltage sources for ease of calculation. [59]

Noise sources in op-amp circuits are pictured in figure 2.12. This interpretation combines various processes which create noise currents and voltages to give a convenient guide to

a designer. Consequently the interpretation offers limited information about the sources of noise.

- E_{NI} input voltage noise density
- E_{RS} represents the Johnson noise in R_S
- I_{BN} represents input current noise density. This value is multiplied by R_S to give a noise voltage
- the feedback resistor adds Johnson noise, represented by the term $\sqrt{4kTBR}$
- I_{BI} current noise, multiplied with the value of R_G to give the noise voltage
- Johnson noise in the feedback path is represented by the noise term in parallel with R_G

EPS sensors are usually unity gain or $\times 2$ gain, making the noise from the feedback resistors negligible. The $1/f$ noise is a consideration when working at low frequencies, but as all experiments are conducted above the $1/f$ corner of most op-amps, the $1/f$ noise is also negligible. The two noise factors of major consideration when designing the EPS are labelled in fig. 2.12 as E_{NI} and I_{BN} - the two front end noise sources. Although I_{BN} in most FET op-amps is orders of magnitude smaller than E_{NI} , when I_{BN} is multiplied by the front end resistance R_S - which is large for EPS sensors - the two figures often become more similar. For example, an OPA827 op-amp is listed as [82] -

- input voltage noise density $E_{NI} = 4 \text{ nV}/\sqrt{\text{Hz}}$
- input current noise density $I_{BN} = 2.2 \text{ fA}/\sqrt{\text{Hz}}$

Hence when R_S is of the order of $\text{M}\Omega$ the noise due to E_{NI} and I_{BN} become the same order. Omitting the effect of the feedback path, the total noise is calculated as the geometric mean of the two front end noise sources -

$$\text{total noise } e_N = \sqrt{E_{NI}^2 + (I_{BN} \times R_S)^2} \quad (\text{V}/\sqrt{\text{Hz}}) \quad (2.11)$$

Because of this, the largest value of the noise tends to dominate and the second largest becomes insignificant. If two-stage amplifiers are used, gain is applied at the first stage, in order that the second stage noise will be insignificant in comparison.

2.4.3 Noise Testing

When testing the noise performance there are two useful tests to ascertain noise. In both, the voltage spectral density of the output is calculated to give the $V/\sqrt{\text{Hz}}$ spectrum. To test the total noise the amplifiers inputs are left open, giving a total picture of both E_{NI} and I_{BN} (when the $1/f$ noise is considered, the corner frequency can clearly be seen on a plot of the spectral density). The voltage noise can be tested by shorting the inputs of the op-amp together - when an amplifier is used with one input referenced to ground, shorting the inputs shorts the voltage generated over R_S , leaving E_{NI} .

Chapter 3

Design of the NMR Experiment

This chapter discusses the design of the apparatus used to capture NMR signals. Traditionally magnetic field detection is used to capture these signals, but in this thesis the experiment designed uses both magnetic pick up coils and the electric field detection technique. Signals from both of these methods can then be compared for differences in signal to noise ratio. The electric field detection technique was first described by Aydin [20] and is patented by Sussex University on behalf of the Sensor Research Group and has been shown to improve the signal to noise ratio of FID signals. This chapter aims to extend that work by performing the same e-field detection at low magnetic field strengths where the signal is low for two reasons: firstly, the magnetic moment created is proportional to the DC field strength and secondly, the magnetic field detection technique further deteriorates the signal as the voltage induced over a coil is proportional to the rate of change of the flux through it. The e-field detection system removes this second cause of noise and can therefore be expected to improve signal-to-noise ratio. Also outlined is the use of pulse sequencing and sophisticated signal averaging and acquisition using a commercial unit - the ispin NMR. This extends the analysis of signals with the e-field detection system by enabling simple NMR spectroscopy.

3.1 Overview

The pulsed NMR experiment uses RF energy to excite a precessing magnetic moment in a sample when it sits inside a static magnetic field. The RF energy is applied across a resonant tank circuit, creating an oscillating magnetic field within the inductor of this tank. The sample is placed in this region, and the magnetic flux passes through it. A larger static magnet provides a DC magnetic field in which the tank and the sample are mounted. The flux lines of this DC field are always at right angles to the RF flux in the inductor. The RF energy is applied for a short amount of time, and afterwards energy is drained from the resonant tank circuit ready for its use as a receiver coil. The precessing magnetic moment induces a voltage across the coil. This signal is amplified and filtered to give a visible NMR signal. The timing of the experiment is critical. The different phases of the experiment occur in a very small space of time and each is important. Custom circuitry could be built for timing the different phases of the experiment and generating control voltages, but for the purposes of this test a commercial unit – the ispin [83] – was purchased. The ispin generates the RF excitation signal and the control voltages needed to control the damping of the tank circuit and amplifier protection for signal acquisition. It also offers full control of the timing of these parameters by way of a Labview GUI. In addition to this the ispin captures and digitises signals, ready for useful data processing operations such as the Fourier transform. In laboratory NMR experiments the DC magnetic field would usually be provided by a large super-cooled magnet. These magnets are highly homogeneous and very high field strength ($\approx 3\text{T}$ is typical), which gives good signal to noise ratio. Here the magnetic field is provided by a Helmholtz pair. The static field which the pair generates is much smaller (1.13mT at resonance) and consequently the FID signal is lower frequency. After consideration of the range of field obtainable with the Helmholtz pair, an operating frequency of 48.5KHz was selected. For a glycerine sample, this corresponds to 1.03mT. The low operating frequency has many practical implications for the design of the experiment – the consideration of which will make up the bulk of this chapter.

Fig 3.1 shows a block diagram of the experiment. The magnetic field acquisition path is represented by the blue line, the electric field by the red line. The labels in the figure are as follows:

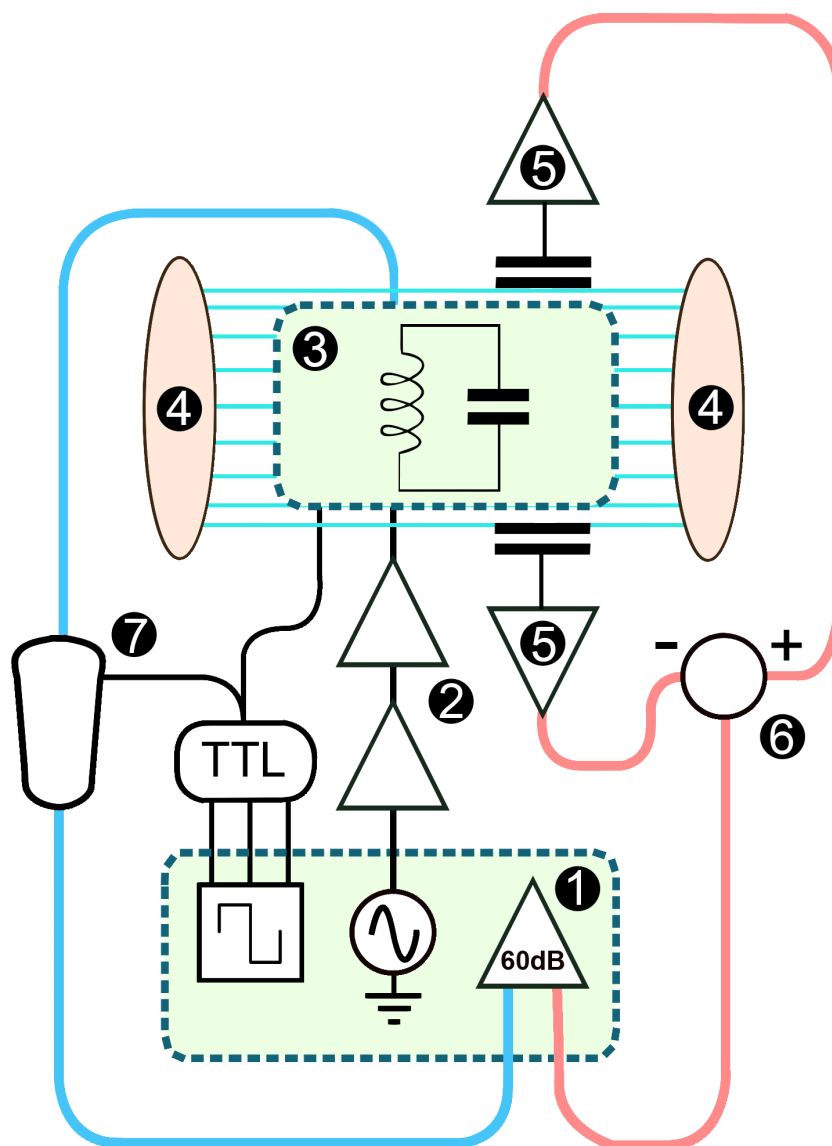


FIGURE 3.1: Schematic diagram of the NMR experiment incorporating both magnetic (blue line) and electric field (red line) detection. Different parts of the experiment are denoted by the numbered labels.

1. Ispin. The ispin produces TTL pulses for the control of the experiment, supplies a 2V peak to peak excitation signal at a chosen frequency from 0-100 MHz, receives the signals from either the magnetic or electric field detection and amplifies those signals by 60dB.
2. The output amplifiers. Needed for amplifying the signal from the ispin. The first stage is a 10X voltage amplifier, the second is a power stage needed for driving the tank circuit.

3. The tank circuit. The excitation pulse is applied across the tank and the sample is inserted inside the inductor. The tank sits inside the static DC field shown by the horizontal blue lines. The damping of the tank is controlled by a FET which is gated by the TTL pulses from the ispin.
4. The Helmholtz coil produces the DC field in which the tank circuit sits.
5. The electrometers are AC coupled to the sample on either side of the test tube.
6. This summing node represents an op-amp based differential stage.
7. The tuned trap takes signals from the tank in the receive cycle of the experiment. The trap is gated by a TTL pulse from the ispin.

3.2 Ispin

The ispin is the central control unit for the experiment. It is a FPGA based data acquisition and pulse generation unit. Pulses are created with the use of the labview software or by batch file. The ispin unit needed a couple of modifications for use the chosen frequency of 48.5KHz. The amplifiers needed replacing, as they are out of band at 48.5KHz. The output amplifier was replaced with an external RF amplifier. The first stage of this amplifier is a x10 voltage amplifier based on an AD849 op-amp with 1.8MHz bandwidth. The second stage is a power amplifier with a bandwidth of 90MHz. The input amplifier was also replaced by a Miteq amplifier [84] with a bandwidth of 10KHz to 200MHz. This amplifier has an in band gain of 60dB. An addition to the ispin was also made – a circuit to handle the TTL voltages that control the tuned trap blanking and the damping of the tank circuit. As will be discussed later in the chapter, two different ways of controlling the ispin were used. The first is with the GUI supplied with the ispin. The second was a custom made Labview VI which performs many scans over a range of parameters. The custom written GUI has limited control over the TTL outputs on the ispin and more circuitry was required to turn the limited information into correctly timed pulses.

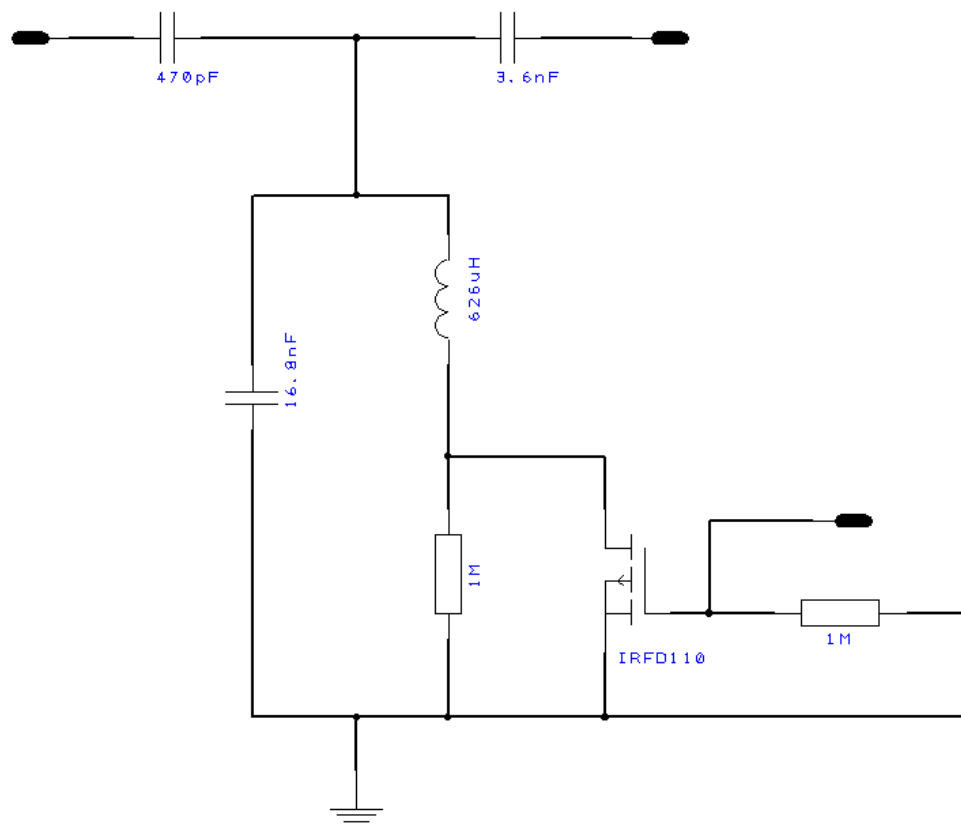


FIGURE 3.2: Schematic of tank circuit with Q damping. The tank circuit is used to hold the sample, which sits inside the inductor. A MOSFET -the IRFD110 - is used to switch a resistor in and out of the circuit.

3.3 Tank Circuit

The tank circuit was designed to work as close as possible to 50 kHz. The main design consideration was the Q factor which was designed to be as high as possible to maximise the energy stored and hence the strength of the excitation field. It also determines the parallel resistance of the tank which is an important factor when considering the design of the tuned trap and the transformer. The full schematic of the tank circuit is pictured in figure 3.2. The inductor was designed first and was designed so that the sample test tube fitted through the centre and allowed room for two electrometer probes to pass through holes in either the side. The former on which the coil was wound was designed with a small space down either side to allow a small copper electrode on the either side to slide freely in and out when removing the sample from the coil. The largest size of test tube

available was chosen for the sample, 32mm diameter. The resulting coil is two layers and measures 72mm x 32mm. This gives the best trade-off between Q - which is highly affected by the aspect ratio - and high inductance. Other specifications are:

$$L = 626 \mu\text{H}$$

$$Q = 47$$

$$\text{Length} = 72 \text{ mm Turns} = \approx 220$$

The capacitor used is a silver mica capacitor. Silver mica has a Q value, high enough to be insignificant in comparison to that of the coil. Two capacitors in parallel were used to provide a tank resonance around 50KHz. The resultant capacitance measured 16.8 nF. The resonant frequency of the tank is calculated:

$$\frac{1}{2\pi\sqrt{626 \times 10^{-6} \times 16.8 \times 10^{-9}}} = 49.077 \text{ kHz} \quad (3.1)$$

However when the sample is in the inductor, the resonant frequency measures 48.5 kHz. Terman [85] gives the parallel resistance of a resonant LC circuit as:

$$r = \omega L Q$$
$$r = 2\pi \times 48.5 \times 10^3 \times 626 \times 10^{-6} \times 47 = 8695 \Omega \quad (3.2)$$

However with the glycerine sample tube inserted the inductance is slightly increased and the resonance is closer to 48.5 kHz. The coupling capacitors were chosen with a high enough reactance at the operating frequency that they would not load the tank circuit. To achieve this, the path to ground either side of the tank must be higher impedance than the parallel resistance of the tank. Initially a value of 47pF was chosen for both coupling capacitors. This was later change to 3.6nF for the input capacitor and 470pF for the output capacitor, with the design of the transformer and the tuned trap. This was because it was realised that the input capacitor was needed to be low to keep energy in the tank during the pulse phase, whereas the output capacitor had a negligible effect in this respect, as it is in series with the high impedance tuned trap during the pulse phase. A damping circuit is needed to drain the energy from the tank circuit after the excitation pulse is applied,

ready for its use as a pick-up coil. To accomplish this, a damping resistor is added between the inductor and ground and shorted out by a FET for the time the excitation pulse is applied. Hence, for the excitation period and the read period the tank is resonant and there is a small amount of time between the two where the tank is critically damped. To short the damping resistor, a power MOSFET – IRFD110 [86] was chosen for its very low on state resistance (0.54Ω). To calculate the damping resistor (r) we use the critical damping criterion given by Fortney [87] for a parallel LCR circuit

$$r = \frac{\omega^2 L^2}{C} \quad (3.3)$$

From which the value is calculated to be 386Ω . A 390Ω resistor is used as the nearest preferred value.

3.3.1 Analysis of the Tank Circuit

The most important measure of power available to the circuit is the energy density inside the inductor; power dissipated in the tank circuit alone is misleading as this is not relative to the size of the inductor. From Krauss [88]

$$\text{energy stored (W)} = \frac{1}{2V} LI^2 \quad (3.4)$$

The energy density of the inductor is compared to that of Aydin [20] to give an estimate of how much power is needed to produce a signal from the same sample, glycerine. Aydin's inductor measured 3.4 mW/m^3 , whereas the new inductor designed is 6.6 mW/m^3 . This measurement gives a rough indication of the voltage needed across the tank. To give the same energy density inside the sample approximately half the voltage used in Aydin's experimental setup is needed, though the energy needed to excite a signal is the integral of the time for which it is applied, so this is not an absolute measurement and is affected by the amount of time the tank takes to accumulate energy.

Measurements of the tank circuit in high Q and low Q can be seen in figure 3.3. The tank is shown to give approximately 20 dB difference between the high and low Q states.

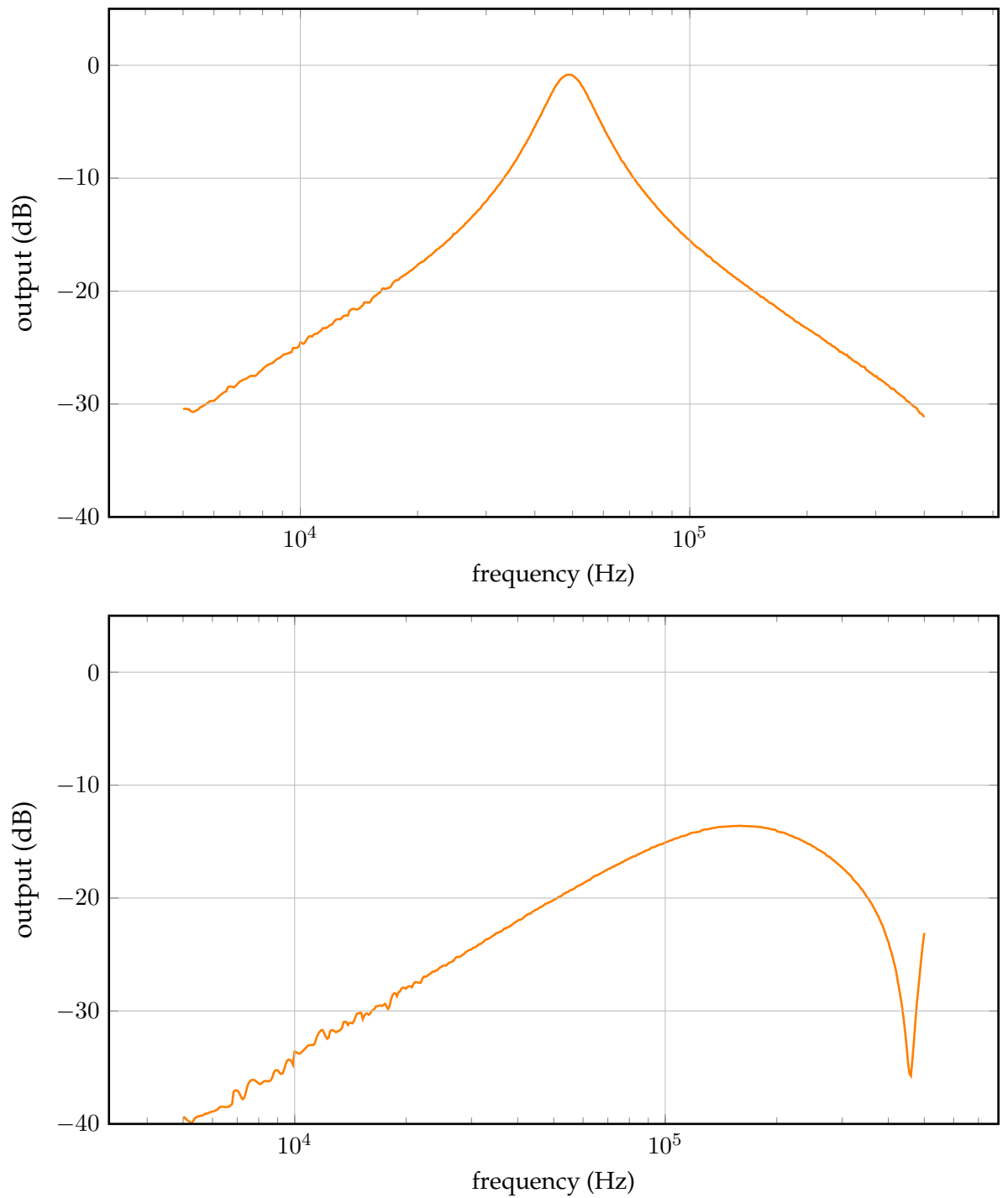


FIGURE 3.3: Bode plots of tank circuit operation. The circuit is ≈ -1 dB in high Q (top) and ≈ -20 dB in low Q (bottom) at the frequency of operation (48.5 kHz)

3.4 Tuned Trap

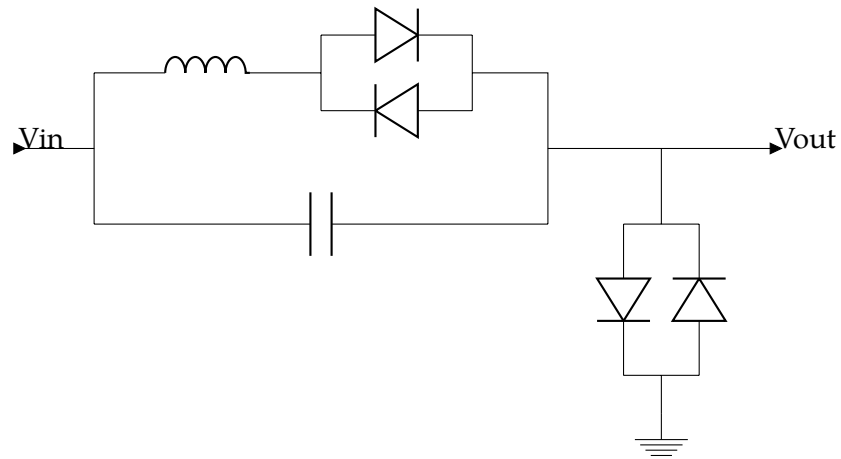


FIGURE 3.4: Basic tuned trap schematic. When the signal is large ($V \geq 0.7\text{ V}$) the circuit attenuates the signal, and when low ($V \leq 0.7\text{ V}$) the signal passes unattenuated to the receiver.

The tuned trap protects the front end of the Miteq amplifier. It does this by acting as a high impedance circuit when the signal is large, and a low impedance when the signal is small. When the signal is large, greater than one diode voltage drop, the circuit acts as a tank circuit with a very high Q , and hence a very high parallel impedance. This tank acts as a voltage divider with the two cross diodes and these diodes clamp the output voltage at $\pm 0.7\text{ V}$. When the signal is small, the path through the inductor is an open circuit and the trap is just a capacitor in series with the output.

The tank circuit consists of an inductor constructed from a potted ferrite core and a 47 nF silver mica capacitor. Silver mica was chosen here for its low series resistance and high voltage rating. The potted ferrite core allows very high Q ($Q = 170$) and also some control over the inductance by moving a ferrite screw. This meant the tank could be tuned to the operating frequency, which corresponds to an inductance of 0.23 mH . The parallel resistance of the tank is

$$r = \omega L Q \quad (3.5)$$

$$r = 2\pi \times 48.5 \times 10^3 \times 230 \times 10^{-6} \times 170 = 11\,915\ \Omega$$

In addition to the basic tuned trap pictured in 3.4 the circuit is modified with a JFET connected in parallel with the output (see fig 3.5). This JFET shorts the signal out while the

excitation pulse is applied to the tank, to minimise the saturation of the amplifier. The gain of the Miteq amplifier is 60dB, and even 0.7V input will saturate the amplifier, even if it does not harm the front end. The design of the trap has also been modified to include an op-amp buffer. This addition is necessary as the signal captured is expected to be small at low frequencies and the tuned trap needs to attenuate the signal as little as possible. The Miteq amplifier is $50\ \Omega$ input impedance, and this will produce a voltage divider with the coupling capacitor of the tank circuit, attenuating the signal greatly. Here an op amp buffer is added to prevent this attenuation. The addition of the buffer creates another problem however: it adds noise to the signal. The op-amp chosen, the AD656, was selected for its low voltage noise specification ($7\text{nV}/\text{Hz}$). This noise will be insignificant as the lowest signal detectable by the Ispin is in the order of millivolts, which puts the minimum detectable signal level around $1\ \mu\text{V}$. This is well above the noise floor of the AD656. A DC bias resistor is also added to the input terminal of the op-amp.

The JFET used to short the excitation signal before the amplifier is a U310 [89]. This JFET was chosen for its low on state resistance and low capacitance. These two requirements are conflicting as lower resistance FETs have larger conduction channels and hence larger capacitance, so a trade off between the two was made. The U310 has 2.3pF capacitance from source to drain and an on resistance of $153\ \Omega$. The full schematic of the tuned trap complete with the JFET modification and component values is pictured in fig. 3.5.

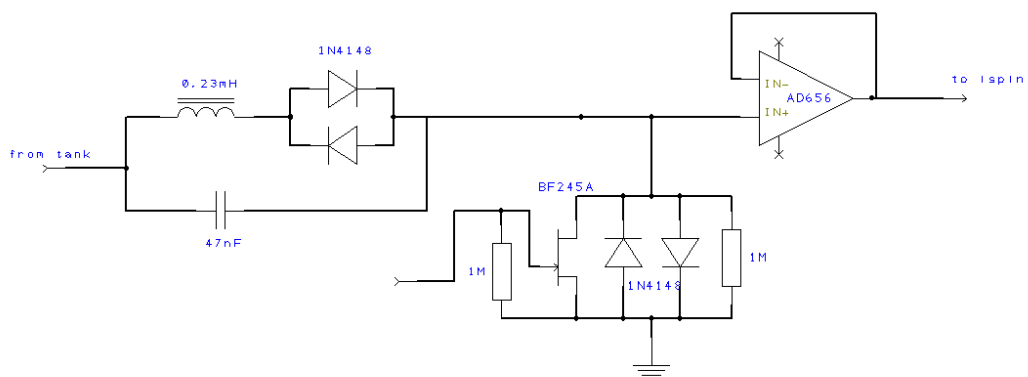


FIGURE 3.5: The tuned trap schematic with labelled component values and additional JFET circuitry included. This circuitry further lowers the signal level at V_{out} .

The signal attenuation from the tank to the tuned trap can be directly calculated by considering the resistances and the reactance of the capacitive elements (see figure 3.6) -

Reactance of coupling capacitor from tank = 6982Ω

Reactance of tuned trap tank capacitor = 69Ω

Reactance of C_{ds} of U310 = $1.43 \text{ M}\Omega$

Parallel reactance of DC bias resistor and U310 C_{ds} = $590 \text{ k}\Omega$

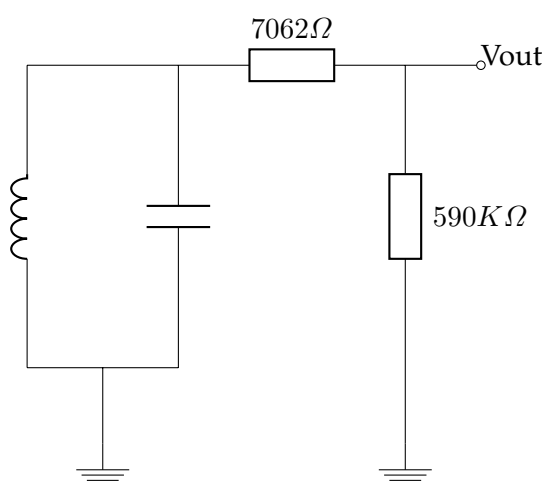


FIGURE 3.6: Equivalent reactances loading the tank circuit. Signal transfer from the tank circuit must be maximised. The equivalent reactances of the loading components are considered to ensure this condition.

The voltage out is 98% of the input signal. Hence the design of the tuned trap maximises the input signal at the cost of adding a very small amount of noise.

3.5 Transformer

The transformer is placed after the power amplifier and transforms the voltage to ensure the maximum amount of power is transferred to the tank which holds the sample. The exact amount of power needed to produce an FID signal is to be ascertained by experimentation. The transformer is made to transform the voltage by a factor of 10. It is not necessary to transform the voltage to the full 500V limit dictated by the tank capacitor rating, as energy builds up in the tank circuit over time. The transformer was wound on

a type 2 potted ferrite core gapped with kapton tape to reduce the inductance. The coil ratio is 10:1.

3.6 Helmholtz Coil

The Helmholtz coil is used to provide the static magnetic field. The apparatus consists of two coils spaced apart to create a relatively homogenous magnetic field in the centre of the two coils. The coils used were pre-existing. The Helmholtz pair was initially powered with the coils in parallel through a 60V power supply. The maximum field produced in this arrangement was 1.37mT. From Levitt [90] the Larmor frequency is

$$\omega_0 = -\gamma B_0 \quad (3.6)$$

Where ω_0 is angular momentum, γ is the gyromagnetic ratio of the sample, and B_0 is the static magnetic field strength. A field strength of 1.37mT corresponds to a spin frequency of 59KHz for glycerine. The frequency of precession can be expected to vary slightly due to non-ideal factors such as the altering of static magnetic field from neighbouring ferric parts. A frequency of approximately 50KHz was chosen for the operating frequency, so the field could be modulated around this frequency when searching for the resonance (the resonant frequency of the tank circuit was 48.5 kHz after building, so this frequency was eventually used as the Larmor frequency).

The coils were later changed from a parallel arrangement to a series arrangement. This holds the current constant through both coils, as the field generated through an inductor is equal to

$$B = \mu_0 \frac{NI}{L} \quad (3.7)$$

[88] By ensuring the current is equal through both coils the field generated is also the same for both coils. If the temperature of one coil changes with respect to the other, no field gradient occurs as the current through both is the same. The power supply used to drive the coils also needed to be changed with the coils in series. To produce the same

current – and hence the same field – the power supply was doubled to 120V. To achieve this two linear 60V power supplies were used in series. Linear power supplies were used for their low noise. Switch mode power supplies are more readily available in high voltage packages but also produce noise in a similar band to our frequency of operation.

3.6.1 Magnetic Field Inhomogeneity

The homogeneity of the magnetic field affects the captured signal. Inhomogeneity throughout the sample causes different areas to precess at slightly different frequencies. When the captured signal is viewed in the frequency domain, this has the effect of broadening the peak of the signal, referred to as “in-homogenous broadening” [69]. In-homogeneity of the static field is not the only reason this effect occurs. Nuclear interactions of neighbouring particles will also affect the magnetic field. In NMR spectroscopy, these interactions are measured carefully and provide information about the chemical structure of the sample. For this reason the broadening due to magnetic in-homogeneity must be many times smaller than any chemical shift being measured. “Most NMR experiments require a magnetic field which is homogenous (i.e. independent of position) within at least one part in 10^9 .” Levitt [90]. For the purposes of this experiment however, the homogeneity can, and is expected to, be much lower. This is because the sample is glycerine, where only one molecular type is present which will provide only one large peak. A very sharp peak is difficult to detect if the peak is too sharp. It is useful to provide a measurement of exactly how the magnetic field changes over the sample and over the entire magnetic field. The magnetic field was measured every one centimetre squared over the central region of the Helmholtz pair - 10x10x40cm. The field was measured with a commercial field meter held by a non-magnetic clamp in order to prevent the metal disturbing the field lines. Over this region the field was found to vary up to 0.23% - or 23,000 PPM - however this figure does not account for the heating of the coils, which causes the magnetic field to diminish over time. The heating of the coil is not thought to be important to the performance of the experiment, as this effect happens very gradually (the data shown was gathered over the period of approximately one hour) whereas one scan takes a fraction of a second. Over time this effect will alter the frequency of resonance, but the field is swept to prevent this

causing a problem. The central cross section of this measurement - a 10x10cm slice - is shown in figure 3.7.

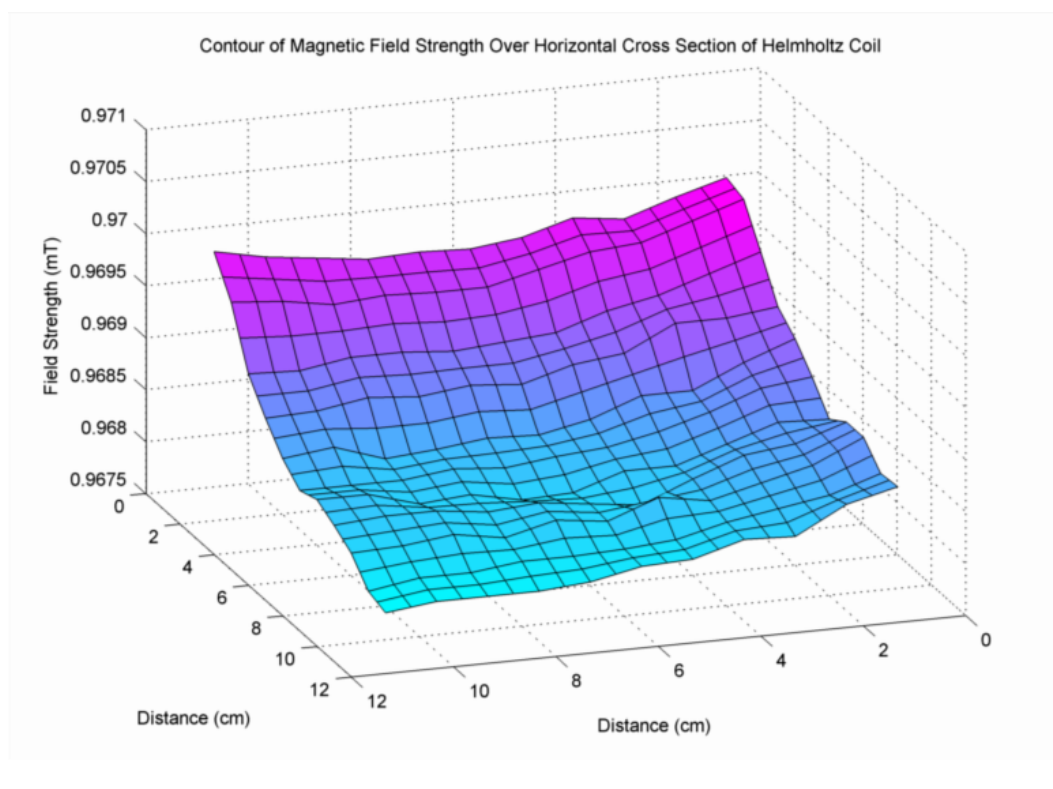


FIGURE 3.7: Surface plot of a 10 cm by 10 cm 2d horizontal cross section of magnetic field measurements over the centre of the Helmholtz Coil. The magnetic field homogeneity of the DC magnet is of great importance in the NMR experiment.

The sample occupies a smaller region of this space, and the field can be expected to vary up to 0.011% over this region. Once again, measurement is without accounting for the warming of the coils.

3.7 Electrometers

The e-field NMR technique uses electric field sensors to acquire signals traditionally acquired by magnetic field detection. These electrometers are based on the topology of the Sussex sensors. This unique sensor technology makes the electric-field acquisition possible. The design can be tailored to each of the many applications the EPS is used in. The topology of the Sussex sensors is pictured in chapter 1, figure 1.6, and figure 3.8.

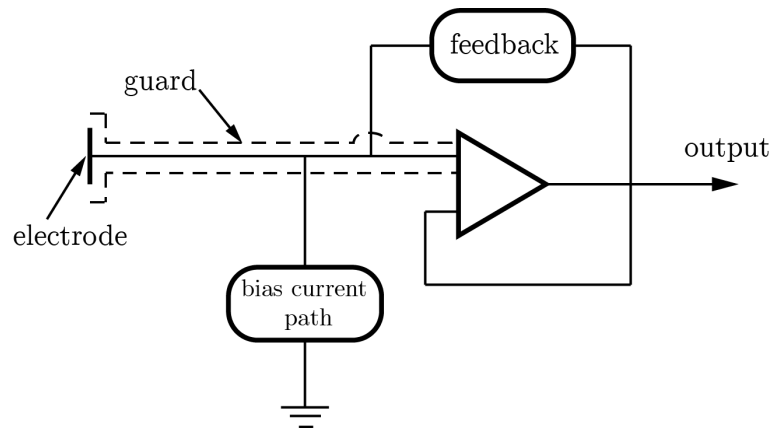


FIGURE 3.8: Generic EPS sensor topology. The op-amp is used as a unity-gain voltage follower. A bias current path is provided to stop the sensor railing and ensure correct operation of the op-amp. Feedback is used to control the potential of the guard, effectively reducing capacitance of the front end [20]

The electrometers designed for this experiment were designed for low noise and low attenuation in the experimental set-up at our operating frequency of 48.5KHz. The bootstrapping feedback is foregone as this is used for low-frequency measurements, and the bias resistor is kept as low as possible and an op-amp with low current noise is chosen - the OP657. This op-amp has low current and voltage noise. The OP657's input impedance is also optimum for coupling the signal (0.7 pF). By considering the reactances (fig. 3.9) of the input coupling, the input attenuation is calculated to be 66%. This is a large attenuation but the signal will still be very large compared to the noise floor of the electrometer.

Neutralisation is provided from a variable potentiometer on the output of the op-amp. The pot is tuned to provide the minimum signal attenuation possible without pushing the electrometer into instability - if too much signal is fed back oscillation can occur. Both electrometers are housed in a tin-plated steel box for RF shielding, and grounded by a ground braid to the star earth point. The full schematic for the electrometer is pictured in fig 3.10

3.7.1 Noise

If designed without due consideration, noise in the electrometers can become a problem. The signals being measured are expected to be at least $1 \mu\text{V}$. Because the Sussex EPS is capacitively coupled a large input resistor is needed to AC couple the signal. The input

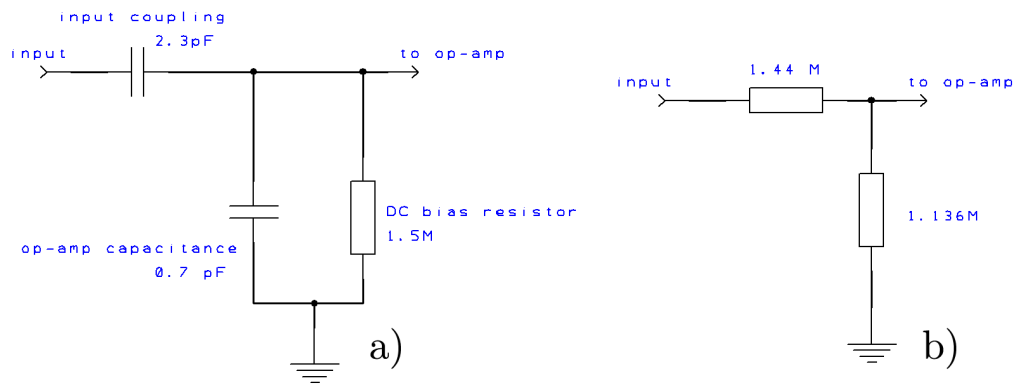


FIGURE 3.9: a) shows the input capacitances associated with the electrometer. Parasitic capacitances of the op-amp must be considered to ensure the signal is not attenuated. b) shows the equivalent loading

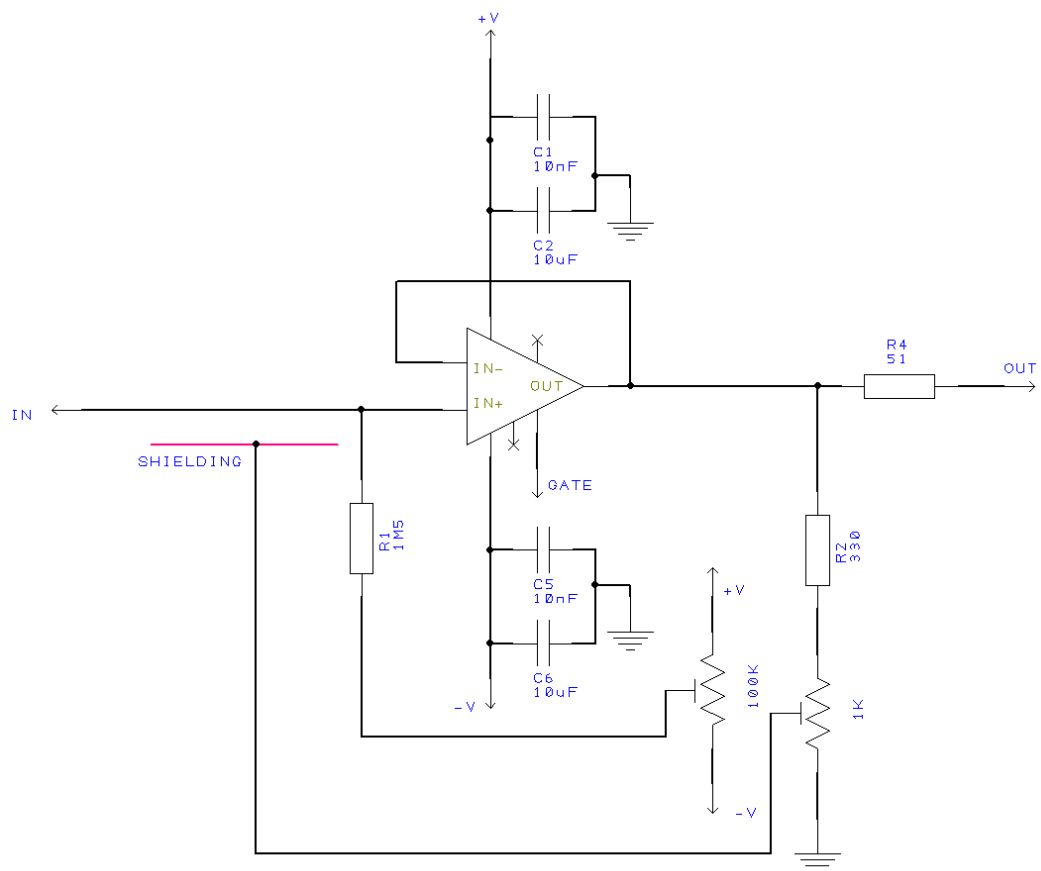


FIGURE 3.10: Full electrometer schematic for the electrometers designed for e-field NMR signal acquisition. An OP657 is used in a unity gain, voltage follower configuration.

coupling is measured to be 2.3pF, an input resistor of at least 1.4M Ω is needed to AC couple this capacitance at 48.5KHz, the precession frequency. Here a 1.5 M Ω resistor is used as the nearest preferred value. This resistance produces two noise sources, the first being thermal noise, given by [85]

$$\overline{v_n^2} = 4k_B T R \quad (3.8)$$

Where k_B is Boltzmann's constant, T is temperature and R is resistance. Which for a resistor of 1.5 M Ω at 295.15 K Equal to 0.15 $\mu\text{VHz}^{-1/2}$. This is acceptable and is not a factor that can be easily changed. The second consideration that must be made is the op-amp current noise. All op-amps have noise sources and the input noise sources can be modelled as current noise and voltage noise. The voltage noise of an op-amp will appear regardless of whatever is placed across the input. The current noise however is multiplied by the resistance to ground on the front of an op-amp to give voltage noise. Figures for both voltage noise and current noise vary dramatically from op-amp to op-amp. In general, noise figures vary between 1 and 100 nVHz $^{-1/2}$. The range of current noise is generally much larger. It is common to see figures range from fA to nAHz $^{-1/2}$. OP657s were used in the design of the electrometers. These op-amps are specified for 1.3 fAHz $^{-1/2}$ and 4.8 nVHz $^{-1/2}$. This means that the current noise in the 1.5 M Ω input resistor generates 1.95 nVHz $^{-1/2}$. This is fairly insignificant compared to the voltage noise, as the sum of two figures being random, non-periodic signals is a geometric mean

$$\sqrt{(1.95 \times 10^{-9})^2 + (4.8 \times 10^{-9})^2} = 5.18 \text{ nVHz}^{-1/2} \quad (3.9)$$

The actual noise figure as measured is slightly higher; just below 10 nVHz $^{-1/2}$. Figure 3.11 shows the measured power spectral density with a 100 μV 48.5KHz input signal. The 1/f noise floor can be seen on the left hand side of the figure as a steady increase in noise below 1KHz

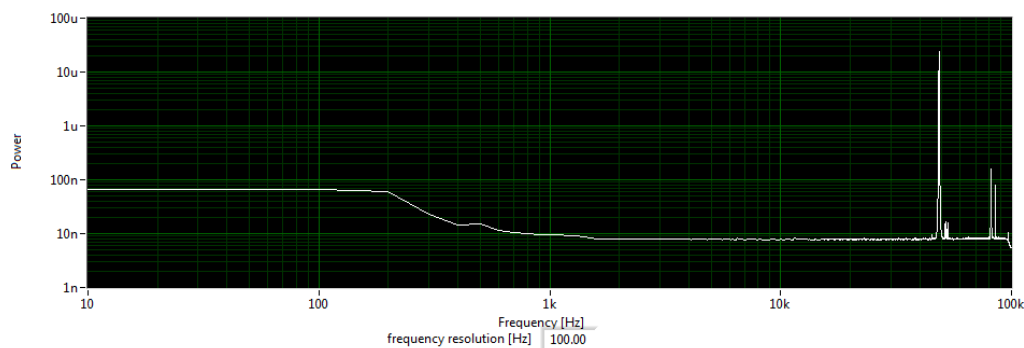


FIGURE 3.11: Power spectral density of OP657 electrometer - the electrometer is tested with a 48.5 kHz input signal and the resultant plot shows the noise floor inside the electrometer.

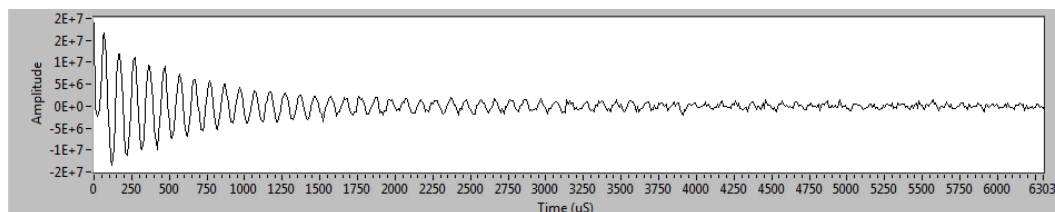
3.8 Preliminary Testing

The system was tested on a previously existing experimental set-up designed by Aydin [20]. The magnet was constructed from a iron core electromagnet, capable of producing approximately 110 mT A^{-1} and tuned to give - with a sample of glycerine - a Larmor frequency of 1.84 MHz. The correct operation of the ISpin with single pulse and CPMG sequence and electrometer signal detection were confirmed with this setup. Figure 3.12 shows single pulse and CPMG scans, with the operating frequency ω_{op} of the detector altered to see the difference in wave shape - with ω_{op} very close to the Larmor frequency only the envelope can be seen, with ω_{op} further away a clearer re-phasing echo can be seen. This is a result of the detector behaviour which mixes the signal down to a low frequency. This test confirms the adequate operation of the Ispin NMR, and all tests after wer conducted at a different frequency with the apparatus designed for a 48.5 kHz.

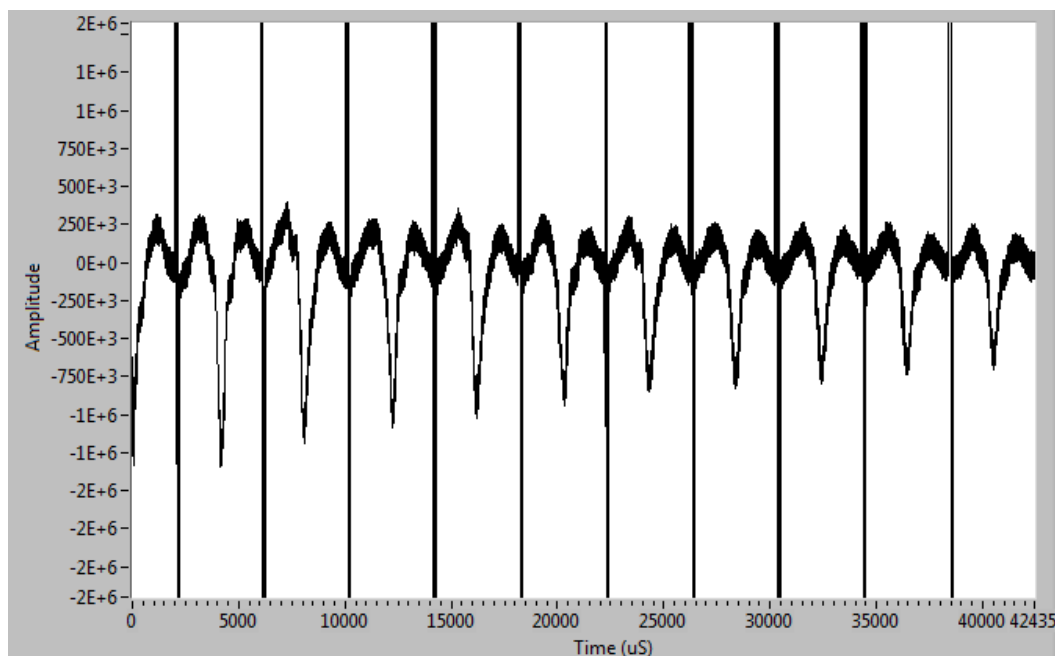
3.9 System Testing

After the construction of the experiment, capture of a FID signal proved elusive. The following outlines possible reasons why:

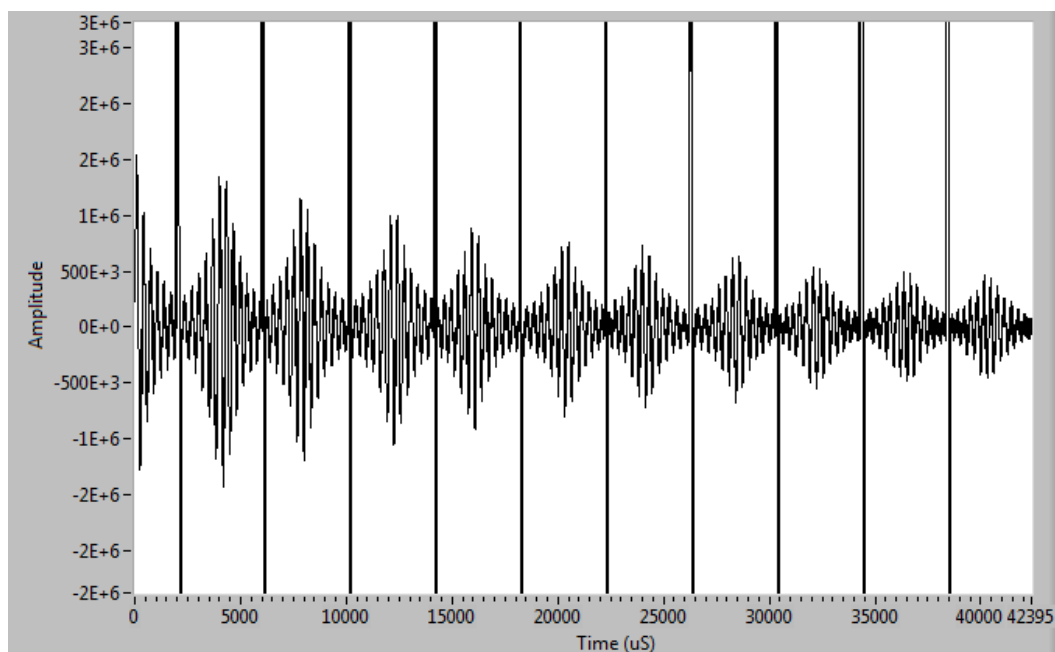
- *Power surplus* provided to the sample saturates the spin states and no signal is seen. Power is provided by the excitation pulse, too long a pulse time or a pulse of too



(a) Single pulse NMR signal



(b) CPMG sequence with receiver set near to Larmor frequency



(c) CPMG sequence with receiver set far from Larmor frequency

FIGURE 3.12: Testing the ISpin NMR system. The above figures show signals captured using the ISpin NMR system with a glycerine sample, Larmor frequency of 1.84 MHz. Figure a) shows a single pulse signal b) and c) show CPMG sequences.

great an amplitude can prevent any FID signal being seen as the spins take longer to return to their original orientations, and the FID does not occur in the time allowed.

- *Power deficit* will fail to produce a visible decay. Not enough spins change orientations and the magnetisation vector \mathbf{M}_0 is not large enough to be detected by the system. As this may occur from too short a pulse time or too low a signal amplitude.
- *Incorrect resonance* Although the magnet is tuned to produce a resonance at a specific frequency, homogeneity in the region of the sample may affect where the resonance is seen. The sharp Q of the tank circuit may contribute considerable attenuation of the FID at frequencies outside the tank operating frequency.
- *Inhomogeneity of the magnetic field* The field in the Helmholtz coil over the area of the sample was shown to have a relatively high inhomogeneity (Section 3.10). In 1996 Vathyam comments that homogeneity has been achieved in the order of 1 part in 10^9 [91]. The inhomogeneity of the Helmholtz coil over the region of the sample is 2,300 ppm. As discussed in section 2.3.1, an inhomogeneous magnet broadens the spectral width of the FID data, but there will come a point where the spins in the sample will de-phase so quickly that the signal cannot be measured. The spin echo is normally used to mitigate the effects of these inhomogeneities, but can only be utilised if the initial pulse provides a visible signal.
- *Ambient Magnetic Field Noise* is more significant when operating at lower magnetic fields as any disturbances are larger relative to the DC field \mathbf{B}_0 . The earth field was measured at $\approx 30 \mu\text{T}$ in the vicinity of the experiments which represents 30% or 30,000PPM of the earth's field. Inhomogeneity in this field and stray ambient magnetic fields presents a greater problem at low frequencies.
- *Low Frequency NMR* is inherently more difficult because the energy between the spin states - and hence the magnitude of the magnetisation vector - is proportional to the applied DC field (eq. 2.3). Tests are conducted at $\approx 48.5 \text{ kHz}$ where \mathbf{M}_0 much smaller compared to 1.84 MHz where the preliminary tests were conducted.

The steps taken to mitigate these effects are outlined in the following sections

3.9.1 Averaging Tests

This section refers to a custom oscillator designed and built specifically in order to test the correct operation of the averaging in the ISpin. This was deemed necessary to rule out any possibility that the ISpin was not functioning correctly. After the correct function was confirmed this oscillator was not used any further in any tests.

The ISpin performs multiple scans and averages the data. This eradicates noise and lowers the noise floor. A start/stop oscillator was made to confirm the correct operation of the averaging inside the ISpin. This oscillator receives an "on" signal in the form of a 5 V pulse, when the pulse goes high the oscillator outputs a sine wave of one volt peak-to-peak at approximately 50 kHz which starts at 0° phase. This function is necessary as successive averages that are not phase coherent will cancel each other.

First an analogue start stop oscillator design was made using the an integrator and Schmidt trigger topology [92]. This allows the oscillation to be stopped by shorting the integrating capacitor to ground and pulling the Schmidt trigger high or low, depending on what starting phase is desired. Upon testing this oscillator it was realised that an analogue oscillator was unable to provide low-enough frequency drift to adequately test the averaging. A digital implementation of the same oscillator was made to combat this problem. The digital implementation reads uses an AVR Atmega328P and the program operates by reading values from a wave look-up table written to represent a sine wave. The output is smoothed by a op-amp integrator with a cut-off at 80 Hz. Schematics for the analogue oscillator and code for the digital oscillator can be found in [B](#).

The use of the start-stop oscillators confirmed that the ISpin could detect input signals in the order of 1 μ V, as listed in the ISpin manual [83].

3.9.2 Labview Virtual Instruments

The NMR signal is difficult to find and the absence of a signal may be a consequence of any of the problems outlined in section 3.9 - because the exact field strengths and homogeneity of the magnet is not known exactly, the signal is searched for by choosing probable values and then performing many scans with slightly different values of magnetic field strength

(which affects the Larmor frequency) and excitation signal (which affects the power delivered to the tank). Many scans can be performed over a range of values, then sorted by computer and visually inspected for data. The extremes of field and power to the tank were widened many times during the tests, in order to minimise the possibility that the absence of signal was a consequence of power surplus, power deficit or incorrect resonance. However, unless a signal is found it is impossible to confidently assert that these factors were not a problem, only that the likelihood of their presence was minimised through the design of automated testing explained in this section.

Consideration of the problems related to Larmor frequency and energy supplied to the sample creates three variable parameters - pulse time, pulse amplitude (both of which control the energy supplied to the sample) and current through the Helmholtz pair - which controls the field in the sample and hence the Larmor frequency. These variables are hard to accurately predict and manually adjusting parameters between scans is laborious and inaccurate. Labview software enables the design of a custom virtual instrument (VI) to automatically adjust parameters in between scans and perform scans over a large range of variables. Furthermore, the VI enables all resulting data to be systematically opened, a Fourier transform performed, and a measure of the signal-to-noise ratio of the largest signal recorded in the file name. This creates a folder with each piece of data ordered by those most likely to contain a signal first. This folder is then opened and the files can be manually viewed one by one. This process simplifies the capture and viewing of many data files immensely.

There are three parts of the VI -

- *Scan* all arguments needed for the operation of the Ispin are collected and a batch file is run via a command prompt with the relevant arguments supplied. The various parameters are entered on the front screen of the VI and the software automatically enters each successive piece of information into the batch file. Each resulting scan is stored with a file name that distinguishes its salient parameter settings.
- *Sort* The VI opens the files one by one, performs an FFT, picks the highest frequency peak and finds the signal to noise ratio at that peak. The file is re-written with a new name that indicates the signal-to-noise ratio at this peak.

- *View* each file is opened in turn, the user can flick back and forward through the scans. Scans are ordered in terms of their signal-to-noise ratio and those with the highest - most likely to contain a signal - are viewed first to save time.

Screen shots of the VI GUI and the inner workings are contained in [B](#). Conducting many scans over a wide range of pulse times, powers and magnetic field strengths eliminates uncertainty over power and Larmor frequency. While it cannot be proven that the scans are being performed with the correct energy, a sensible prediction can be made, then by searching above and below this point the scans become more rigorous. When no signal was found the highest and lowest points were changed to allow searching over an even wide range, in this way the possibility of error from power deficit and surplus and incorrect resonance is minimised.

3.9.3 Proton Magnetometer

A proton magnetometer was designed as a means of testing a second NMR system in low-field conditions. The construction of the proton magnetometer was inspired by the articles by Hollos [[93](#)], Duggard [[94](#)] and Ruhunusiri [[95](#)].

The operation of the magnetometer is discussed in section [2.2.2](#). The apparatus consists of a large polarising coil (giving $\approx 4.45 \text{ mT A}^{-1}$ - see [fig 3.14](#)) used to generate a strong magnetic field and two detector coils which sit inside the polarising coil ([fig. 3.15](#)). These are used as pick-up coils made to fit the width of a test tube and are wired differentially with a capacitor to cancel ambient noise and produce a resonant tank. A glass tube filled with the test sample is inserted into one of the coils. The capacitor in the setup was a variable switch box capacitor used to tune the \tan to the operating frequency of the experiment. The schematic diagram of the experimental setup is pictured in [figure 3.13](#): The coil arrangement consists of two receiver coils wired differentially inside a larger magnum coil which provides a large magnetic field to polarise the spins. The receiver coils form a resonant tank with a separate variable capacitance box, this box is tuned to the Larmor frequency. A variable power supply is used to provide current to the magnum coil which is switched through the coil for three seconds, then left for 15 seconds for the sample to relax. The control unit operates the switching by the use of a MOSFET and also

includes diodes to counter the effects of back E.M.F. induced in the coil when the current is switched off. A function generator controls the timing of the switching and also triggers the oscilloscope to read the data from the tank circuit, so the readings may be averaged. All wires are shielded to reduce unwanted noise..

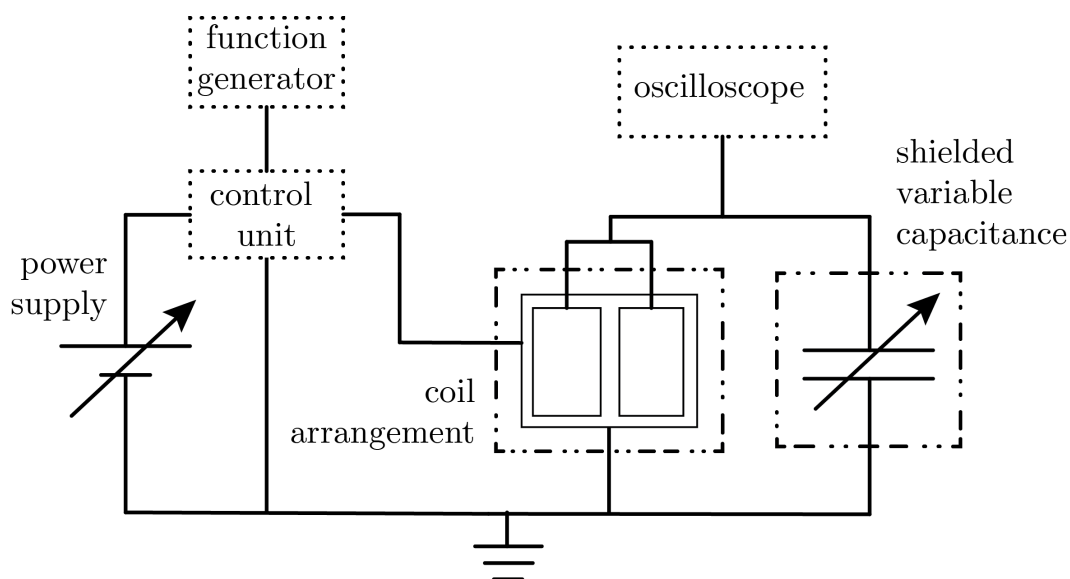


FIGURE 3.13: Proton magnetometer experiment. The setup is analogous to the pulsed NMR setup but does not require timed pulses and only DC magnets.

TABLE 3.1: Proton Magnetometer Coil Measurements

Coil	wire (mm)	turns per layer	layers (mm)	L	Q 2 kHz	Length (mm)	Diameter (mm)
coil 1	0.58	138	4	3.43 mH	9.4	94	32
coil 2	0.58	138	4	3.40 mH	9.5	94	32
magnum	1	98	6	25.68 mH	55	100	88

The polarising coil is fitted with protection diodes to stop back EMF damaging the surrounding circuitry when the current through the coil is switched off suddenly. A FET (an IRF6215 [96]) is used to switch 3 A of current into the coil for 4 seconds, then turn off for 15 seconds. This process is automated by a signal generator which feeds a 15V gate pulse to the FET, and an oscilloscope is set to trigger on the falling edge. The signal from the tank is low-pass filtered to show the envelope of the signal and fed to the oscilloscope which averages the noise out, thereby extending the noise floor of the system. The apparatus is oriented with the magnetic field lines through the inductor at 90 degrees to the earth field lines, which were tested with a commercial magnetometer by measuring the field strength at various angles.

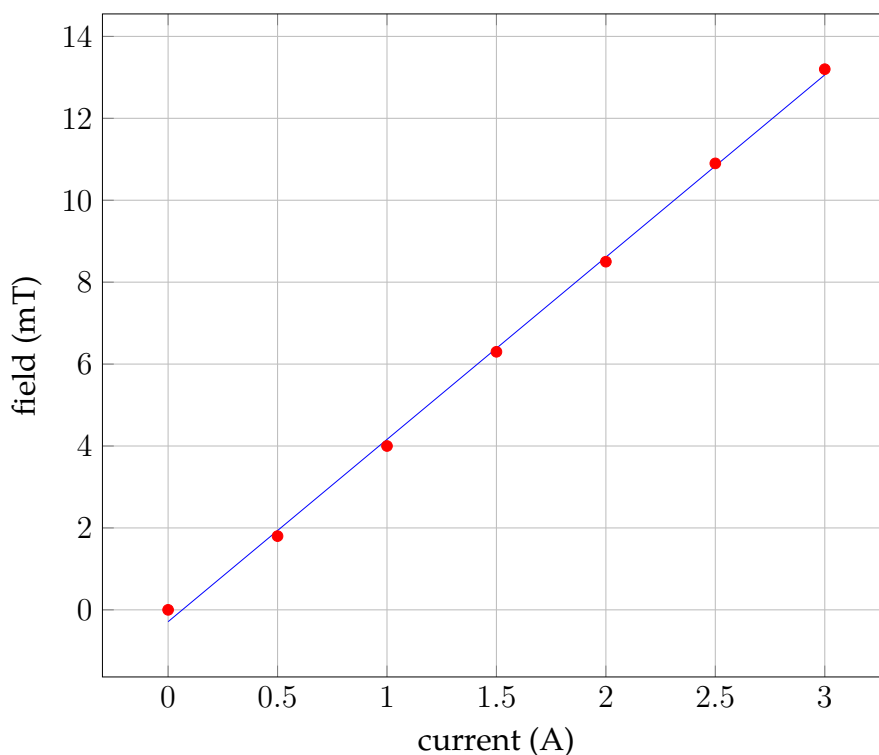


FIGURE 3.14: Magnetic field inside the proton magnetometer magnum coil as a function of current through the coil

The signal from the proton magnetometer is much smaller than the signal from the pulsed NMR experiment, owing to the relatively small magnitude of the earth's magnetic field ($\approx 20 \mu\text{T}$). This means extensive averaging is required to see even a small signal. Hollos [93] recommends digitising the data and using an FFT to extract salient information about the frequency, the experiment constructed in this thesis was tested by extracting the envelope data of the ringdown, extensively averaging it and comparing it to the signal of the same system without the sample present.

3.9.4 Results of Proton Magnetometer Tests

The comparison of results from the proton magnetometer experiment is displayed in figure 3.16. It shows that there is a slight difference in the ring down time of the tank circuit, consistent with the presence of a signal. However, these results were replicated with the tank tuned to a different frequency from the Larmor frequency (this is pictured in fig. 3.17), and therefore it is decided that this difference is not the result of a FID signal.

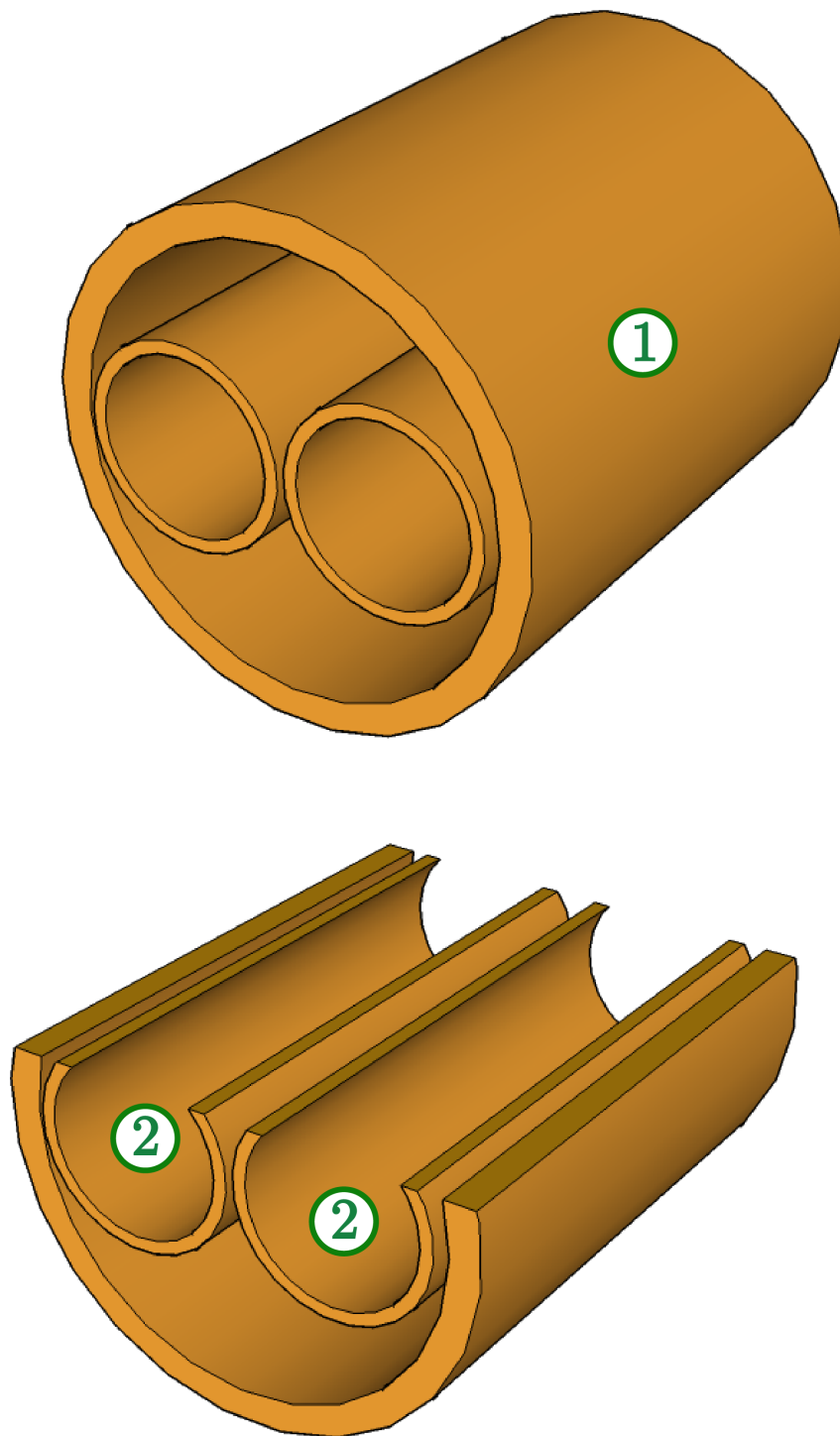


FIGURE 3.15: Proton magnetometer assembly - the top figure shows the larger coil (1) which provides the static DC field with the two smaller receiver coils (2) sitting inside it - the lower figure shows the same assembly with a cut section

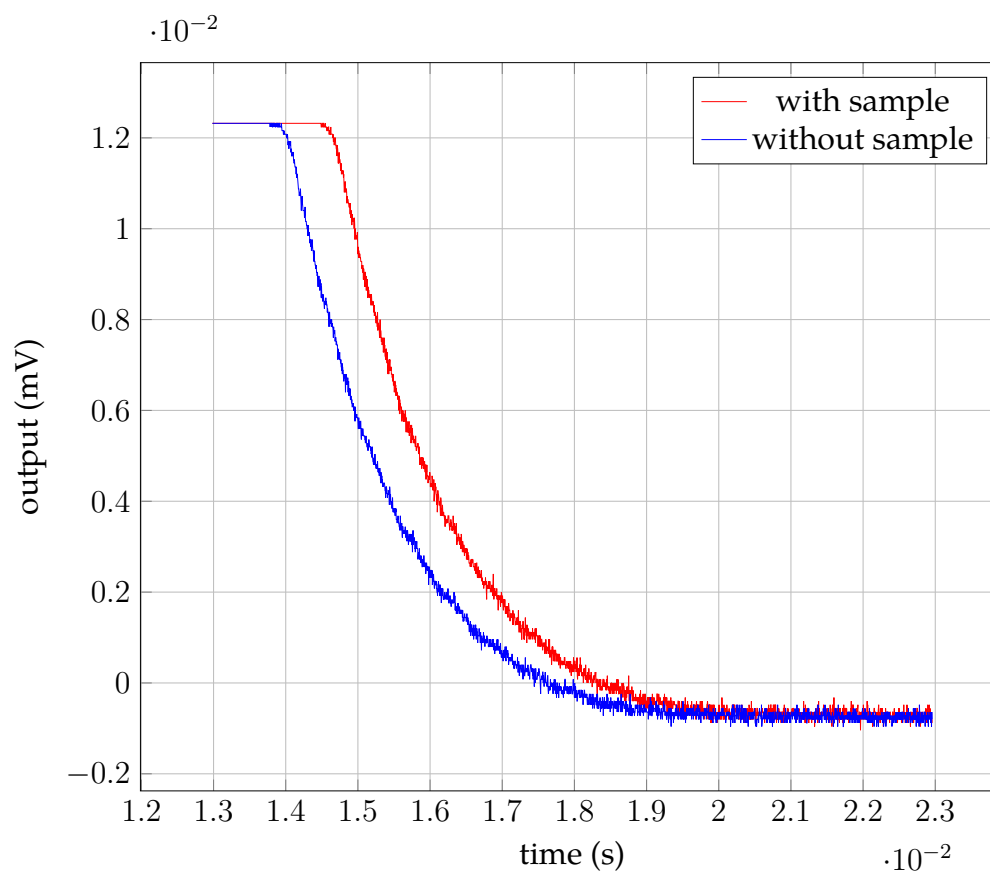


FIGURE 3.16: Results of the proton magnetometer experiment. A clear difference in the ring-down times is recorded with a sample present and not present

3.10 Conclusions

The tests undertaken eliminate most of the variables outlined in 3.9. This is done by taking extensive scans with a custom automated VI. As discussed in section 3.9.2, the use of this automated testing minimises the likelihood that the problem factor is either an incorrect resonance or problems with the power delivered to the tank. This leaves the following as the most likely factors.

- Magnetic field inhomogeneity - the magnetic field of the Helmholtz coil is too inhomogeneous. As has been measured in section , the homogeneity of the field is very low compared to that expected in a conventional NMR spectrometer. Low homogeneity may mean the phases of the individual spins are not sufficiently in phase to produce a detectable magnetic moment.

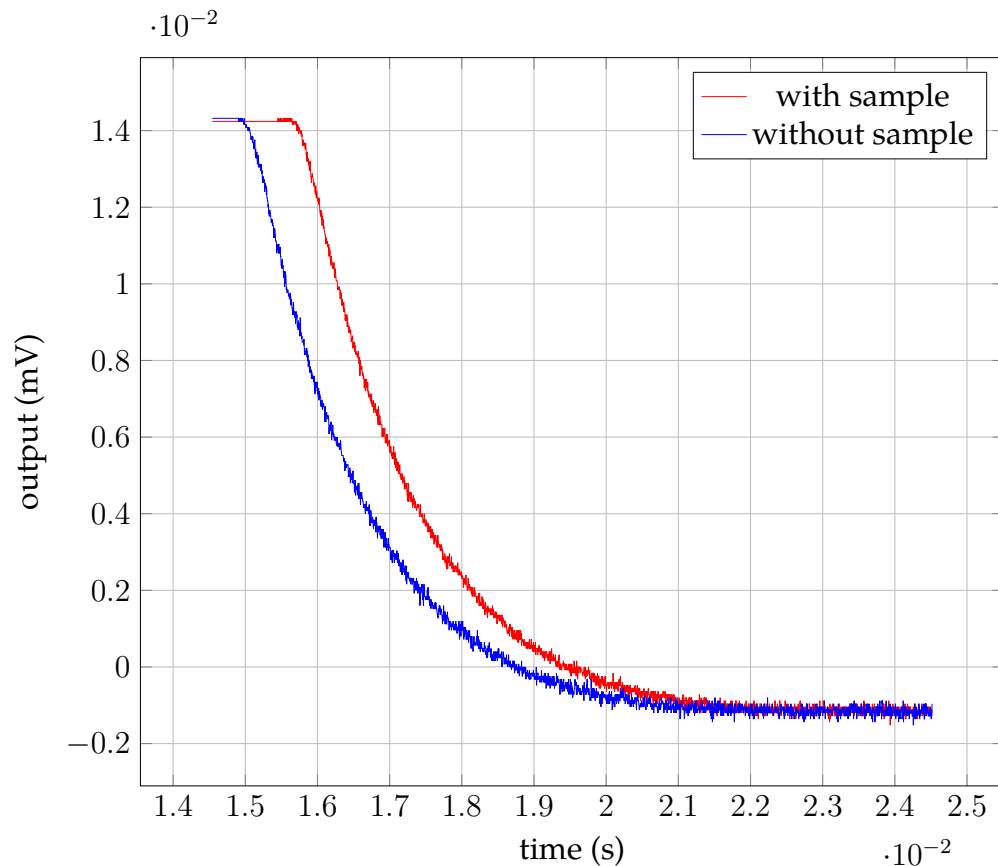


FIGURE 3.17: Results of the proton magnetometer experiment with tank circuit tuned to a different frequency than the Larmor. The difference in the ring-down times is still present with and without sample present.

- Size of the resulting signal is too small - although the premise of the NMR detection has been proven by Aydin [20], these tests concentrate on using far lower magnetic field - creating a Larmor frequency of 48.5 kHz rather than 2 MHz signal created in low field NMR conditions is known to be much smaller, as the signal level is proportional to the applied field strength (discussed in Chapter 2, section 2.1.4). This may mean the signal created by the magnetisation vector produced by the field inside the sample is in the sub- μV region, too small to be detected by the ISpin. This signal level is documented in the ISpin manual [83] and is above the noise floor of the electrometers measured in section 3.7.1, making the ISpin the piece of equipment in the detection with the highest noise floor.

The proton magnetometer was intended to show that even though the pulsed NMR system may not produce signals, the EPS sensors would be well suited to capture the signals

created by nuclear precession. In fact, the proton magnetometer may have been suited only to an outdoor environment: Chung [97] refers to the magnetic field perturbations created by buildings with steel structures, while Skakala [98] and Afzal [99] record significant field disturbances in indoor unshielded environments. These disturbances are likely to be high in a research building with many sources of magnetic noise. The Faraday cage that the experiments were conducted in will provide protection only from electric field disturbances and not from magnetic field disturbances. Indeed, Afzal [99] records magnetic field perturbations in the presence of the perturbation source of up to 40 μT . It can therefore be said that the most likely cause of the failure to produce signals is ambient magnetic field noise.

The eventual failure of the experiment does not indicate the EPS is unsuitable for low-field NMR, as no signals were detected at low frequencies using either magnetic or electric field detection. Suggestions for further work on this experiment are as follows -

- Substitute the Helmholtz coil with a higher homogeneity magnetic field. This would reduce the likelihood that the homogeneity is the problem.
- Modify the Ispin front end electronics to produce higher signal to noise ratio of the detection electronics. This would reduce the likelihood that the signal level was the problem with the system.

Chapter 4

Particle Detection Theory

4.1 Overview

With minor modifications the EPS can be used as a particle detector. This thesis will focus primarily on the behaviour of a parallel plate ionisation chamber where a volume of air between the plates is irradiated by alpha particles. Most of the experiments in this thesis cover the EPS functioning like a traditional ionisation chamber in current mode, but as an extension of these, experiments are undertaken to attempt to make the detector function as a pulse mode device by manipulating the rise time of the sensor. This chapter provides the theoretical basis for these experiments. This chapter covers the theory of charged (alpha) particle detection in current mode ionisation chambers (sections 4.3 to 4.4.6); proportional and Geiger Muller detectors; neutron detection and converter layers (sections 4.6); and special considerations for the EPS, covered in section 4.7.

This thesis focuses on expanding the potential applications of the EPS sensor and provides a proof of concept for use in particle detection applications. The EPS is especially useful as a particle detector as it is cheap and small - the working of the sensor exists as a monolithic 1cm^2 chip designed by Plessey. This means the sensor may be fitted into small spaces where existing sensors cannot fit, requiring only enough space for an electrode assembly. Additionally, the sensor offers built in control of feedback which will be shown in chapter 5 to affect the rise time of the sensor. Further work on this area may mean a sensor which can be switched from current mode to pulse mode behaviour may be developed.

This distinguishes this work from recent research in the area such as that of Takata [26], Bellicoso [27] or Aladili [28].

4.2 Design of Particle Detectors

According to Leo [100, p.116], the design of an effective particle detector takes into account four main factors

- **Cross section for reactions in the detector** The detection of particles normally relies on the creation of charged particles [101, p.10]. It is these particles which are then detected and measured. This thesis primarily covers the transferral of kinetic energy to charge which occurs in the interaction of alpha particles with air - in the ionisation chamber experiments - and the interaction of neutrons with various detector materials in the neutron detection experiments. Those materials in which particles react are chosen because they have a high likelihood of interacting with a particle. Cross section quantifies the chance of an interaction between a particle and the material it passes through (charged particles, including alpha particles interact primarily through Coulomb interaction [102, p.96],[103, p.2] while neutrons through strong force interactions with nuclei [100, p.63]) and has the unit of barns. The detector must utilise a material with a high cross section for the particle it is trying to detect.
- **The detector mass** In addition to choosing a material with appropriate cross section, the material must also be of sufficient mass to absorb all or sufficient amount of a particles energy. A useful figure here is the range - defined as the average distance a specific particle with a certain energy can travel through a certain density of material (measured in kg cm^{-2}), before it loses all of its energy [104] [100, p.30].). This figure will vary experimentally due to the unpredictable path and interactions of a particle in a material (this effect is called range straggling [105, p.45]), so some approximation is used in calculation, the most common being the practical range [100, p.31].
- **Inherent detector noise** The amount of energy produced in reactions between particles is often small and the equipment used to detect the charged particles produced

must be sufficiently low noise that they might be seen above the noise floor of the equipment.

- **Protective material surrounding the sensitive volume of the detector** The material through which particles travel into the sensitive volume of the detector must be designed as to interact as little as possible with the particles, preserving their energy. In this thesis, the surrounding volume must also provide adequate electric field shielding, as discussed in section 4.6.3.

4.3 Charged Particle Detection in Ionisation Chambers

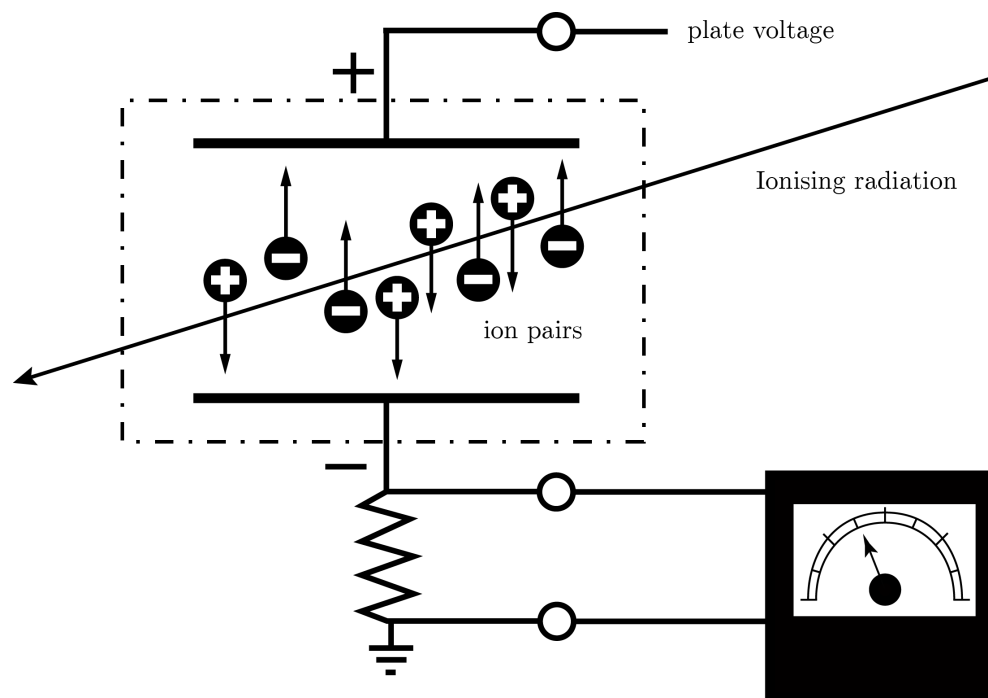


FIGURE 4.1: Parallel plate ionisation detector showing the separation of ions. Incident radiation creates ion pairs in the captive volume of gas represented by the dotted box. An electric field applied between the plates moves the ion pairs, the induced voltage is measure by an electrometer. [106]

This section provides an overview of the function of ionisation chambers, before discussing the relevant processes in greater detail in section 4.4.

Figure 4.1 shows the schematic of a parallel plate ionisation chamber - there are two plates, cathode and anode, between which a voltage is applied and an electric field exists. The space between the plates is accessible to air and to incident radiation. Incident particles

ionise air molecules creating ion pairs - free electrons and positively charged ions, which migrate to either electrode under the influence of the electric field. The movement of the charges induces a voltage over the resistance and is read by an electrometer. Hence, gas filled ionisation chambers detect ionisation produced in gas by incident charged particles [100, p.127],[101, p.52].

Without the applied voltage the ion pairs created may recombine, reducing the signal [107, p.134]. The electric field attracts the charges to either plate, separating them,[107, p.135],[103, p.90], hence the effects of recombination are decreased and the more efficiently the charge in the volume is measured[38]. When increasing the voltage further does not increase the signal, the "saturation region" is reached and a measurement of the incident radiation may be inferred [107, p.136]. When the voltage is increased further the behaviour of the ions in the gas changes and as more voltage still is applied, the behaviour changes continually. There are in total 6 types of behaviour observed between ground and a high enough voltage to precipitate a continuous discharge in the gas (see figure 4.2). The six regions of collector behaviour are:

1. *recombination region* In this region most of the ion pairs created recombine. As more voltage is applied, the pairs are separated faster and less recombination takes place.
2. *saturation region* When enough field is applied, most of the ion pairs created are collected. When this region is reached, the amount of incident radiation can be inferred.
3. *proportional region* further increasing the field causes the electrons to gain enough energy to ionise other molecules. The amount of electrons collected is proportional to the ions produced in the chamber.
4. *region of limited proportionality* like the proportional region but the movement of electrons is increased such that the positive ions present are almost immobile, which creates non-linearities in the measurement. Detectors do not operate in this region
5. *Geiger-Muller region* In this region any discharge will continue until the electric field of the immobile positive ions prohibit it and consequently all incident particles produce the same pulse height.

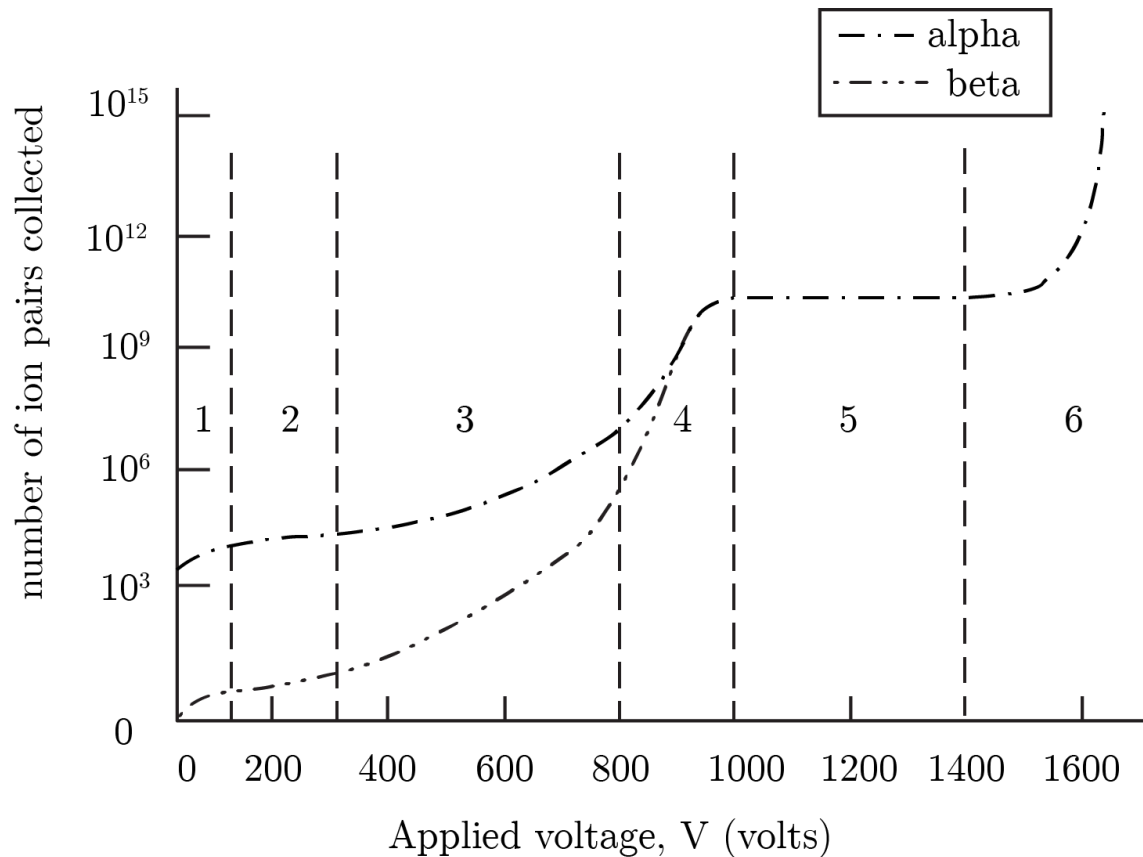


FIGURE 4.2: Operational regions of conventional ion chambers. Electric field over a volume of gas precipitates 6 distinct behaviours, depending on the voltage applied [108]

6. *Continuous discharge region* The voltage on the plates is increased sufficiently that there is a steady current through the gas.

The ionisation chamber, the proportional detector and the Geiger-Müller detector are three types of detector all designed to work in different regions of applied voltage [105, p.206],[107, p.161]. In the saturation region, the detector works as an ionisation chamber. Current mode detectors are not used to detect individual particles. The proportional counter, a pulse mode detector which works in the proportional region, accelerates free electrons enough that they may ionise molecules by secondary ionisation [109, p.47], which increases the amount of ion pairs produced per incident radiated particle. The output is proportional to the energy of any incident particle [100, p.136] and proportional detectors can be used to count these particles and distinguish their energy. The Geiger-Müller is also a pulse mode detector and functions in the Geiger-Müller region. In this region even low energy particles precipitate an avalanche of electrons, causing the

detector to saturate [109, p.53]. The signal from such a detector has no relation to the primary ionisation [109, p.53], hence it can count low energy particles but cannot be used to measure their energy.

4.4 Mechanisms of Ionisation Chambers

This section covers in greater detail the processes relevant to this thesis which enable the detection of charged particles in parallel plate ionisation chambers.

4.4.1 Ionisation and Excitation

Ionisation occurs when an electron is removed from the outer shell of a molecule or atom. This occurs as a result of various interactions between particles but in the particular case of charged particle radiation, the most significant is the Coulomb interaction [102, p.96],[103, p.3]. Coulomb's law gives the force of attraction between two bodies -

$$f = \frac{kq_1q_2}{r^2} (V) \quad (4.1)$$

Where k is Coulomb's constant (dimensionless), q_1 is the charge on the first body (C), and q_2 is the charge on the second body (C) and r is the distance between the bodies (m). When a charged particle moves through the air in an ionisation chamber, there is a force of attraction between it and neighbouring charges. The force between the electron and incident particle can cause the electron to be excited - the electron may stay bound to the nucleus, but become excited - if the force is insufficient to free it. If the force of attraction is sufficient an electron is freed: the molecule is ionised. The term ionisation energy (or binding energy, or ionisation potential) is used to quantify how much energy it takes to separate an electron from its nucleus, however if the total energy of the interaction between a molecule and a charged particle is considered, the energy is higher, as energy is absorbed by the other electrons bound to the nucleus [103, p.13]. The value W is used to represent this total energy needed to ionise a molecule. For gasses, the W value is around 30eV [105, p.207] [103, p.14] (see table 4.1). The amount of ion pairs created for a 5 MeV alpha particle is therefore around 16.67×10^4 , however considering that the value

W is actually an average, potentially ionising interactions are potentially higher or lower for each interaction. The Fano factor is used to calculate this variance. The Fano factor is important in detectors used to measure the energy of individual ionising events [100, p.117], but has no significance in current mode detectors (as in this thesis) [107, p.133].

TABLE 4.1: "Compilation of some properties of gases. Given is the average effective ionisation potential per electron I_0 , the average energy loss W per produced ion pair, the number of primary (n_p), and total (n_t) produced electron-ion pairs per cm at standard pressure and temperature for minimum-ionising particles" [103, p.14]

[0.1 ex] Gas	Density (g/cm ³)	I_0 (eV)	W (eV)	n_p (cm ⁻¹)	n_T (cm ⁻¹)
H ₂	8.99·10 ⁻⁵	15.4	37	5.2	9.2
He	1.78·10 ⁻⁴	24.6	41	5.9	7.8
N ₂	1.25·10 ⁻³	15.5	35	10	56
O ₂	1.43·10 ⁻³	12.2	31	22	73
Ne	9.00·10 ⁻⁴	21.6	36	12	39
Ar	1.78·10 ⁻³	15.8	26	29	94
Kr	3.74·10 ⁻³	14.0	24	22	192
Xe	5.89·10 ⁻³	12.1	22	44	307
CO ₂	1.98·10 ⁻³	13.7	33	34	91
CH ₄	7.17·10 ⁻⁴	13.1	28	16	53
C ₄ H ₁₀	2.67·10 ⁻³	10.8	23	46	195

The free electron and the positive ion are now separate, equal and opposite charges and the kinetic energy of the incident particle is minus the energy of the Coulomb interaction. Thereafter the particle continues to travel, excite and ionise molecules. Charged particles are slowed by their interaction with electrons, and scattered by their collisions with nuclei [102, p.106]. As the particle continues on its path its energy decreases through each interaction. The Specific Primary Ionisation refers to the "number of primary ionisations produced by an ionising particle per unit path length in an irradiated medium" [110]. Both of these two are measured averages, as the amount of interactions along the path of a particle will not be constant, depending on the unpredictable motion of molecules in gasses.

Electrons freed through Coulomb interaction by an energetic charged particle may gain sufficient kinetic energy through the interaction that they travel away from the point of origin - these are called delta electrons or delta rays [102, p.97]. Delta electrons may have enough energy to cause ionisation themselves, an effect called secondary ionisation [102, p.97]. The amount of energy lost through Coulomb interactions changes along a particles

range, and reaches a maximum toward the end [111, p.31]. This peak occurs while the particle still has enough energy to ionise but is travelling slowly, maximising the time it will spend in the vicinity of an electron. This is illustrated in figure 4.3, which shows the specific ionisation (the number of ion pairs created per unit length of the particles range) of an alpha particle in air as a function of distance to its end range. The point at which the maximum amount of ion pairs are created is called the Bragg peak [112].

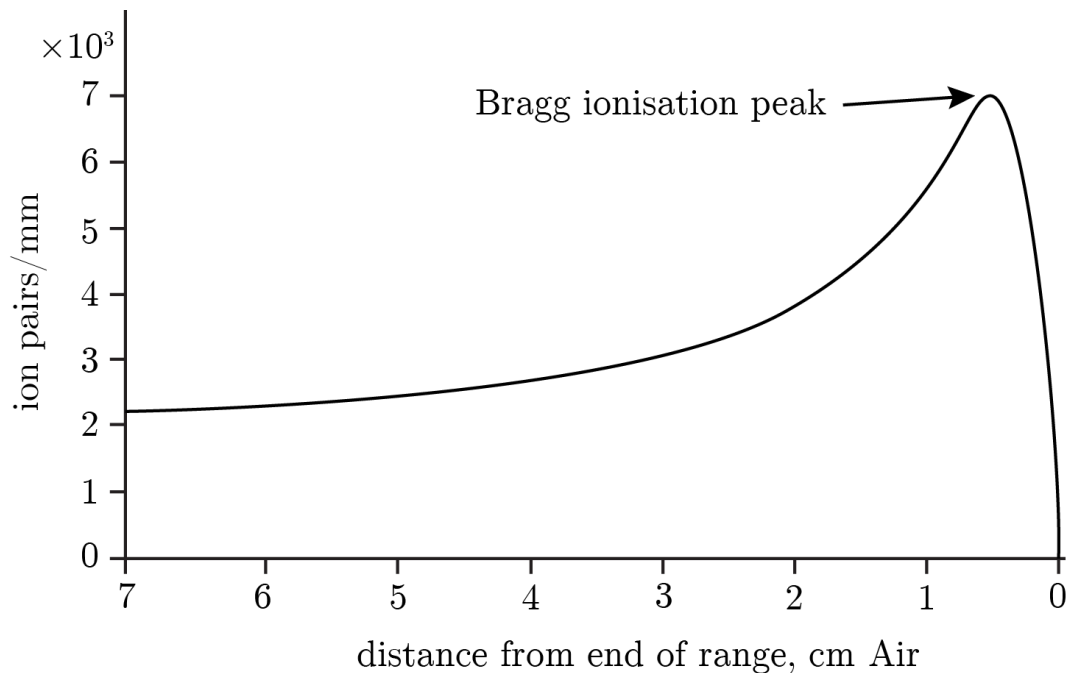


FIGURE 4.3: "specific ionisation (ion pairs/mm) as a function of distance from the end range in air for a 7.69 MeV alpha particle." [112]

The area under the curve in figure 4.3 represents the total energy of the alpha particle. The x axis represents the distance from the end of the range. In materials with greater stopping power (a measure of how much a material attenuate) A material with a low alpha range will cause an alpha particle travelling through it to lose all its energy in a short distance.

4.4.2 Separation of the Ion Pairs

In order to use an ionisation chamber to make an accurate measurement of a radioactive source, the amount of ion pairs - the charge - created in the volume between the plates is measured. This is complicated by recombination processes: opposite charges are likely to recombine if they remain in the same vicinity [107] (factors affecting recombination

in a chamber is covered in section 4.4.3). The pairs are separated by the application of an electric field: when a large enough voltage is applied to the plates, the recombination effects are minimised and the detector operates in the saturation region [100, p.129][107, p.136].

Ion pairs created between the plates of an ionisation chamber experience either an attractive or repulsive force (depending on their polarity) from the field between the plates. They gain kinetic energy: electrons move toward the anode, and the positive ions toward the cathode. Korff states the velocity of the electron is between 10×10^3 to 10×10^4 times greater than that of the ion [108, p.37] in the same electric field, owing to the electrons much smaller mass. This movement induces a charge on either electrode. When charges move toward the plates, charged clouds of ions are created around the plates [38], in these regions the effects of recombination are low. Hence, when a field is applied ion pairs are separated and attracted into regions where the possibility of recombination is much lower, reducing the overall rate of recombination.

Figure 4.4 shows the how the applied field affects the concentration of ions around the plates. This effect is seen in all ionisation chambers. Space charge refers to "clouds" of charge around the plates which have the ability to repel and attract charges (figure 4.4). Positively charged ions cluster around either plate the -ve plate, their concentration being represented by the diagonal line that ends $\frac{fqd}{k_1 \frac{v}{d}}$, and the negative ions cluster around the plate, concentration being represented by the diagonal line that ends $\frac{fqd}{k_2 \frac{v}{d}}$. The ion pairs travel with a velocity of $k_x \frac{v}{d}$, where k_x represents the mobility of the particle and $\frac{v}{d}$ the electric field. At any point x between the plates, the relative concentration of ions is represented by the difference in the heights of the lines (space charge).

4.4.3 Recombination Effects and the Saturation Region

This section covers the different types of recombination which affect the ion pairs in the chamber. Knoll [107, p.137] states there are three main ways in which this happens

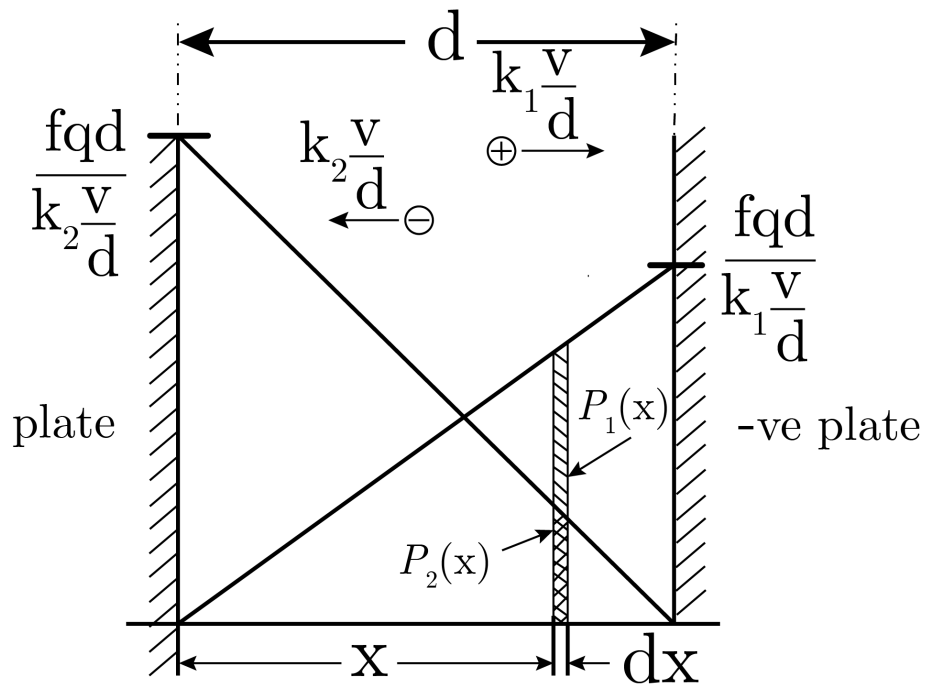


FIGURE 4.4: Geometric interpretation of the distribution of positive and negative ions in parallel plate ionisation chambers. A field is applied between two plates distance apart which separates charges in the volume [38]

- *General recombination*

As the free electrons move through the irradiated volume of gas they collide with positively charged ions. When these two collide the charge is neutralised.

- *Initial Recombination*

At the instant an ion pair is created an electron and a positively charged molecule are in close proximity. Therefore there is a probability that the two will recombine shortly after the pair is created.

- *Ionic diffusion*

Ions diffuse against the electric field. The creation of ion pairs creates a gradient of charge in the gas and the ions migrate away from areas of high concentration. These effects are mitigated by the application of an electric field. When a greater field is applied, the ion pairs move more quickly toward the plates, reducing the time they have to recombine and reversing the effects of migration.

Recombination effects are reduced by increasing the electric field over the ionised volume, which attracts the ions to the plates faster [107, p.135]. As the field increases the number of ion pairs that recombine inside the chamber reaches a saturation point where all - or the maximum (some recombination is always present) - ion pairs created are preserved and the charge measured. The voltage needed to produce this effect varies depending on the amount of charge created in the chamber (proportional to the rate of irradiation), the distance between the plates and the voltage applied between the plates [38] (this is covered in more detail in section 4.5).

4.4.4 Signal in Ionisation Chambers

In a current mode chamber, the drift of the electrons constitutes an electric current. When recombination in the chamber is reduced, the measured signal increased. The peak value of the voltage produced in response to an incident particle in an ionisation chamber is equal to

$$v = n_0 e \quad (4.2)$$

[107, p.154] Where n_0 is equal to the number of ion pairs created in the volume and e is the charge on an electron. The maximum number of ion pairs created within the volume from a 5 MeV alpha particle will be

$$n_0 = \frac{E_0}{W} = \frac{5 \times 10^6}{30} = 0.17 \times 10^6 \quad (4.3)$$

Where E_0 is the energy of the incident particle (in this case 5 MeV) and W is the total ionisation energy, taken to be 30 eV (see section 4.4.1). Combining 4.2 and 4.3, and using the value of 100 pF (The value which Knoll gives for the value of a typical ionisation chamber capacitance [107, p.154]) gives

$$V_{max} = \frac{(0.17 \times 10^6)(1.6 \times 10^{-19})}{10^{-10}} = 2.72 \times 10^{-4} \text{V} \quad (4.4)$$

Ordinarily this would be difficult to detect as it is buried in the noise floor, however if the front end RC constant can be reduced sufficiently this value will increase accordingly to

a larger value, this is pulse mode operation. Alternatively, the integral signal from many events can be measured - current mode.

Inside the ionisation chamber, electrons freed by incident particles are attracted toward the front electrode. These electrons move over the front end resistance to ground. The signal measured is caused by the movement of these electrons, but is induced on the front electrode by charges moving towards it [107, p.813],[113]. Consequently a signal appears from the EPS at the moment the charge is created, and gets larger as the charges move toward either electrode. This effect was discovered independently by Shockley [114] and Ramo [115]. The theorem states that the instantaneous current on a given electrode is equal to

$$i = q\vec{v} \cdot \vec{E}_0 \quad (4.5)$$

Where q is the charge, \vec{v} is the velocity and \vec{E}_0 is the weighting field. This weighting field is found by solving the Laplace equation for the detector geometry in question. In this thesis, the detector geometry is a cylinder, so the solution for the centre cross section can be found in 2D Cartesian coordinates, with boundary conditions - the electrode on which the charge is induced is set to 1 and all other boundaries are set to 0. This is in agreement with the detector described in section 4.6.3, where the grid and shielding is held at a potential with respect to the front electrode. See figure 4.5 for a surface plot of the weighting field inside the grid assembly (the grid assembly is discussed in section 4.7), the surface plot was created in Matlab, using Fourier coefficients as a solution to the Laplace equation, then by plotting them over a 2D grid.

The energy contained within the chamber is equal to the energy stored between the plates of that capacitor. This energy attracts the positive and negative ions to the plates and work is done. The total energy between the plates is less the amount of energy it takes to attract the charges, the difference appears as V_R . If the movement of the electrons can be represented as n_0e and the movement of the positive charges is $-n_0e$, the voltage induced is equal to n_0e . The movement of the positive charges *away* from the front electrode and the movement of electrons *to* the front electrode both contribute to the voltage on the electrode, however for most ion pairs created the majority of induced charge will be from the

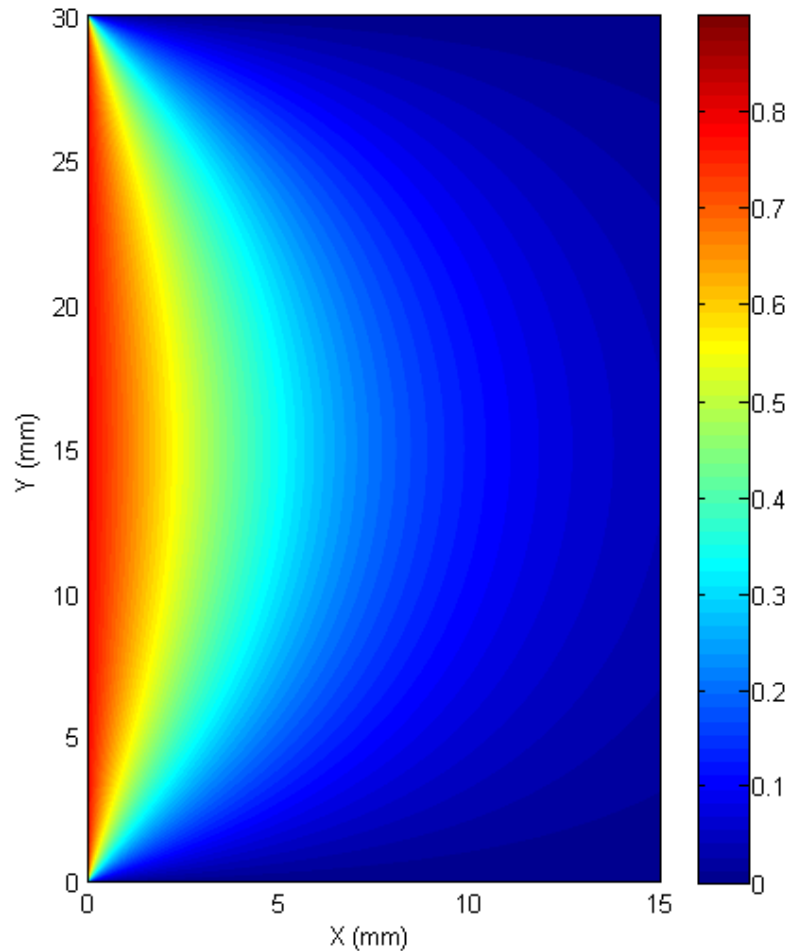


FIGURE 4.5: Contour plot showing the weighting field inside the EPS ionisation chamber. Y is the electrode face where the boundary condition is 1, for the rest of the faces the boundary condition is 0. The weighting field is required to calculate the current induced on the electrode when charges move inside the chamber.

drift of electrons, rather than that of positive charges [107, p.817]. This can be shown from examining the weighting field (pictured in figure 4.5): the gradient of this field is at a maximum around the front electrode. All electrons that reach the front electrode will traverse this region, but the positive charges created travel in the opposite direction, contributing little to the overall signal except when they are created near the front electrode.

Referring to figure 4.5, if charge is created inside the chamber, for example at $X=10$, $Y=15$, then the positive charge created travels toward $X=15$ and the negative charge travels toward $X=0$. From 4.5, the difference in weighting field that the charges move through dictates the charge induced on the electrode. At the point of origin the weighting field

measures approximately 0.2, and moves to its final point where it is 1 - a difference of 0.8. The positive charge moves from a weighting field of 0.2 to 0. Because the charges are opposite polarity and also moving in opposite directions, they both contribute to the charge induced on the front electrode.

The induced charge from the electrons and the induced charge from the electrons sum together to the value in equation 4.2. However, as the drift of electrons is much faster than that of the positive charges, the voltage induced from the electrons arises much faster. Figure 4.6 shows the charging of the front RC time constant in response to the movement of charges inside the chamber: at first RC charges quickly owing to the movement of electrons, then after V_{elec} is reached it charges more slowly until V_{max} is reached. This is where the maximum energy captured within the chamber has been captured. If the RC constant of the network were infinite, the voltage would stay at this level indefinitely. Practically RC is much bigger than t^+ for ionisation chambers in current mode [107, p.150], so V_{out} decays from this point. The case when RC is between t^- and t^+ applies to pulse-mode chambers and is discussed in section 4.4.5.

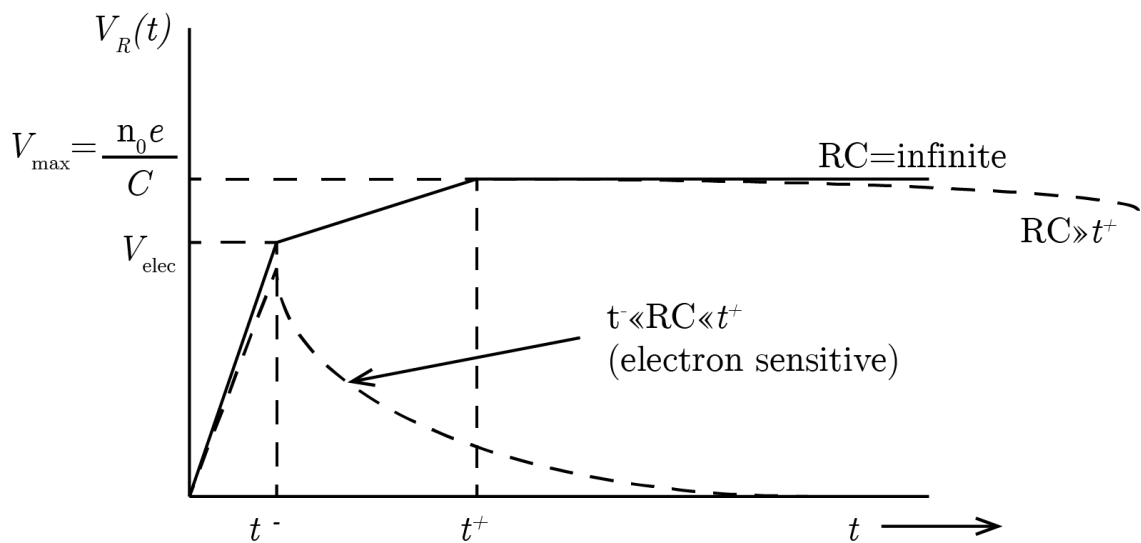


FIGURE 4.6: Charging of the front end RC network by induced charges. Shockley-Ramo theorem states that the charge induced on the front electrode depends upon the movement of charges through the difference in weighting field, thus the movement of electrons creates more charge - in a shorter time - than the movement of positive ions.

4.4.5 RC Time Constant and Pulse-Mode ionisation Chambers

In this thesis there are some tests in which the EPS ionisation chamber is used to detect the movement of charge in response to the arrival of individual particles. This is pulse-mode, as the output of the detector to an individual incident particle will be a pulse rather than the integrated output seen in integrating detectors, where the output is proportional to the rate of charge created in the chamber per second.

In order to build an effective pulse mode detector, the RC time constant of the front end must be considered: this RC time constant affects how quickly the front end can charge and discharge: In a current-mode chamber, the RC constant is long compared with the drift time of the ions and electrons whereas in a pulse-mode detector the time constant is most often operated so the RC time constant is shorter than the drift time of the positive ions, but longer than the drift time of the electrons [107, p.150]. For the EPS detector, the value of C is affected by parasitic capacitances in the electrometer and associated wiring. The R is affected by the resistor used at the front end. In the EPS sensor feedback techniques are used to artificially reduce the value of C by manipulating the voltage applied between the two plates. This effect is discussed in more detail in section 4.7.

4.4.6 More Factors Affecting the Efficiency of Ionisation Chambers

When measuring a source, there are two basic factors which affect the efficiency of any chamber - the amount of radiation entering the chamber and the likelihood that of that radiation interacting [100, p.121] - the following is from Leo's analysis of efficiency in chambers. When a isotropically radiating point source is considered, the angle which the detector occupies within this sphere dictates the proportion of the total radiation incident to the detector -

$$P(\theta)d\Omega = d\Omega/4\pi \quad (4.6)$$

Where $d\Omega$ is projected 3d angle that the detector occupies. The radiation interacting for charged particles detectors is assumed to be high - as Leo states "*it is rare for a charge particle not to produce some sort of ionisation*".

As previously mentioned, some recombination effects are always present, even when a large enough field is applied to enter the proportional region. This adds another consideration to the efficiency of current-mode ionisation chambers. Weinhaus [116] and Yamamoto et. al [117] describe different experimental techniques for establishing the efficiency of chambers. These methods are not discussed further in this thesis as the thesis serves as a proof of concept of the EPS as particle detector, which is possible without exact calibration of the detector.

4.5 Mathematical Analysis of the Saturation Region

This thesis uses Boag and Wilson's mathematical description of the behaviour of parallel plate ionisation chambers [38]. This analysis simplifies J.J. Thompsons equations [23] by ignoring the space charge terms in his mathematics. A short summary of the main points of this analysis is important for the context of later analysis of the EPS behaviour.

4.5.1 Boag and Wilson's analysis

The saturation region occurs when enough electric field is applied to the plates of an ionisation chamber that increasing the field further does not reduce the recombination. In the following discussion of Boag and Wilson's analysis [38] it is show that the application of electric field produces two effects - to alter the concentration of charge in the gas, resulting in higher concentrations of positive and negative charge near to the plates and to separate the charges more quickly, hence both types of recombination - volume and initial - are reduced. According to Boag and Wilson the average rate of recombination can be represented by the following formula -

$$R = \frac{1}{d} \int_0^d \alpha p_1(x) p_2(x) dx \quad (4.7)$$

Where d is the distance between the plates (m), α the recombination coefficient (dimensionless), p_1 the charge density of positive ions (q/m^2), p_2 the charge density of negative ions (q/m^2) and e is the electric field (v/m). This formula represents the average rate of recombination at a point x between the plates. This recombination is greatest when

the concentration of positive and negative ions is high. Without a separating voltage, the distribution of ions in the volume is assumed to be equal, i.e.

$$p_1(x) = p_2(x) \text{ for all } x$$

When a voltage is applied the concentration of the ions is altered, resulting in a higher concentration around the plates. As the voltage is increased the saturation condition is approached and the concentration of charges further approaches the ideal approximation where -

$$p_1(x) = \frac{x}{d} \frac{i}{k_1 v} \quad (4.8)$$

$$p_2(x) = \left(1 - \frac{x}{d}\right) \frac{i}{k_2 v} \quad (4.9)$$

Meaning that the product of p_1 and p_2 to which the rate of recombination is proportional to is a quadratic function of x with the maximum is somewhere between the plates. In other words when voltage is applied the ionic concentration between the plates changes, charges crowding around either plate. When an ion pair is created in the volume the charges are separated by the field reducing the effect of initial recombination, and the concentrations of ions is altered sufficiently that the chance of volume recombination is also sufficiently decreased.

The saturation characteristics of the saturation region rely on the size and shape of the ionised volume, the rate of ionisation, and the voltage applied. Boag and Wilson [38] approximate the function of f as follows

$$f = 2/[1 + \sqrt{1 + \frac{2}{3}\xi^2}] \quad (4.10)$$

$$\xi = m \frac{d^2 \sqrt{q}}{v}$$

The curve is plotted with respect to

$$\frac{d^2 \sqrt{q}}{V} \quad (4.11)$$

Where d is distance (m), q the rate of ionisation in the chamber (C), v the the voltage

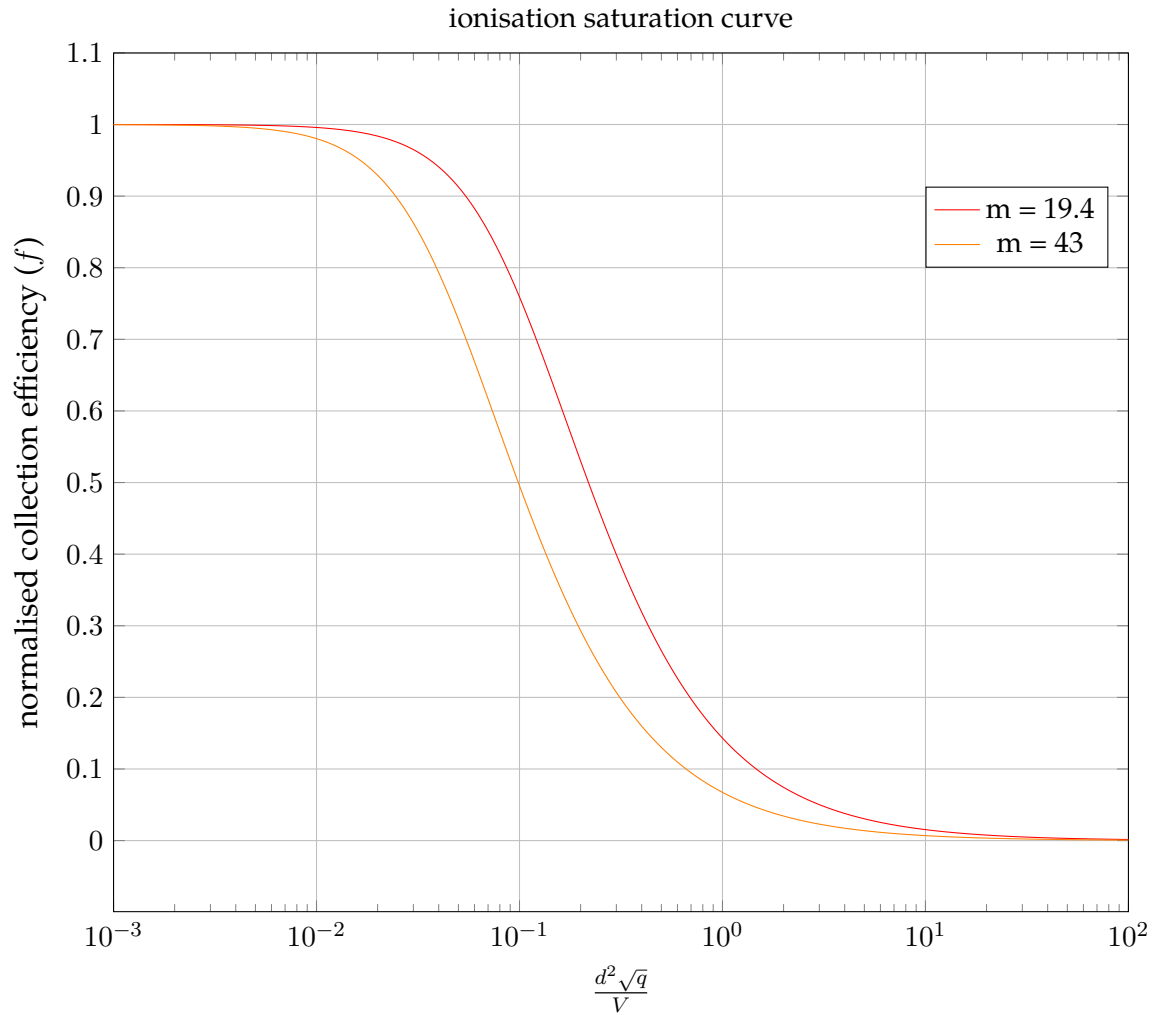


FIGURE 4.7: The ionisation saturation curve, plotted from Boag and Wilson's formula. It can be seen that as the voltage is increased $\frac{d^2 \sqrt{q}}{V}$ becomes smaller and the collection efficiency f approaches 1.

between plates (V), and m is a scaling factor accounting for the mobility of the charges, the exact value of which is discussed in section 4.5.2.

The theoretical curve of function in equation 4.10 is depicted in figure 5.5. As the base is divided by the voltage between the plates, the axis is mirrored - small values of V correspond to large values on the x axis. It can be seen that by applying a larger field between the plates (V), the rate of recombination drops and the efficiency (f) approaches 1. Two values of m are plotted, accounting for extreme values of m (see section 4.5.2).

4.5.2 The Value of m

The theoretical value of m - the mobility of the charges is equal to

$$\sqrt{\frac{\alpha}{k_1 k_2}} \quad (4.12)$$

Where α is equal to the recombination coefficient (dimensionless), k_1 ionic mobility of positive ions (m/s), k_2 ionic mobility of negative ions (m/s). These factors are controlled by the atmospheric conditions and are affected by humidity, concentration of gases present and air pressure. The Boag and Wilson paper notes a lack of concordance of various measurements and calculations of k_1 and k_2 . The value of this factor m is the focus of the 1967 paper by Greening [118], and more recently by Boutillon [119] in 1998, and Takata and Matiullah in 1990 [120] in which various measured values for m from different sources are presented. Boutillon explains the reasons for the large spread of results as follows -

"the range of the recombination losses is often large, up to 40 % in some cases, so that the theory does not strictly apply; in many cases space charge and initial recombination are ignored; the polarity effect is disregarded; and, finally, the influence of atmospheric conditions is often neglected"

for the purposes of this thesis, the minimum and maximum values available from the papers reviewed are used - the minimum value of 19.4 from Boag and Wilson's paper, and the maximum value of 43.4 recorded in the Greening paper.

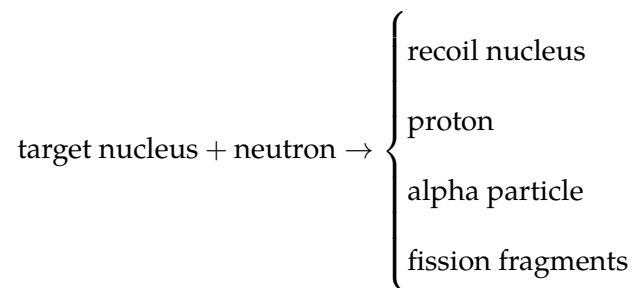
4.6 Neutron Detection

Neutrons have no charge and consequently neutron radiation does not ionise through Coulomb interaction like the charged particles discussed in previous sections. Virtually all neutron detectors are sensitive to the charged particles produced from collisions with a target nucleus [107, p.519].

4.6.1 Scattering and Absorption

As neutrons interact by strong force collisions with particles, the likelihood of their interaction with matter is much lower than that of charged particles which can interact via Coulomb interaction: strong force interactions are short range, whereas electromagnetic interactions are comparatively long range [102, p.11]. A converter material is used to convert the energy of the neutron into decay particles which are then measured. When choosing this converter material, the target nuclei must be of high isotropic abundance to maximise the likelihood of a collision with the neutron [107, p.520]. The measurement of cross section outlined in section 4.2. The two most important interactions are:

- *Scattering* the neutron collides with a nucleus, changing its kinetic energy and direction. The nucleus may be excited and emit radiation in the process of relaxation. There are two types of scattering - elastic and inelastic scattering.
- *Absorption* the neutron and the nucleus collide, the structure of the nucleus - and or the neutron - are changed causing decay products. The different types of absorption refer to the decay products produced: electromagnetic, charged, neutral and fission. Only slow moving neutrons are likely to be absorbed, with fast moving neutrons normally undergoing scattering reactions [100, p.65]. According to Knoll [107, p.520], possible decay products from neutron absorption are -



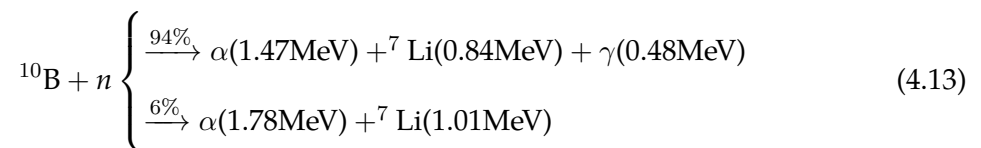
The scattering cross section (σ_s) and absorption cross section (σ_a) refer to the probability that an incident particle will be either scattered or absorbed. When added together they give the total cross section (σ_t). Cross sections are given in table 4.2. Three commonly used isotopes used in converter materials are ^6Li , ^{10}B and ^3He [107, p.521]. Compounds using these particular isotopes are most often used as they are more readily available or more easy to work with. This thesis covers experiments using carborane ($\text{C}_2\text{B}_{10}\text{H}_{12}$), lithium

element	absorption cross section for 2200 m/s neutrons (barns)
^{10}B	3835
B	767
^6Li	940
Li	70.5
Be	0.0076
^3He	5333
He	0.00747
F	0.0096
C	0.0035
Cu	3.78
H	0.3326
^2H	0.000519

TABLE 4.2: Neutron cross sections. Converter layers in detectors are chosen for their high neutron cross section, which is a measure of how likely it is that an incident neutron is absorbed and converted into decay products. [122]

flouride and niobium. When a compound is used, the term "target nucleus" refers to the nucleus with which an incident neutron might collide with to produce measurable collision products. The target nucleus of carborane is boron, and of lithium flouride, lithium. The collision products are -

Boron [46]



Lithium [121]



The combined energy of the reaction products is known as the "Q-value" [107, p.520]. As these decay particles are mostly charged particles, they can be detected with the EPS sensor, as the sensor detects the movement of charge between the plates.

4.6.2 Behaviour of Fast Neutrons in Converter Layers

Interactions between neutrons and matter change depending on how fast the neutrons are travelling. This leads to the classification of neutrons by their energy: Leo states [100, p.64]

In general, high energy neutrons are considered to be those with energies above ≈ 100 MeV or so, whereas those between a few ten's of MeV and a few hundred keV are known as fast neutrons. Between ≈ 100 keV and approx 0.1 eV where nuclear resonance reactions occur, neutrons are referred to as epithermal.

Although the previous section covers absorption products of neutron collisions, these interactions are unlikely to occur unless the neutron is travelling slowly. The experiments in this thesis concern neutrons in the range of a few MeV, considered "fast" neutrons. As the energy of neutrons increases, the cross section of materials drops, for example the cross section of ${}^6\text{Li}$ for a 0.01 eV neutron is in the region of 1000 barns, but for a fast neutron of 1 MeV the cross section is around 0.1 b. Similar decreases are seen in the neutron cross sections of both ${}^3\text{He}$ and ${}^{10}\text{B}$ [107, p.522]. Fast neutron reactions are most likely to result in inelastic scattering [100, p.65] [102, p.632]. When elastic scattering takes place most importantly *recoil protons*,

Two documented lithium reactions for ${}^6\text{Li}$ which constitutes 7.4% [123, p.21] of natural lithium are described by Glasstone and Dolan -



Which means that when a fast neutron collides with a ${}^6\text{Li}$ nucleus, a one likely resulting reaction will produce helium-4 and hydrogen-3 (tritium) nuclei, the collected energy of which is around 4.8 MeV. The source notes "other reactions can occur with lithium-6, or the more abundant isotope lithium-7" [123, p.21]. A common lithium-7 reaction is -



[124] - One likely collision between a ${}^7\text{Li}$ nucleus and a fast neutron will produce Helium-3 and Hydrogen-3 nuclei along with a slow neutron. Combined these products have an energy of 4.8 MeV. These neutron collisions therefore produce decay products which are highly likely to interact with the converter layer - the charged helium and hydrogen nuclei mostly by ionisation and the slow neutron by neutron capture. All of these reactions may create more decay products, hence the behaviour inside the converter layer is complex but will involve the creation of charged particles which may be detected by the EPS. A full discussion of this behaviour is outside the scope of this thesis, but chapter 5 will detail experiments performed to verify the effective function and detection of neutrons using converter materials.

4.6.3 Determination of Neutron Energy

Often incident neutron reactions are distinguished by their energy. This is the basis of neutron spectroscopy. By digitising the data and plotting a pulse height spectrum - a histogram with the charge collected along the x axis (this is separated into channels, which define an upper and lower region on the energy, for example 1 to 2 MeV) and the counts per channel along the y axis - peaks should develop, centred at the incident neutron energy. Supposing that the source emits neutrons of one energy, there will be two peaks. The first is centred around the baseline energy, i.e. when no neutrons arrive and the system resets to its baseline, the second develops around the incident neutron energy. Figure 4.8 shows a typical pulse height spectrum.

4.7 EPS as a particle detector

Previous research with the EPS has typically focused on the detection of electric fields [61],[62],[55] but as a particle detector the EPS detects the movement of charged particles in the electric field created by the two plates. The experiments in chapter 5 detail experiments undertaken in using the EPS as a particle detector to detect firstly charged particles, then to detect neutrons. The operation of the EPS as a particle detector is most easily understood

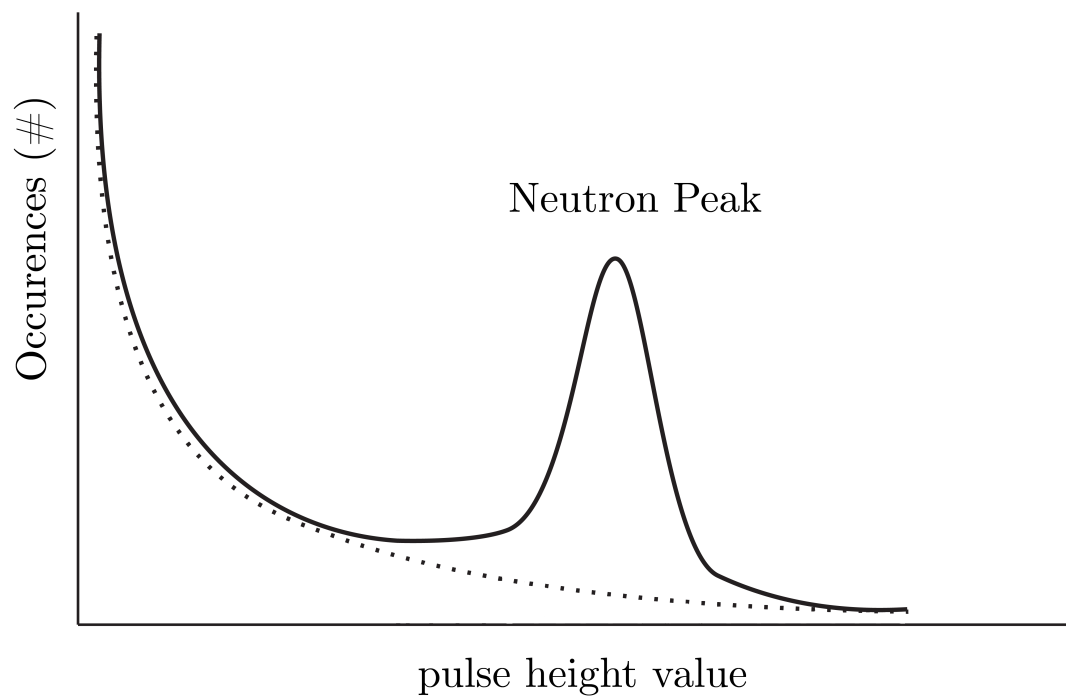


FIGURE 4.8: Pulse height spectrum: A histogram of time-domain data from a particle detector reveals useful information regarding the energy content of the incident radiation. The solid line represents a data with a sample, the dotted without the sample)

by first considering its behaviour as an ionisation chamber, before extending the principles to the detection of neutrons, as most of the modifications are the same.

For the EPS to be effective as an ionisation chamber, various modifications need to be made. Figure 4.9 shows the apparatus used as a front end for the EPS. The sensors high input impedance makes it sensitive to electric fields within the operational bandwidth, including mains interference. Surrounding the front electrode of the sensor with a shielded tube (2) and covering the outer with a conductive gauze (1) produces a shielded sensor immune to outside interference but accessible to the air. When a voltage is applied to the front gauze, the sensor can be as a traditional ionisation chamber. The front electrode (7) to which the electrons move in normal operation is paired with a back electrode (8), which is held at the same potential as the shield, and electrically joined to a piece of copper tape which covers the space between the electrodes (9) to provide complete grounding. The back electrode is necessary to shield the front, and a space is provided in order that only the minimum amount of capacitance between the electrodes is present. The electrode assembly is connected to the electrometer via a piece of semi-rigid coaxial cable (3,6) with an

SMA (4) connector on the opposite end. The electrometer is held in a shielded enclosure.

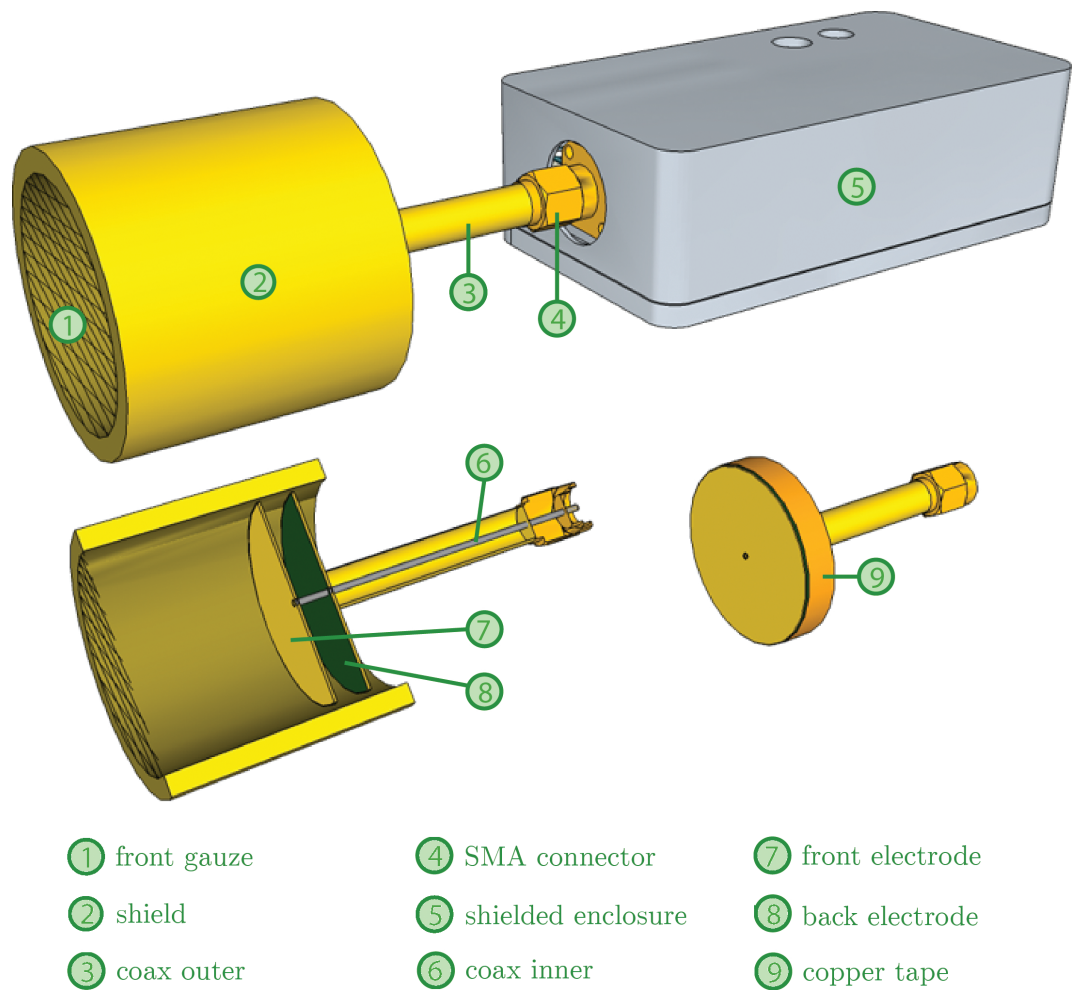


FIGURE 4.9: EPS modifications to allow particle detection. The three parts show different views of the modifications made to the EPS

Figure 4.9 shows three different views of the modifications made to the EPS. The top picture shows the electrode assembly attached to the grey box (5) which houses the electrometer. The bottom left shows a cross section of the electrode assembly.

4.7.1 EPS as an Ionisation Chamber

The EPS sensor ionisation detector behaves similarly to a conventional ionisation chambers. In this design there is no captive volume of gas and hence there is no need for a window which separates the gas from the outside air. This means lower energy particles

can enter the region between the plates as they are unimpeded by a barrier, but the effect of drift due to air currents may be higher and consequently the efficiency of the chamber may suffer.

- *Low pressure measurement.*

As there is no captive volume of gas, the air pressure is the same as the ambient pressure. The measurements covered in this thesis were taken in laboratory conditions and were therefore around 1 bar. This low pressure means the effects of recombination will be lower as the charge density is likely to be low (equation 4.7).

- *Variable capacitance*

By utilising the feedback capabilities of the EPS sensor, capacitance can be 'trimmed' off the front end. As the effective capacitance is reduced the sensor further approaches the behaviour of a pulse mode detector, described in section 4.4.4. The RC time constant can be expected to be longer than the drift time of the electrons and the positive ions, meaning that the detector is operating in current mode where the voltage out is the integral of the charge induced by movement of charge inside the chamber. When the capacitance is reduced so that the RC time constant is lower than the drift time of the positive ions the detector is operating in pulse mode, where individual ionising events may be detected. The ability to control the front end RC constant allows the operation of the sensor to be changed for different applications. The feedback is taken from the output of the electrometer and can be applied to the outer of the coax, the back electrode, the shield and the front gauze (3,8,2 and 1 in figure 4.9). By applying this signal the potential difference between these points is reduced which reduces the capacitance.

4.7.2 Calculation of Radiation Activity

If the EPS ionisation chamber is operating in the saturation region and the output is measured, the amount of radiation entering the chamber from a known source of radiation can be inferred. Working backwards from the output of the sensor, we find the saturation

current (I_s) from the output of the sensor (V) and the resistance of the front end (R):

$$I_s = V/R \quad (4.17)$$

One ampere is equal to one coulomb per second, so the number of electrons - and hence the number of ion pairs created - is calculated by dividing the current by the charge on one electron.

$$\text{ion pairs created per second (PPS)} = \frac{I_s}{1.6 \times 10^{-19}} \quad (4.18)$$

Now the energy needed to produce x amount of ion pairs can be calculated from the energy of the incident particles

$$\text{Number of charged particles per second} = \frac{PPS \times V_k}{V_i} \quad (4.19)$$

Where V_k is kinetic energy, and V_i is ionisation potential.

4.7.3 EPS in Neutron Measurements

When using the EPS, neutron detection is achieved by covering the front electrode with a thin layer of a converter material to create a detector which detects the charged decay products produced by neutron collisions. When this modification is made the grid apparatus does not function to separate the ion pairs in the region between the plates, as with the ionisation chamber, but is still necessary to shield the sensor from electromagnetic interference and apply feedback which enables the of individual ionising incidents within the converter layer by reducing the front RC time constant. The field between the plates also makes the EPS sensitive to charge created between the plates (Shockley-Ramo theorem, covered in chapter 4, section 4.4.4) even if it then recombines in the converter layer before reaching the front electrode.

Chapter 5

Experimental Results

This chapter documents the design, results and analysis of experiments conducted to characterise the behaviour of the EPS as a particle detector. Detailed in this chapter is the direct detection of alpha and beta particles, detection of ionic current produced by alpha particles in air (analogous to a traditional ionisation chamber), manipulation of rise and fall times by the use of feedback and neutron detection conducted with appropriate converter layers on the front electrode. The sensors used in these experiments are the same in their basic design principles as those used for the NMR experiments, but are modified as per the directions in chapter 4.

5.1 Detection of Ionic Current due to Ionisation of Air

The EPS was tested to confirm its operation as a particle detector. The test conducted was to show the sensor reacted to the presence of a radioactive source. Figure 5.1 shows the experiment. A 37 kBq piece of americium was attached to a laboratory jack and the distance (d) between the source and the front of the EPS altered by 2 mm every measurement and given approximately 5 seconds to settle. The grid voltage was held constant at 0 V.

5.1.1 Results

The data collected is plotted in figure 5.2. The sensor used for this experiment was non-inverting. The data plotted is the absolute value of the data recorded, which showed a consistent negative offset in the presence of the sample, which decreased with distance. This is consistent with movement of electrons to the front electrode of the sensor. The data is averaged from 10 sets of measurements, as the output drifts slightly when air currents move the air around the sensor, moving the charged particles between the anode and cathode.

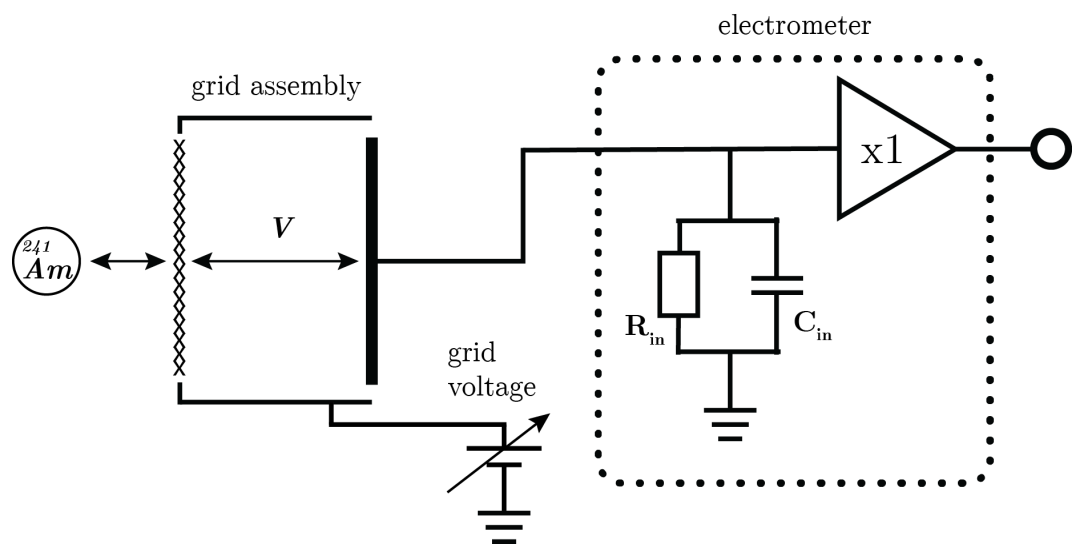


FIGURE 5.1: Experimental setup to detect ionic current with the EPS. The grid voltage between the front electrode and grid is held at a DC voltage of 0 V and the distance between the source and the grid is altered by 2mm every measurement.

5.1.2 Analysis

There are two notable aspects of the data - the graph of output against grid voltage (figure 5.2) does not appear to be linear and >200 mV of signal is present when the source is near the sensor, despite the absence of a grid voltage. Charged air around the source is created by alpha particles radiated isotropically from the source, when the source is moved further from the sensor the signal may be expected to decrease according to an inverse square-law relationship, as is usual with sources that radiate equally in all directions (the source radiates equally in all directions but the metal which holds the sample absorbs most of it).

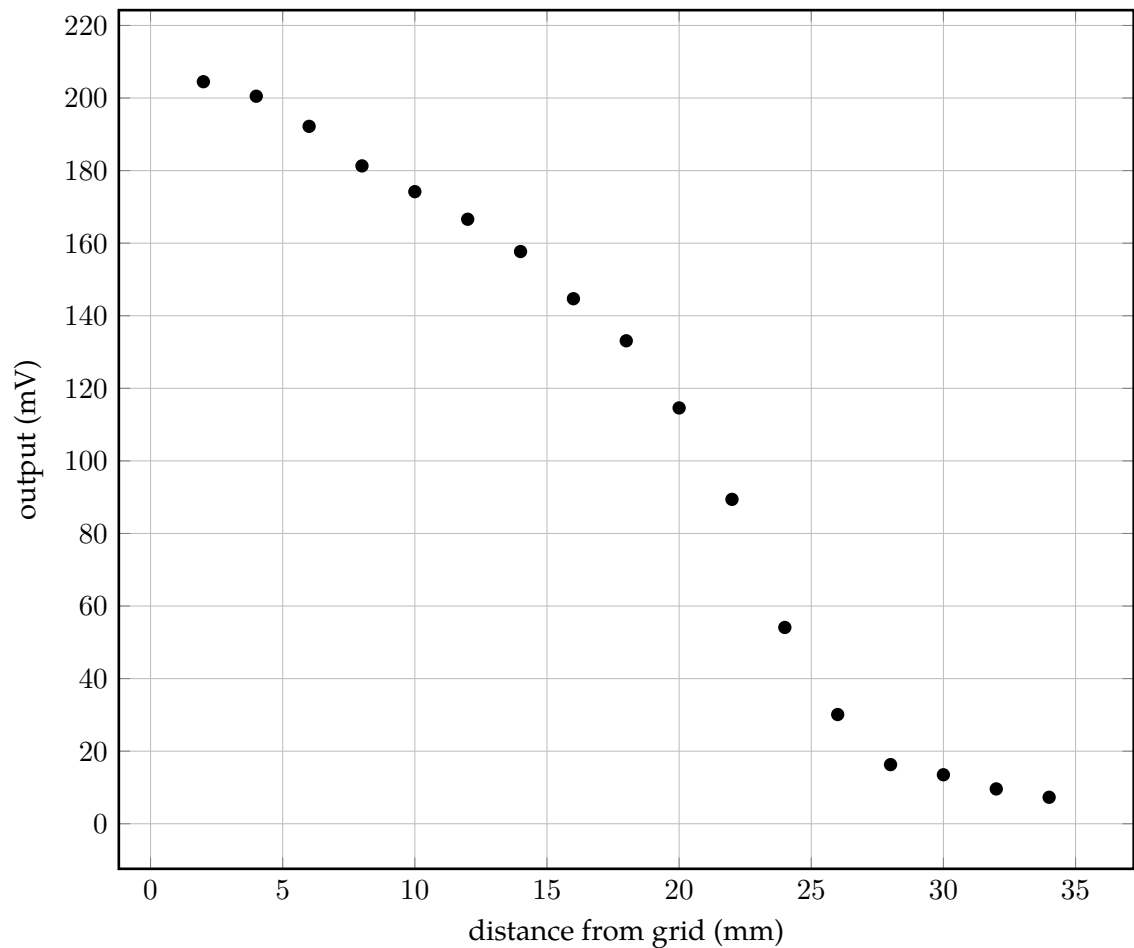


FIGURE 5.2: Output of EPS when the air between the grid and plate is irradiated by an ^{241}Am source, as a function of source-grid distance.

The unusual shape of this curve is most likely due to the complex interaction of ion pairs and alpha particles between the plates, though a thorough analysis of this behaviour is beyond the scope of this thesis.

The absence of an applied grid voltage is relevant only in the first instance when the detector is exposed to the source and both the anode and cathode are at the same potential. Any charging of the front electrode (which can vary in voltage, as it is separated from ground by a $20\text{ G}\Omega$ resistor) will result in the creation of a field between the electrode and grid which will act to separate the ion pairs. As covered in section chapter 4, 4.4.1, most of the energy from incident alpha particles is lost to non-ionising interactions and electrons freed often gain kinetic energy and travel away from their points of origin as delta electrons. These electrons carry on moving unless repelled by a voltage. It is likely collection

of these recoil electrons on the electrode which produces a signal even when there is no grid voltage applied.

The ionisation current can be calculated using Ohm's law using the value of the input resistor and the output DC output voltage. The peak output voltage (220 mV), when the distance between the source and the grid is ≈ 2 mm corresponds to a current of 9.5×10^{-12} A and 5.9×10^7 electrons. As the amount of alpha particles emitted by the source is much lower, this result would seem to confirm that each alpha particle produces many ion pairs (covered in 4, section 4.4.1) - the amount of ion pairs produced by a 5 MeV alpha particle which fully ionises in air is $\approx 16.67 \times 10^4$, if the W value is taken to be 30 eV.

5.2 Effect of Altering Grid Voltage

Tests were conducted to show that applying a grid voltage separates the ion pairs created by a source of charged particles. Like conventional ion chambers, the EPS sensor allows adjustment of the electric field over the ionised region in order to minimise recombination effects. Altering the grid voltage alters the distribution of the positive and negative charges inside the chamber, resulting in less recombination between the charges (section 4, 4.5). The experimental setup is the same as figure 5.1 but for this experiment the distance between the sample and the grid (d) is kept constant at approximately 4 mm. No feedback is used and the sample is held in open air.

5.2.1 Measurements

Figure 5.3 shows the output from the sensor when the grid voltage is varied between ± 2 V on the top plot and ± 6 V on the bottom plot. An approximately linear relationship can be clearly seen between the grid and output voltages between ± 2 V. When the grid voltage is increased beyond this region a plateau starts to emerge. When the grid voltage is increased past 5 V there is a consistent plateau as far as ± 1000 V grid voltage, which is visible in figure 5.4. At 0 V grid voltage there is a small offset of approximately 100 mV, this is most likely due to the offset voltage at the front of the op amp, which creates a small potential between the electrode and the grid.

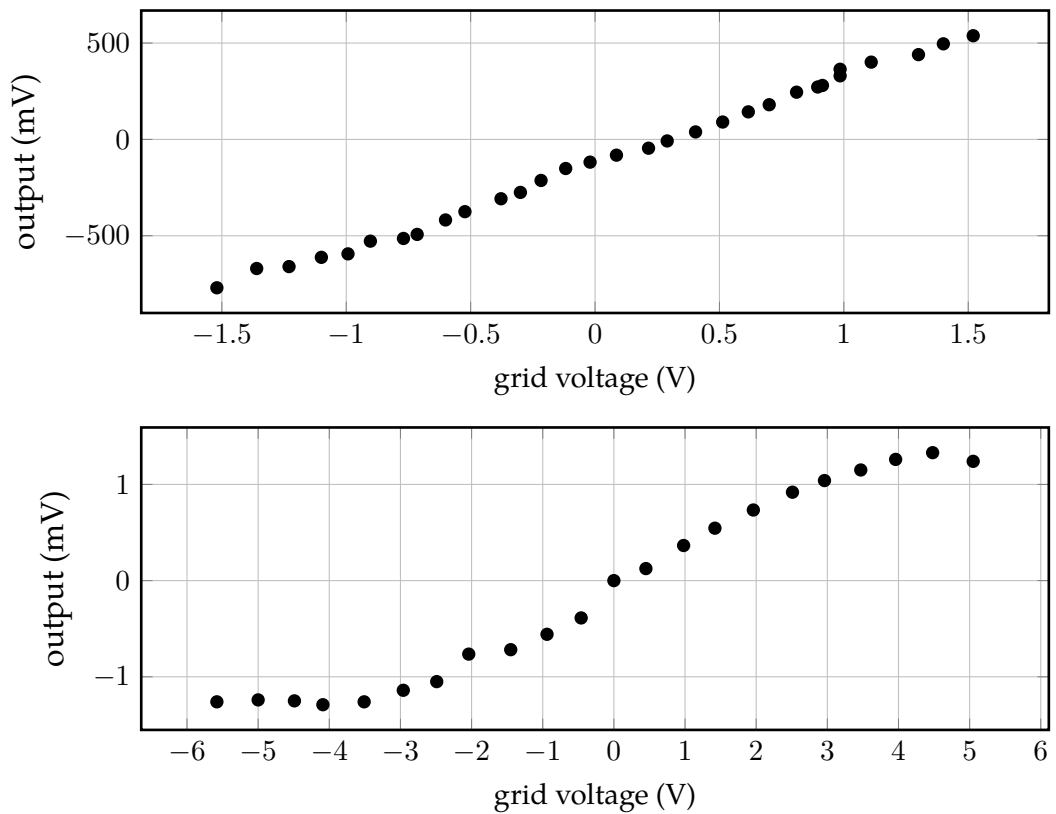


FIGURE 5.3: Output of EPS as a function of grid voltage when irradiated with a ^{241}Am source kept at a fixed distance in front of the sensor. Top plot shows a relatively linear relationship between ± 1.5 V and between ± 6 V the start of the saturation region (see section 4, 4.3) can be seen between approximately ± 3 -6 V.

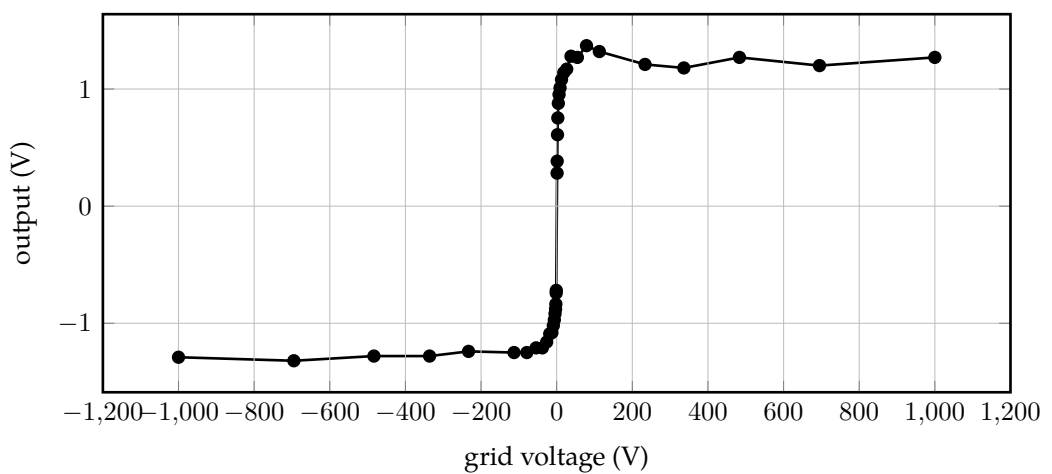


FIGURE 5.4: Output of EPS as a function of grid voltage. Lines between the points are guides for the eyes only.

The test results show a clear linear relationship between output voltage and grid voltage between ± 2 V, and a plateau of $\approx \pm 1.26$ V. The results show the saturation and recombination regions described in chapter 4, section 4.3. When enough voltage is applied, recombination effects between the plates are minimised and the application of a higher voltage between the plates will not yield a larger output voltage.

5.2.2 Discussion

The irradiation of the chamber can be calculated from the plateau voltage. Firstly the amount of particles expected to reach the electrode is calculated from the solid angle. The distance the source to the grid is 4 mm, so by trigonometry the angle subtended by the electrode from the source is 150° .

$$\begin{aligned} \text{solid angle of electrode seen from source} &= \\ \Omega &= 2\pi(1 - \cos(\frac{\theta}{2})) = 2\pi(1 - \cos(75.07)) = 4.67 \text{ sr} \end{aligned} \quad (5.1)$$

$$\text{proportion of sphere occupied by electrode} = \frac{4.67}{4\pi} = 37\% \quad (5.2)$$

Now the steady state ionisation current can be calculated using the voltage recorded in the saturation region.

$$\begin{aligned} \text{maximum number of ion pairs created per second} &= \\ \frac{n \times E}{W} \end{aligned} \quad (5.3)$$

Where n is the number of incident alpha particles, to be calculated from the source activity and the proportion of particles hitting the electrode, E is the energy of the alpha particles (5 MeV) and W is the effective ionisation potential of air (discussed in section chapter 4, 4.4.1). The calculation is continued below:

$$\frac{n \times E}{W} = \frac{37 \times 10^3 \times 0.37 \times 5 \times 10^6}{30} = 2.28 \times 10^9 \quad (5.4)$$

The steady state ionisation current is then calculated:

$$\begin{aligned} \text{current} &= \text{number of electrons} \times \text{charge on an electron} = \\ &(2.28 \times 10^9) \times (1.602 \times 10^{-19}) = 0.37 \text{ nA} \end{aligned} \quad (5.5)$$

Which would produce a voltage of 7.3 V over the front resistance. Although this figure is in good agreement with the measured value, there are factors to consider which affect the accuracy of the calculation:

- Although the activity of the source is rated at 37 kBq, the exact amount of radiation emitted from the source into the sensor is not known. The tolerance of the activity is undefined and although the shape of the americium within the brace which holds it is assumed to be a sphere for the purpose of calculations, the exact shape is not known.
- According to Bushberg et al. [112], "approximately 70 % of charged particle energy energy deposition leads to non-ionizing excitation" - consideration of which significantly reduces the expected number of ion pairs.
- Even in the saturation region, there are still some recombination effects that vitiate charge collection.
- Some radiated particles ionise in the air around the sensor and do not reach the space between the two plates.

Figure 5.4 shows a larger plot in which the saturation region extends up to 1000 V .

5.2.3 Comparison of Data to Theory

The experiment in section 5.2 was conducted again with a finer resolution (30 V in 0.01 V increments), to compare with Boag and Wilson's theoretical curve (discussed in chapter 4, section 4.5). Figure 5.5 shows a comparison of the resulting data along with the theoretical curve. The data lies between the two extremes of m discussed in chapter 4 section 4.5.2, showing that the sensor behaves in line with traditional ionisation detectors.

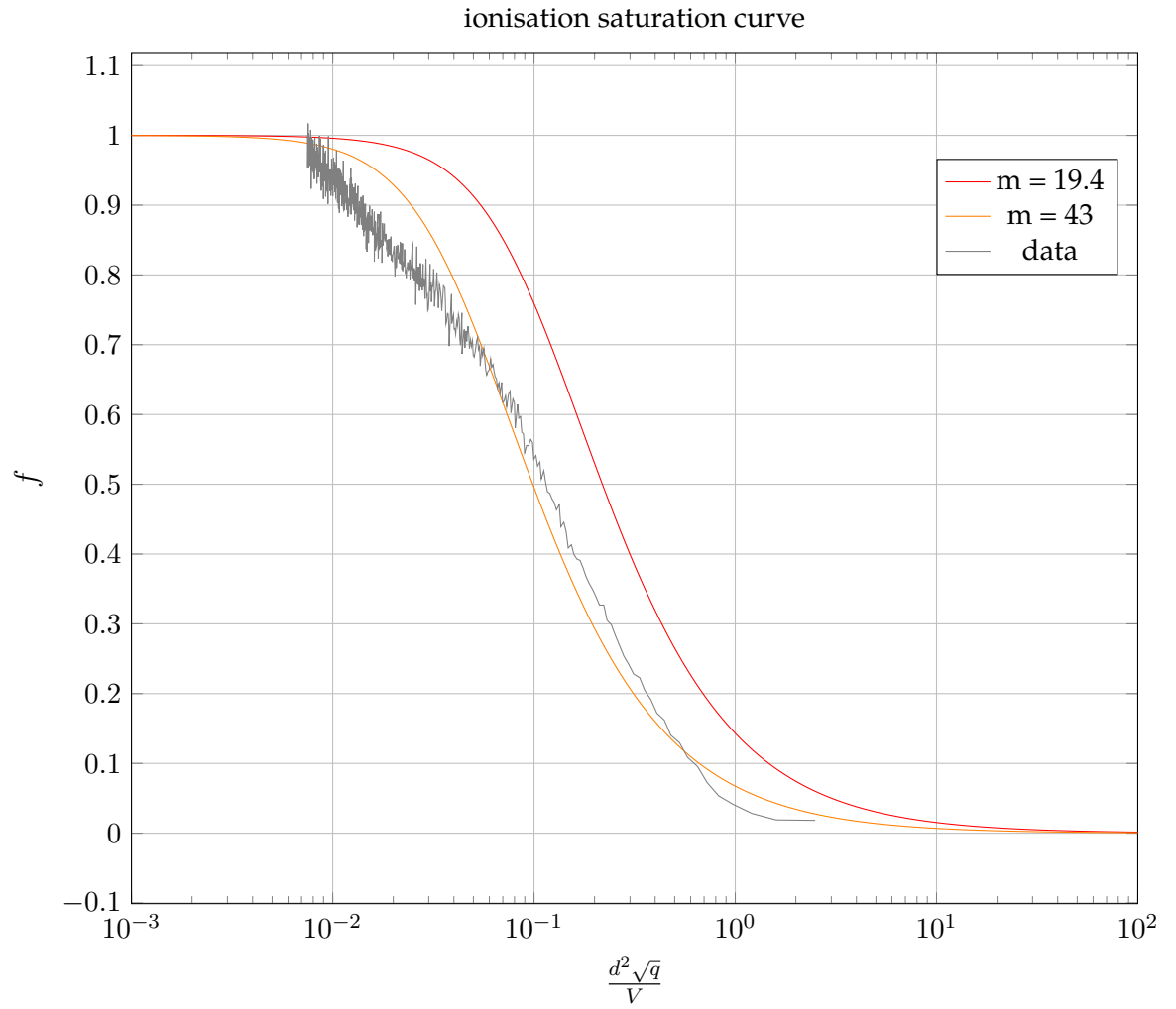


FIGURE 5.5: Measured data compared with Boag and Wilson's equation for ionisation in parallel-plate ionisation chambers. Two curves are plotted representing the upper and lower extremes of the value of m .

5.3 Rise and Fall Times

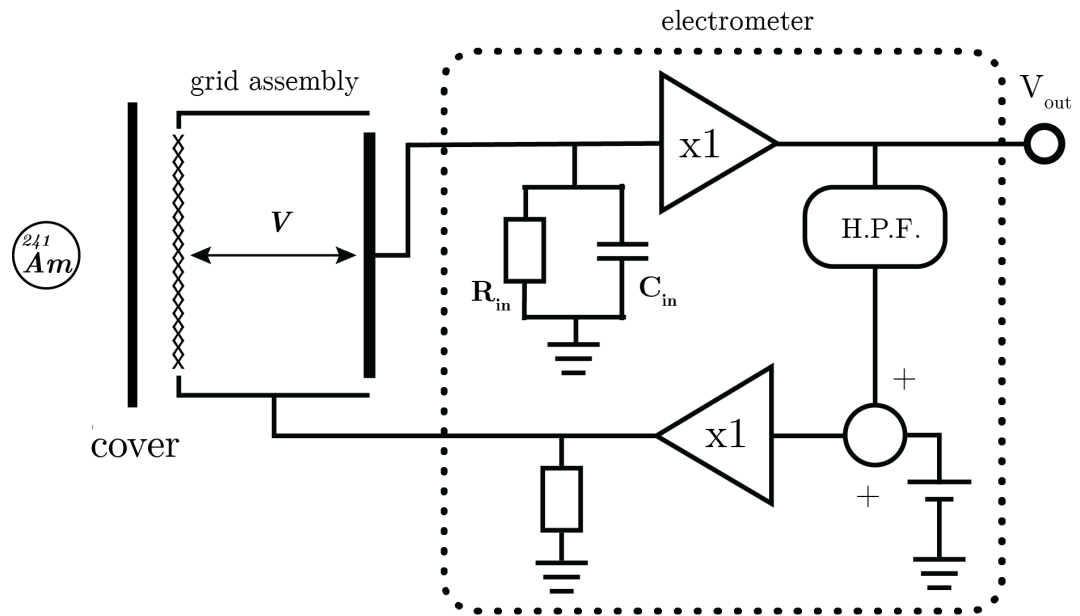


FIGURE 5.6: block diagram of an experiment to determine the effect of AC feedback on the rise and fall times of the EPS. The electrode is covered by a piece of paper, then uncovered. The process is repeated with different levels of AC feedback applied and the time domain data is captured and compared

Tests were conducted for the effect of providing AC feedback. AC feedback is usually used in the EPS to neutralise the effect of input capacitance, this effect is documented in previous research on the EPS [60]. In this test a modification to the EPS was used to high-pass filter the feedback to isolate the transients from the DC equilibrium value, the transients were then fed back to the outer guard, the rear electrode and also to the grid assembly. This is relevant since the total capacitance of the system depends on both the plates and the parasitic capacitance of the front end [107, p.141]).

5.3.1 Testing

In order to test the rise and fall times as determined by the RC constants, a simple test was devised: the sensor was covered to prevent any alpha radiation from a $37\text{ kBq }^{241}\text{Am}$ source from reaching the sensor, then uncovered. The difference in the rise and fall times (the time it takes for both to change between 10 and 90 % of the final value - 2τ) are

recorded. The experimental setup is depicted in the figure 5.6. The high pass filter had a corner frequency of 0.1 Hz, the output is summed with a variable DC voltage and applied to the grid from the output of a second op-amp. A small resistance to ground is used to reduce the RC constant of the grid. Without this resistance there is no path to ground and hence any charge that accumulates on the grid will take a long time to discharge and may distort the transient signal feedback.

5.3.2 Results

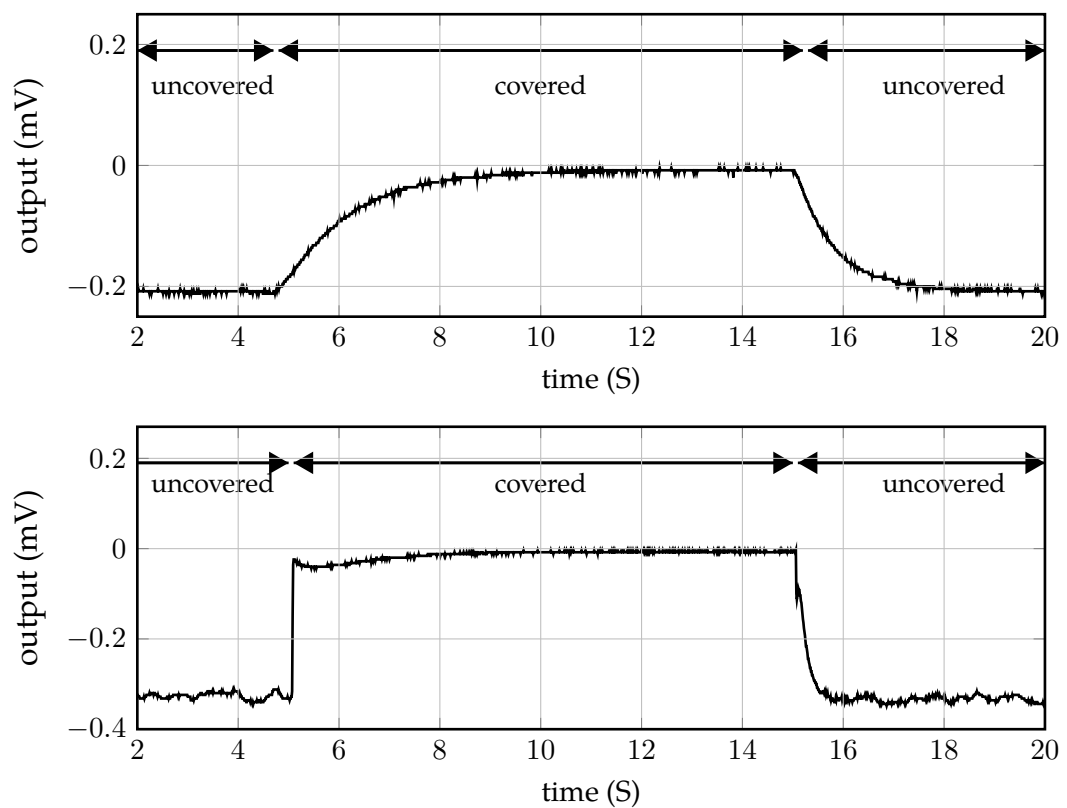


FIGURE 5.7: The effect of increasing positive AC feedback to affect rise time of the EPS in response to an Americium source. Top figure shows the rise / fall of the EPS with no feedback, and the bottom shows the effect of increasing the feedback to full. Indicators show where the source is covered and uncovered

Figure 5.7 show the results. The difference in the figures shows clearly that the rise and fall times have been reduced by a factor of approximately ten. The exact RC constant of the sensor cannot be calculated from the data because the rise time is not absolute but depends on the drift of electrons in the chamber. The use of feedback is useful for manipulating the

rise-times of the sensor, but the application of the feedback to the grid is a special case as the voltage between the plates is altered. More work is required to understand the effects of this feedback.

5.4 Direct Detection of Beta Particles

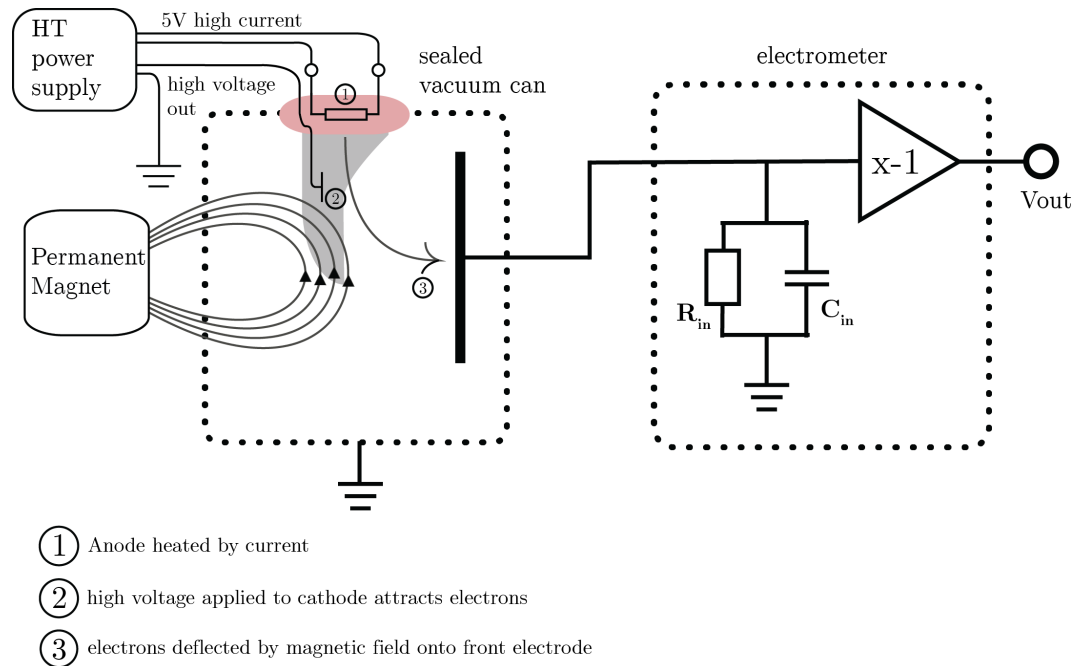


FIGURE 5.8: Diagram of experimental setup for the direct detection of beta particles. An EM80 thermionic valve is kept in a vacuum sealed box with the glass case removed. A magnet is used to divert electrons from the valve onto the front electrode

The previous tests were designed to establish if the EPS could detect alpha particles or the ionic current that alpha particles create in air. This section focuses on the direct detection of beta particles. This further proves that the previous tests detecting ionic current are a result of the movement of electrons that the alpha particles liberate. If the sensor detects beta particles (in the form of electrons) directly, a negative voltage from the build up of any charge on the front end can be expected.

A convenient source of beta particles is the EM80 thermionic valve [125]. The valve was designed to replace magnetic VU meters and focuses a beam of electrons onto a phosphor dish shaped anode which produces a photoluminescent effect in response. The beam can be focused by applying a larger voltage to the grid, creating an electric field which

deflects the electron beam. The apparatus is vacuum sealed inside a small glass shell. The cathode of the EM80 is heated by a current. The thermal energy this provides is enough - in a vacuum - to free electrons from the wire. The electrons "boil" off and are attracted to the anode by the electric field applied between the anode and cathode. The valve is rated as producing 3 mA of current at maximum - only a small proportion of which need be diverted onto the front end of the sensor to produce a response.

An experimental setup was constructed to test the direct detection of beta particles. The front electrode of the electrometer was fitted inside a die-cast aluminium box. The box was fitted to a vacuum pump and a hole cut in the top just wide enough for the valve to fit through. The valve was fitted with a collar around its base and the glass enclosure cut approximately halfway down and placed immediately onto the hole in the box. The result is a sealed box containing the EM80 valve and also the front electrode of the electrometer. A magnet was used to deflect the stream of electrons onto the front electrode. This arrangement was short-lived as opening the glass enclosure of the valve severely shortened its life and unexpectedly the front end of the sensor was eventually blown by the accumulation of charge on the front end. The apparatus did however remain intact for long enough to capture several sets of data.

5.4.1 Results

The output of the EPS showed a negative voltage from the accumulation of beta particles onto the front electrode. In order to optimise the system it was necessary to adjust the anode voltage and the magnet position. Small variations in the anode voltage around 500 V were enough to precipitate the movement of a large number of electrons, thus railing the sensor. The clearest sample of data captured is pictured in figure 5.9. Here the anode voltage is increased enough to rail the sensor then lowered slightly so that the charge is draining from the front end, approaching some equilibrium around -0.7 V. The magnet was used to move the beam inside the box, causing fluctuations in the familiar exponential decay curve. The data in fig 5.9 can be interpreted as this exponential decay shape summed with the fluctuations in current from the movement of beam.

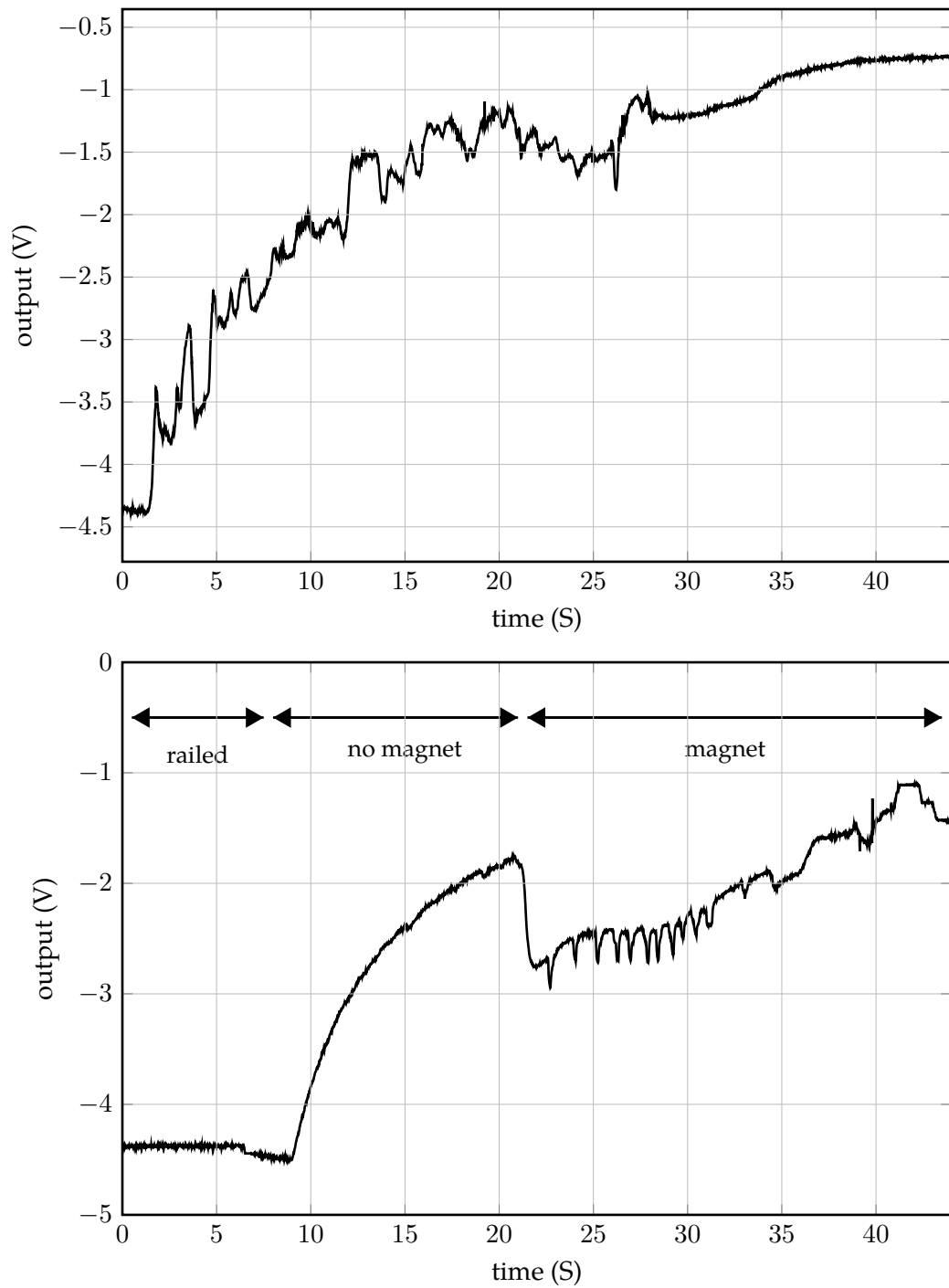


FIGURE 5.9: data captured from an EPS in response to excitation by beta particles. Top figure shows the recovery of the sensor from railed to ground whilst moving the beam with the magnet. The bottom figure shows the sensor railed, then recovering without the interference of the magnet, then with the interference from the magnet.

5.4.2 Analysis

The direct detection of beta particles by the EPS is proved beyond reasonable doubt. This provides further evidence that the results of the previous experiments are a result of the detection of beta particles in the form of free electrons from ionised air molecules, rather than from any interaction of the alpha particles with the sensor.

5.5 Direct Detection of Alpha Particles

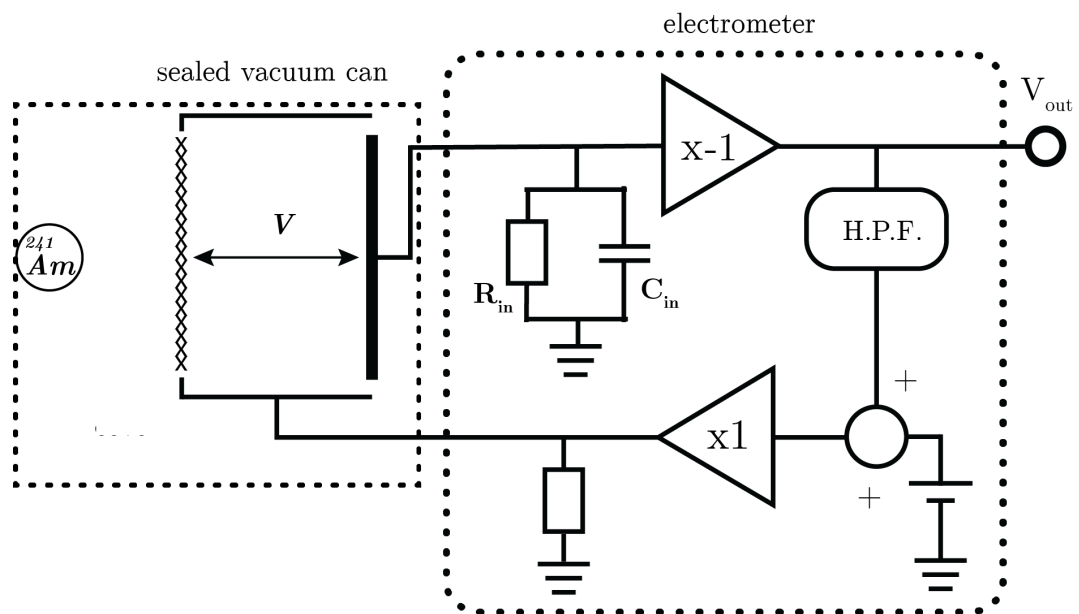


FIGURE 5.10: A schematic of the experimental setup designed to verify direct detection of alpha particles with the EPS. The grid is held in a vacuum can along with an ^{241}Am source placed ≈ 1 mm from the grid. The voltage on the grid is kept at 0 V DC, but full AC feedback is applied.

An experiment was designed to directly detect alpha particles emitted from a ^{241}Am source. Detection of these particles is possible as they have a charge of $2e$. It is known from Shockley-Ramo theorem (section chapter 4, 4.4.4) that the movement of charge through the sensor induces a current on the front electrode. Positive feedback is applied to the outer coax to reduce the time constant sufficiently so that pulses from the alpha particles movement through the air may be detected.

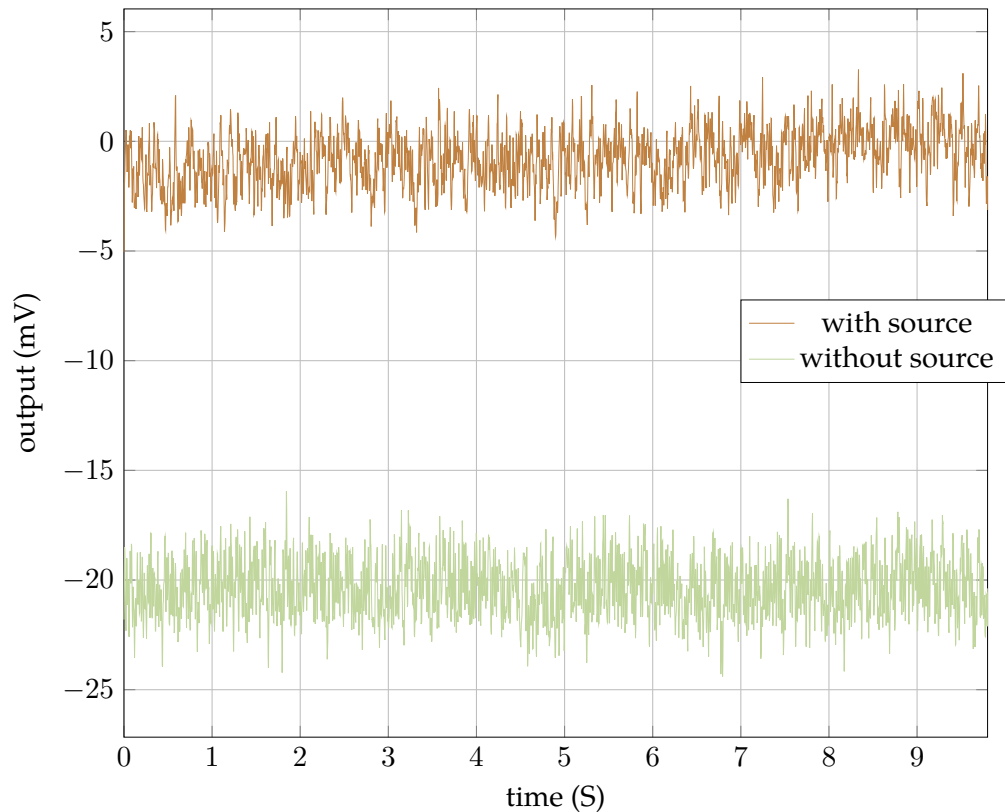


FIGURE 5.11: Data captured in experiment to detect alpha particles directed directly onto the front electrode of an EPS sensor. Two plots shows a comparison of the data with and without the source present - a positive DC offset is noticed.

The experimental setup is pictured in figure 5.10. A 37 kBq, ^{241}Am source was used to irradiate the sensor. The source was placed in a vacuum to prevent the alpha particles ionising the air and the front electrode is placed in a grounded metal vacuum can. All experiments were performed twice, first with the grid voltage at 0 V, secondly at 6 V. A through-connector is used to connect the electrometer to the outside. The pressure inside the can was reduced to 0.04 bar and the output of the EPS is recorded via a digital oscilloscope. The Americium projects alpha particles directly on to the front electrode and the AC feedback is set to its maximum stable level, reducing the parasitic capacitance of the front end and lowering the front end RC time constant. The output from the sensor was recorded both with and without a sample in the vacuum can.

The parameters of the experiment are as follows -

- grid voltage = 0 V
- distance from source to grid 1 mm

- distance from grid to electrode = 10 mm

5.5.1 Results

Figure 5.11 shows a visual comparison of two of the data sets - the sensor used has an inverting output, therefore the charge seen on the front electrode is positive. Individual spikes indicative of discrete particles arriving are not visible. However, the data show a steady and consistent negative DC offset in response to a source -

- without sample -26.623 mV
- with sample -47.58 mV

Despite the use of maximum stable neutralisation the sensor did not respond fast enough to distinguish individual particles. However, a consistent positive offset was recorded in the presence of an americium source. This positive offset varied in size between tests, but was present consistently when the source was placed inside the can.

5.5.2 Discussion

There are two points which will be discussed - the absence of pulses from the movement of alpha particles and the presence of a DC offset.

The detector would not be expected to detect pulses for the following reason: in the time it takes for the front end RC constant to charge, many alpha particles arrive on the plate this means the sensor will not function as a pulse detector but will detect the integrated charge. From Shockley Ramo theorem, a charge moving through the sensor will induce a voltage on the front end, this will start when the charge enters the field between the two plates and reach a maximum when the charge reaches the front electrode. The speed of an alpha particle can be calculated by re-arranging the formula for kinetic energy

$$\sqrt{\frac{K.E.}{0.5 \times m}} = v \quad (5.6)$$

Where K.E. is the kinetic energy (found by converting the energy of the alpha particle - 5 MeV into Joules - 8×10^{-13} J), m is the mass of the alpha particle (6.8×10^{-27} g) and v is the velocity.

$$\sqrt{\frac{8 \times 10^{-13}}{0.5 \times 6.7 \times 10^{-27}}} = 15.45 \times 10^6 \text{ m s}^{-1} \quad (5.7)$$

This means that the alpha particle will traverse the 1 cm space between the anode and cathode in 0.647 ns. The front end of the sensor therefore cannot charge quickly enough to respond to the pulses produced by alpha radiation. The 37 kBq rate of irradiation is high enough that the sensor would not recover in time to detect individual particles: If the sensor had an effective 0.7 pF of capacitance (this figure is taken from the datasheet for the OP657 [59], the minimum the sensor could have), this would mean the RC (τ) constant with a 1 G Ω resistor would be 0.7 s and the 90% rise time would be 2.2τ , 1.54 s, and if the rise time is increased 10 times (the figure calculated in section 5.3) 0.154 s, which is still many times longer than the time it takes for the alpha particles to traverse the space between the plates.

The likelihood of receiving a particle can be calculated from the solid angle. In this calculation the source is assumed to be a point source radiating isotropically into 4π . The solid angle subtended by the electrode can be found as follows:

$$\Omega = 2\pi(1 - \cos(\theta)) \quad (5.8)$$

$$\Omega = 2\pi(1 - \cos(56)) = 0.92 \text{ sr}$$

The number of alpha particles likely to be radiated onto the electrode in 1 s is found by multiplying the number of particles radiated from the source per second by the proportion of surface area that the electrode occupies.

$$\text{proportion of area occupied by electrode} \quad (5.9)$$

$$= \frac{\Omega}{4\pi} = \frac{2.79}{4\pi} = 0.22$$

$$\text{number of particles radiated onto electrode per second}$$

$$= 37000 \times 0.22 = 8140$$

Using the figure from equation 5.9, 125353 alpha particles can be expected to arrive in the time it takes the detector to charge (using the previous calculation for front end RC). The detector would therefore be operating in current mode and any charge would appear as a DC offset.

As the output signal is a DC voltage, the front end capacitor is charged and the voltage at the front end must equal the current over the resistor. The stream of alpha particles would constitute only a small current -

$$\begin{aligned} I &= \text{alpha particles emitted onto the electrode per second} \times 2e & (5.10) \\ &= 8140 \times 2 \times 1.6 \times 10^{-19} = 2.61 \times 10^{-15} \text{ A} \end{aligned}$$

Which over the front end $20 \text{ G}\Omega$ resistance would produce a $52 \mu\text{V}$ DC value. As this recorded value is many times greater than this, another possible explanation is sought.

It is possible the offset is a result of the ionisation of the front electrode, the energetic alpha particles producing recoil delta electrons (covered in section chapter 4, 4.4.1) with enough energy to travel away from the copper electrode, leaving a positive net charge. According to Perry and Zarris [110], for an ionising particle "*a substantial amount of the particles energy is not deposited locally but carried away from the track of the particle by energetic secondary electrons called δ rays*".

The range in copper of a 5 MeV alpha particle is $9.10 \times 10^{-3} \text{ g/cm}^2$ [126] and the thickness of the copper used is 1.86 g/cm^2 (the thickness of the copper is rated as 2oz. per square foot - this is converted to g/cm^2 units for direct comparison), hence the alpha particles will expend all their energy in just a fraction of the copper. The range of electrons in copper is much greater - an electron with just 125 keV kinetic energy has an almost equivalent range of $9.73 \times 10^{-3} \text{ g/cm}^2$ [127], therefore it is possible that energetic delta electrons might escape the copper leaving a net positive charge, as electrons with this energy or above are energetic enough to traverse the entire range of the 5 MeV alpha particles in copper. The creation of large numbers of such energetic electrons seems unlikely, but if significant numbers of delta electrons are created further from the end of the range, the amount of energy needed to move free of the copper is much lower.

The results here show a consistent change in DC voltage when in the presence of an alpha source. Further work is needed to verify the source of this effect. It is suggested that the same test is conducted with two different sources of different activity: if the conjecture is correct a larger offset would be present for a higher activity source. A different way of testing this same hypothesis would be to replace the copper electrode with a metal with a different ionisation potential. If the DC offset changes in response to the presence of this different metal (higher ionisation potential would result in lower DC offset and vice-versa) then this hypothesis is proven.

5.6 Neutron Detection

The EPS was used to detect neutrons by coating the electrode with a converter material. An americium-beryllium source was used to irradiate the front electrode of the EPS upon which different converter layers were tested. The grid was held at 5V and full AC feedback was used to decrease the rise time of the sensor. The neutron source is highly radioactive - 18 GBq. Tests were conducted at a private facility.

Figure 5.12 shows the setup of the experiment. A remotely operated mechanical arm moves the EPS over the Neutron source, which is held inside a tank and filled with water to act as a moderator. A hollow plastic tube is moved over the source, creating an unobstructed path for neutrons (the bottom section of the tube having a low neutron cross section hence providing little obstruction to the neutrons) through the air column in the tube. Various different converter layers were tested - Lithium Flouride, Boron Carbide, Niobium and bare copper. It is expected that there will be visible spikes on the output of the electrometer when a material with a high neutron cross section is irradiated, indicating the sudden arrival of charge on the electrode.

TABLE 5.1: Converter layer properties

Material	Thickness	Cross section of target nucleus (barns)
copper	69.58 μm	3.78
niobium	$\approx 2\text{mm}$	1.15
lithium flouride	0-1 mm	940
boron carbide	$\approx 0.1\text{ mm}$	3835

The converter layers were deposited on the electrode as follows -

- *Copper* a bare copper electrode was used, made from commercially available 2 oz. copper-clad board.
- *Lithium Flouride* was painted on solute and allowed to dry. The resulting coating is an uneven grainy white coating varying from approximately 0 to 1mm thick.
- *Niobium* was glued directly to the copper electrode using silver epoxy. The layer is approximately 2mm thick.
- *Boron Carbide* is deposited on to copper foil via a sputtering process, the resulting layer is in the region of ≈ 0.1 mm thick. The foil was glued to the electrode using a commercially available glue.

filters used on the signals are as follows -

- lowpass @ 30 Hz 1st order (post processing)
- x10 gain
- 50 Hz notch (mains hum filter)
- DC coupled

5.6.1 Results

Lithium flouride and Boron carbide converter layers produced visible spikes on the output of the electrometer. These are consistent with the arrival of neutrons, producing a sudden increase in charge. In comparison, few spikes are seen when using a Copper or Niobium converter layer - materials with comparatively low neutron cross section. Figures 5.13 and 5.14 show approximately two minutes of data with each different type of converter layer. Spikes are clearly distinguished in figure 5.13 for the Lithium flouride and Boron carbide converter layers but for Copper and Niobium the spikes are so infrequent as to be almost completely insignificant. The data for Niobium and Boron have been processed to remove an exponential decay in the DC level, due to the front end of the sensor settling.

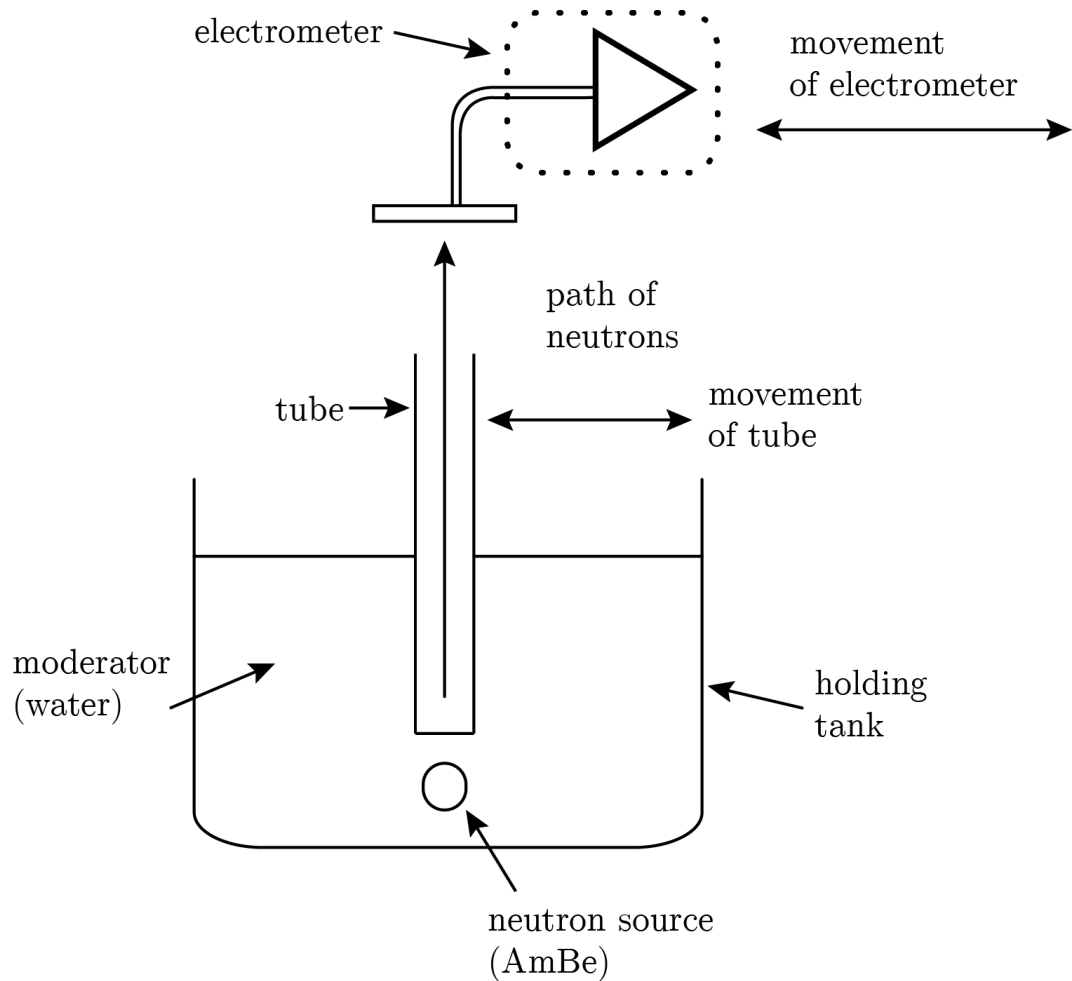


FIGURE 5.12: Diagram of experimental setup for the direct detection of neutrons. An Americium-Beryllium source is held in a tank with water to act as a moderator. When both are moved above the source, a path from the source to the electrometer exists.

5.6.2 Analysis

Figure 5.15 shows histograms of two sets of data, both *approx* 120 s - the top plot shows a Lithium fluoride converter with the EPS on a shelf in the same room as the neutron source. The second shows the same sensor over the neutron source. These histograms represent a spectrum of pulse heights. When the sensor is on the shelf few neutrons reach the electrode and the background level is recorded - the histogram shows a spike at approximately 0.17 V. With the sensor over the source the baseline moves to approximately 0.19 V. There are a series of small peaks to the right of the main peak indicating the neutron capture events are producing energies around particular values - there is a clear peak at ≈ 0.207 , a smaller, broader peak around 0.22 and a smaller peak still at ≈ 0.236 . The pulse

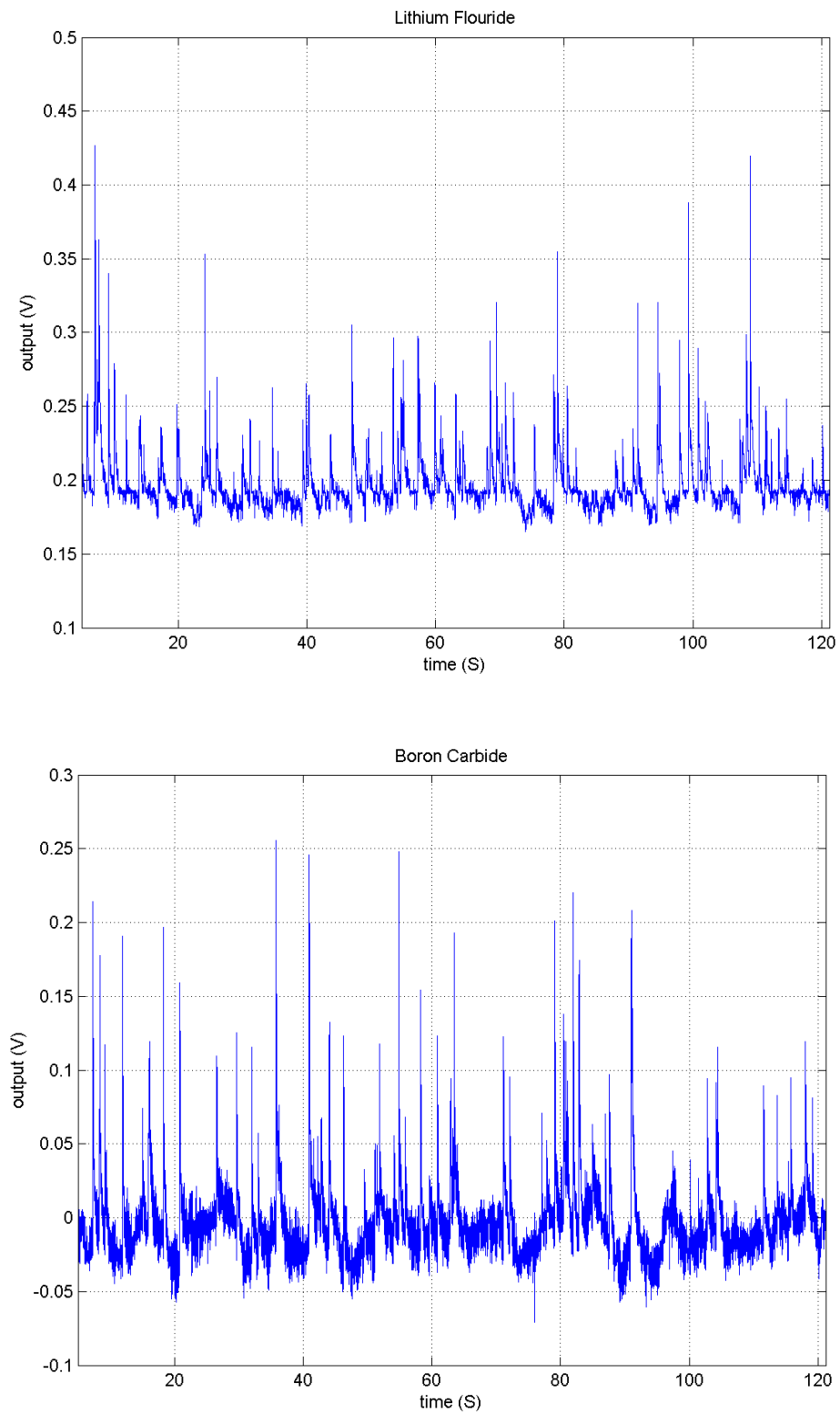


FIGURE 5.13: Top figure shows data captured from the EPS sensor with a Lithium Fluoride converter layer when irradiated by an Americium Beryllium neutron source. The lower figure shows data from the same sensor with a Boron Carbide coated electrode irradiated from the same source.

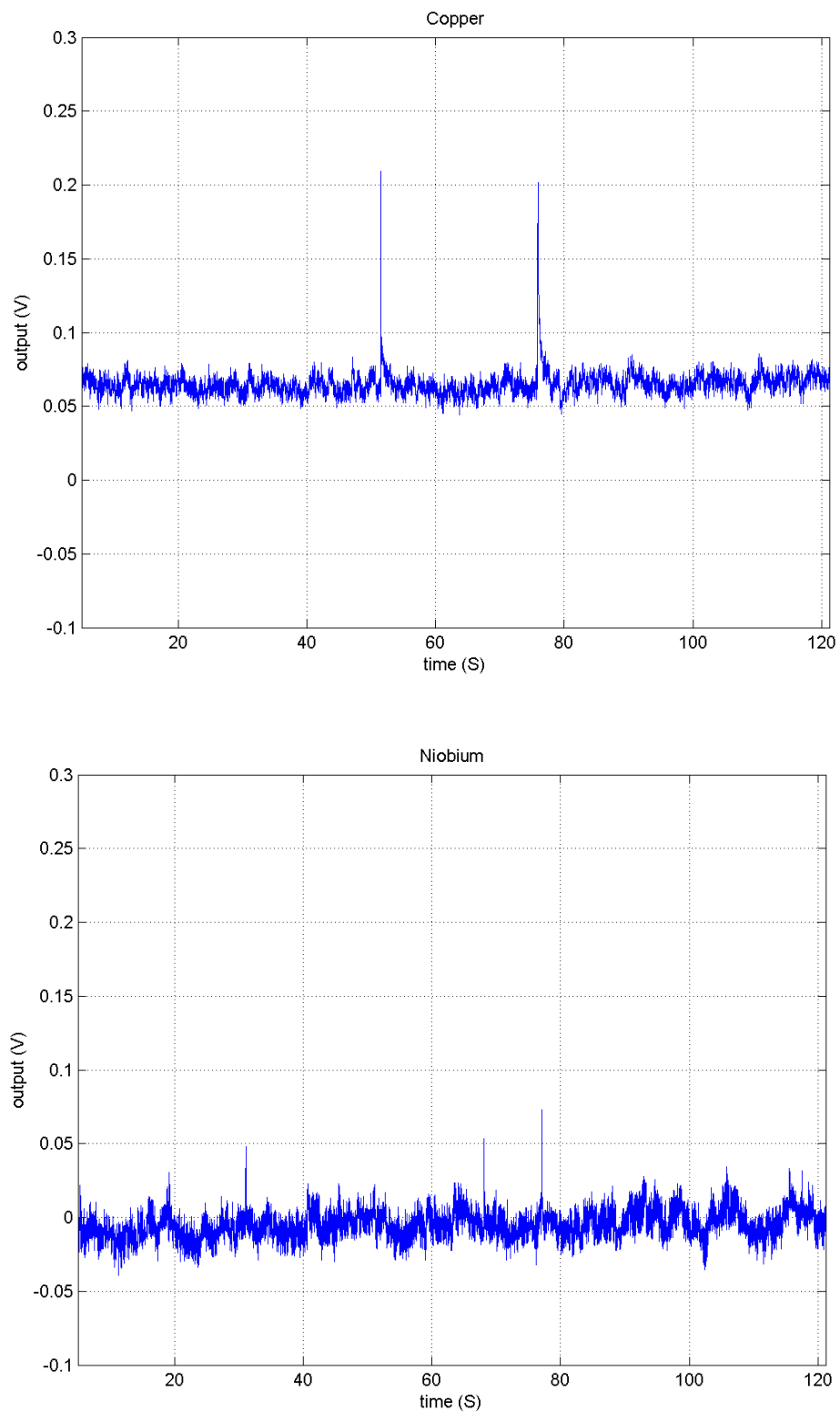


FIGURE 5.14: Top figure shows data captured from the EPS sensor with a bare copper electrode when irradiated by an Americium Beryllium neutron source. The lower figure shows data from the same sensor with a Niobium layer over the electrode, irradiated from the same source.

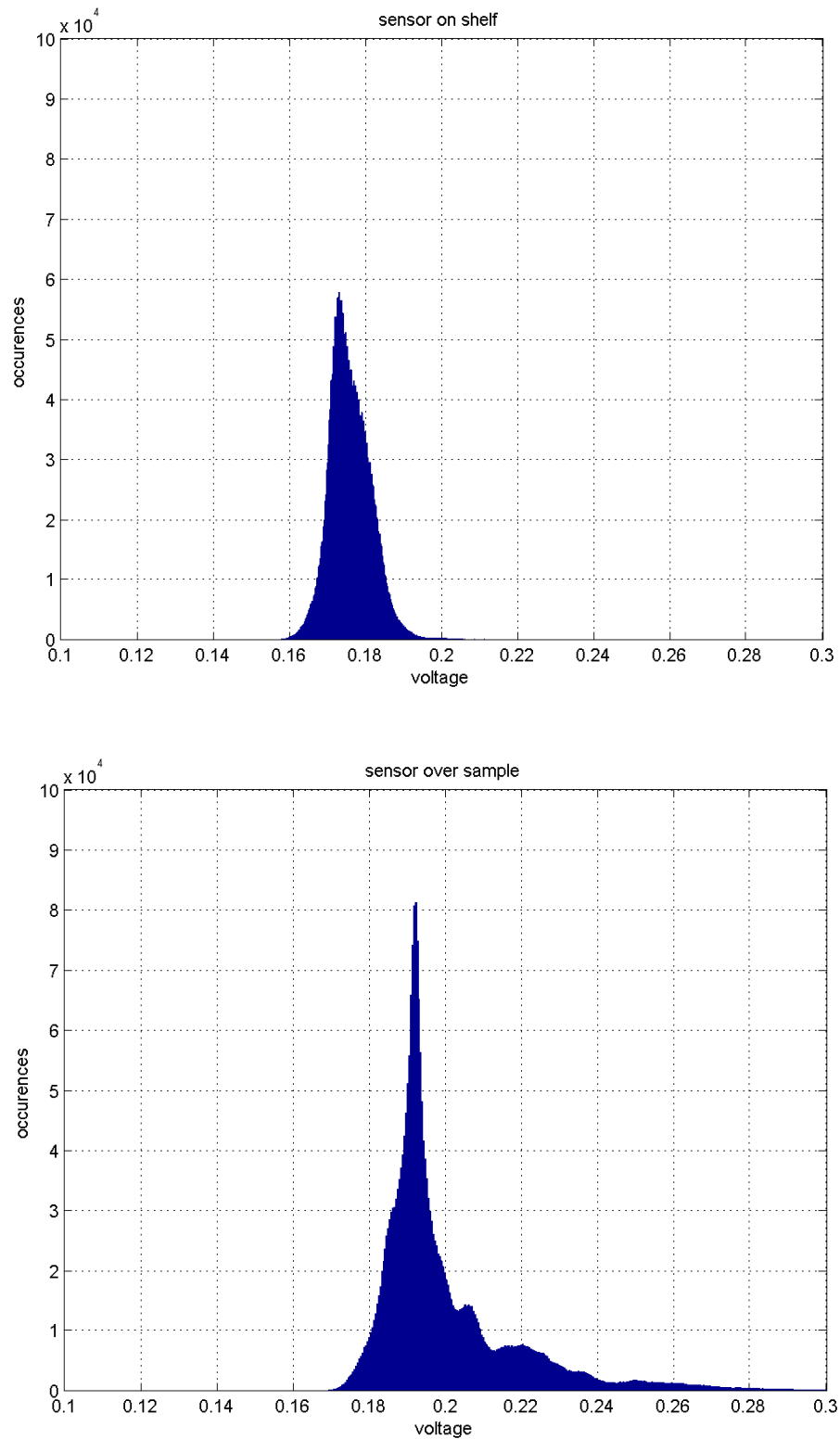


FIGURE 5.15: Comparison of pulse height spectrum captured with a Lithium Fluoride converter layer on the front electrode of the EPS sensor (top) in the presence of and (bottom) in the same room as - but not directly irradiated by - an Am-Be neutron source.

height spectrum clearly shows a DC shift in the presence of a neutron source, the presence of this DC shift is not expected and might be a result of the energy of the incident particles being integrated over time, producing a DC offset, or some conversion process within the converter layer - as covered in chapter 4, section 4.6.2, the interaction of fast neutrons in converter layers often results in energetic decay particles which may cause further reactions.

The Figure 5.16 shows a close-up of the pulse height spectrum, peaks in the data represent the arrival of charge on the electrode. Possible peaks are marked on the histogram. In order to prove that these peaks are the result of neutron interaction with the converter layer, the data is compared to Marsh' measured spectrum for a neutron source [128]. According to Marsh "peaks are observed near 3.1, 4.8, 6.6, 7.7 and 9.8 MeV. The observed peaks are compared with these values in table 5.3 where the values are normalised to the maximum value and compared. The small difference ($6 \geq \Delta\% \geq 1$) between the peaks suggests that the data is indeed a match and the peaks are a result of neutron interaction rather than other products such as gamma particles. Marsh' measurements of neutron source are shown in figure 5.17. The large peak at 0.192 in figure 5.16a is the "zero-point" - the value to which the system decays and consequently by far the largest number of samples are around this point. In order to match the peaks, the zero point and the final peak are taken as the first and last points, and the peak positions are normalised to the final value. No such spectrum is visible in the data for Carborane.

Processing the data to find the count rate yields the data shown in table 5.2. Entries for the old data sets refer to additional data captured in a previous experiment. The figures given are likely a very low accuracy, they were obtained using a Matlab function which finds turning points in data in which two thresholds values are required to adjust the sensitivity of the detection algorithm. Setting these variables to find peaks will either include noise as counts or will discard peaks as noise and the best compromise is different between data sets. Care was taken to standardise the data sets by removing the offsets and applying the same values to all data. It is clear from the table that copper and niobium have a lower cross section than the other two electrodes, but a distinction between the Lithium Fluoride and Niobium data cannot be made by this method. Exact details of the converter layers are also unknown - the purity and exact thickness of the materials affects the cross section

significantly. In order to calculate the neutron the solid angle is calculated. The distance between the source and the electrode is 0.5 m, the radius of the electrode 0.015 m and the activity of the source is 18 GBq. The angle subtended by the electrode as seen from the source is 3.44° .

$$\begin{aligned} \text{solid angle of the electrode} &= \\ \Omega &= 2\pi(1 - \cos(\frac{\theta}{2})) = 2\pi(1 - \cos(\frac{3.44}{2})) = 0.029\text{sr} \end{aligned} \quad (5.11)$$

$$\begin{aligned} \text{probability of neutron hitting electrode} &= \\ \frac{\Omega}{4\pi} &= \frac{0.029}{4\pi} = 2.31 \times 10^{-3} \end{aligned} \quad (5.12)$$

$$\begin{aligned} \text{average number of neutrons incident on electrode per second} &= \\ 2.31 \times 10^{-3} \times 18 \times 10^9 &= 41.58 \times 10^6 \end{aligned} \quad (5.13)$$

Hence the count rates in table 5.2 are far lower than the expected neutron flux. This suggests that the spikes observed in the data (figure 5.13) are the result of many neutrons arriving at the electrode at once, creating a greater charge than the arrival of any one individual neutron. The arrival of individual neutrons may be buried in the noise, otherwise may require a further reduction of the front end time constant of the sensor to be detected.

TABLE 5.2: Neutron Counts

material	counts	data time (seconds)	counts per minute
Lithium Flouride (old)	383	509	79
Lithium Flouride (new)	2586	2423	56
Carborane (old)	1005	1034	58
Carborane (new)	1137	1436	47.49
copper	2	120	1
niobium	4	120	2

TABLE 5.3: Neutron Source peaks

theoretical values (normalised)	measured values (normalised)	difference (%)
0.32	0.31	1
0.49	0.55	6
0.67	0.64	3
0.79	0.75	4
1	1	-

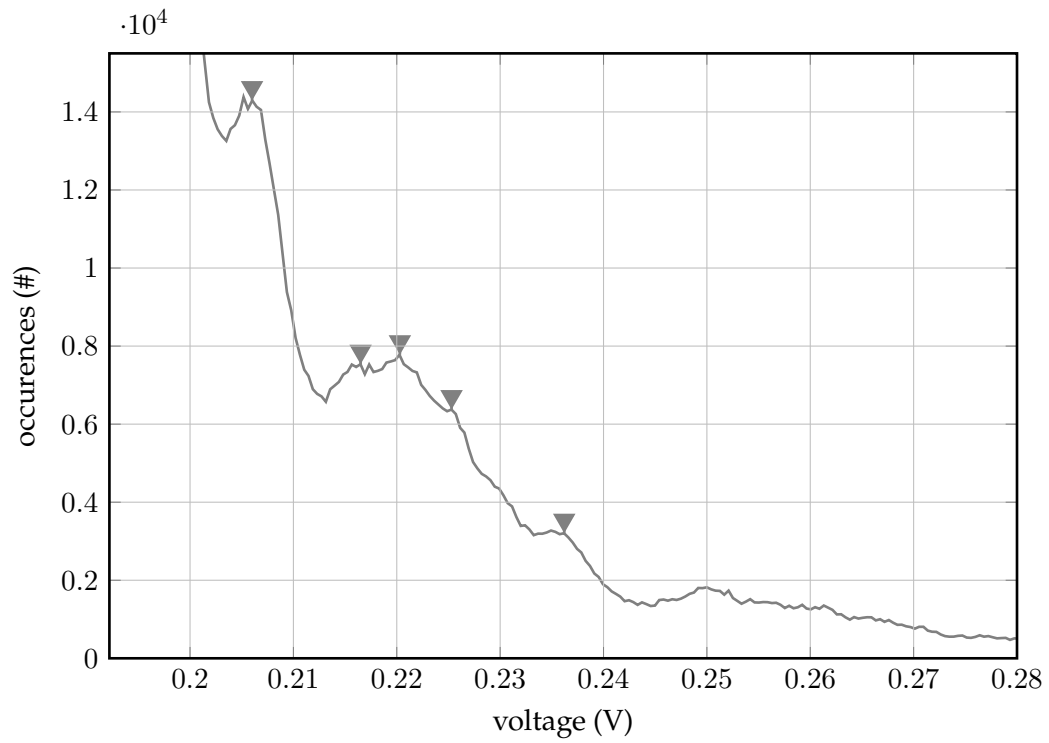


FIGURE 5.16: Close-up of pulse-height spectrum shown in 5.15. Arrow markers highlight peaks at 0.206, 0.2165, 0.2203, 0.2253, 0.2362

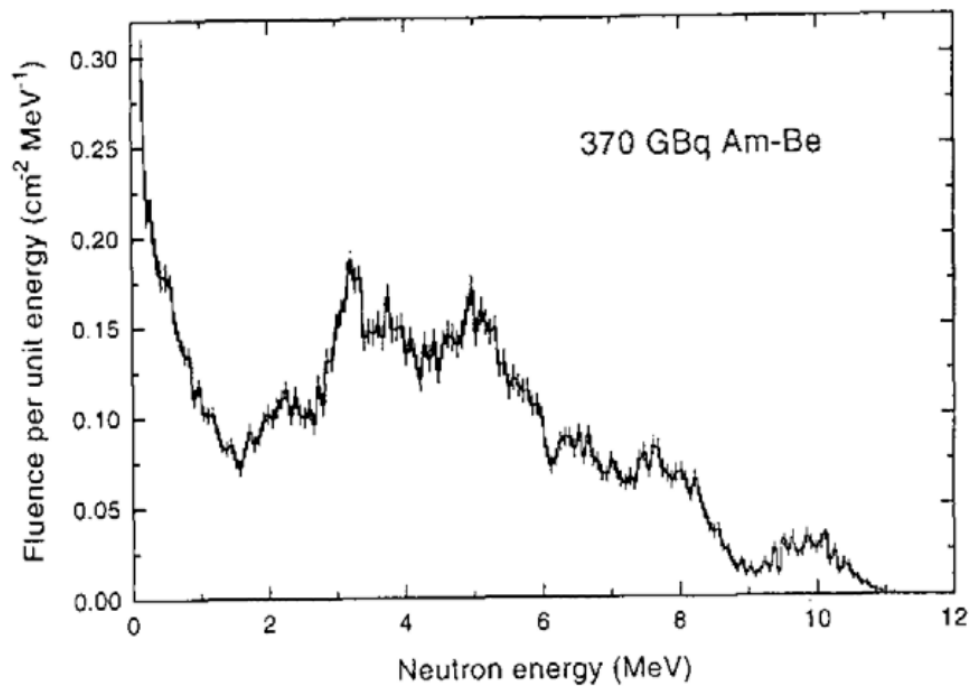


FIGURE 5.17: Neutron spectrum for a typical Americium Beryllium Source [128] for comparison with the spectrum captured from the EPS sensor.

From the results the conclusion drawn is that the EPS can be used in combination with an appropriate converter layer to detect neutrons. This is evidenced by the spikes observed in the time domain data (figures 5.13,5.14) this confirms the movement of charge over the front end of the sensor in the presence of a neutron source. Confirmation that this is caused by neutrons and not a product of other absorption products is given by figures 5.16,5.17 and table 5.3, which demonstrate that the neutron spectrum peaks documented by Marsh [128] for an Americium-Beryllium source are present in the data.

Further testing is required to verify whether the arrival of individual neutrons is possible, this is likely to require further modifications to the sensor to reduce the front-end RC time constant and improve the response time of the sensor. More testing is needed to verify the performance of the converter layer - converter layers with specified thickness and defined purities are required to fully define the behaviour of the sensor.

Chapter 6

Conclusions

6.1 Conclusions

The aim of the research undertaken in this thesis is to provide proof of concept for the use of the EPS in two areas related to security systems: low field NMR and particle detection. This closing chapter will address the conclusions to both parts of the work separately.

6.2 Low Field NMR

The work on low-field NMR aimed to prove electric-field acquisition yields higher signal-to-noise ratio than traditional magnetic-field detection in low-field NMR systems. Improvements in the signal captured in such systems has implications for the efficacy of NMR systems in general, but especially for low-field NMR where the design of systems is shaped by low signal levels. The research was undertaken to provide solutions for mobile drug and explosives discovery, but could also have implications in medical diagnosis.

In an NMR system, the induced magnetic moment is proportional to the DC field strength in which the sample is placed. Therefore at low static field strengths the signal-to-noise ratio is low. Traditional magnetic field detection suffers a further complication at these field strengths: the Larmor frequency - also proportional to the DC field - is low. By Gauss' law, the signal induced over the pick-up coil is proportional to the rate of change of flux, hence

at low frequency the pick-up coil is weakly coupled to the signal. A different approach is presented by using the EPS sensor in place of the pick-up coil to detect the electric field component of the free induction decay. By detecting the e-field the magnitude of the signal is no longer proportional to the frequency of precession. The primary source of signal loss instead becomes the capacitive coupling between the electrode and the sample, as the front-end impedance forms a capacitive divider with the coupling between the electrode and the sample.

In order to maximise the signal-to-noise ratio in the process of experimentation, the size of the sample was increased. This increases the number of spins in the DC field, increasing the signal strength. The DC field was provided by a Helmholtz pair. To extend the capability of the system the basic determination of compounds required for explosives detection, a commercial system - the ISpin NMR - was used. This system enables simple NMR spectroscopy by storing the measured signals digitally, averaging them and performing Fourier transforms. The resulting spectral content can then be examined for signature traces of compounds. This system also provided the excitation pulses and sequencing. The CPMG sequence which mitigates the effects of magnetic field inhomogeneities was used in testing and to attempt to detect a signal as the field inhomogeneities in the Helmholtz coil were found to be high.

Initial testing of the system at a higher field resonant circuit proved successful and confirmed the correct function of the ISpin NMR and accompanying GUI in performing signal acquisition, averaging, Fourier transform and the CPMG sequence. The accompanying GUI was modified to produce a Labview VI in which the pulse length, pulse amplitude and magnetic field strength were changed incrementally between scans. This is necessary as the NMR signal can be difficult to find, being critically affected by these three criteria.

During the course of the extensive testing on the low-field NMR apparatus, the system did not yield any free induction decay signals, either for magnetic or electric-field detection. In order to progress the research, a second system was designed: the proton magnetometer. This system also detects the effects of precession but only uses the a static DC magnet and the earth's magnetic field. In this system the performance of the static magnetic field applied in provoking the desired signal does not depend on the homogeneity of the field.

The detection of low-frequency precession signals can be demonstrated with the proton magnetometer, but the system is not able to determine the sample composition as with the pulsed NMR system. A positive result with the proton magnetometer could confirm higher signal-to-noise ratio with EPS sensors in low frequency NMR systems with e-field detection than with the traditional magnetic field detection.

Ultimately, the proton magnetometer also failed to produce a signal, even with the traditional magnetic field detection. The exact reasons for this are most likely different for each system. The field homogeneity was probably too low for the pulsed NMR system to work, meaning the individual spins are too out of phase to produce any net magnetic moment. It is assumed that with further tweaking and testing to the proton magnetometer, a signal may have been detected, but with the time scale of the project a pressing consideration, the work was abandoned in favour of the particle detection work.

The negative results of this area of the project do not indicate that the EPS is unsuitable for the purpose of low-field NMR signal acquisition: as a working NMR system with magnetic field detection could not be constructed, the e-field detection at low frequency could not be tested or appraised. A low-field, e-field detection NMR system may still provide a novel way of mitigating the low signal levels associated with low-field NMR.

6.3 Particle Detection

The research undertaken with the EPS as a particle detector aimed to provide a proof of concept: that the EPS can be used as a particle detector. It has been shown that detectors based on the EPS behave broadly in line with many types of traditional particle detectors, needing only simple modifications to provide a wide range of particle detection applications. Particle detectors based on the EPS present low cost alternatives to existing detectors, needing only few components.

Most particle detection techniques involve the creation of charged particles which are collected and measured. The critical design aspects were identified by Leo (covered in section [4.2](#)) as

- *Cross section for reactions within the detector* The incident radiation must have a high chance of interacting with the detector. In the case of alpha particles which ionise readily in air, the detector was similar to a parallel plate ionisation chamber. In the case of neutrons, appropriate converter materials were used - boron carbide and lithium fluoride showed clear evidence of neutron interaction. The detection of beta particles is a special case as the movement of which constitutes an electric current and so the cross section requires no special consideration.
- *Detector Mass* In order to measure the energy of incident radiation, an incident particle must lose enough energy in the detector volume. The range is used to define the length travelled through a particular material by a type of particle. The range for alpha particles in air is only a few cm, and the design of the grid assembly was made only one centimetre to provide adequate space for particles to ionise within the chamber. Neutron path length inside converter materials is much lower, owing to their interaction primarily by strong force rather than the comparatively long range Coulomb force. As the converter layers employed were thin and the energy of neutrons measured was high, the accuracy of calculation of the energy of particles was significantly reduced.
- *Inherent Detector Noise* In order to shield from noise the grid assembly was used. This assembly shields the electrometer from any unwanted e-field disturbances within the operational bandwidth of the sensor. The use of the large input resistance ensures that small currents are detectable above the noise floor.
- *Protective material surrounding the sensor* This is effectively covered by the grid-guard assembly, although little care was taken to ensure that the surrounding material did not interact with particles: alpha particles were detected satisfactorily and the interaction of fast neutrons with most materials is rare.

The experimental results covered various different aspects of detector behaviour. The conclusions drawn from analysis of all the particle detection results reported in chapter 5 are as follows -

- The EPS sensor detects ionic current due to ionisation from an alpha source. This current is detectable up to approximately 16 mm away from the grid. This is consistent with the the range of alpha particles in air.
- Altering the grid voltage affects the level of signal at the output of the sensor when used as an ionisation chamber. When a sufficient voltage is applied, the saturation region is reached where the application of more voltage does not yield higher output. The behaviour of the sensor in this regard is in line with Boag and Wilson's theoretical treatment of parallel plate ionisation chambers and can clearly be seen when plotting the data on the same curve, as in section
- The combination of parasitic capacitances from the chamber and the front end of the electrometer forms an RC network with the resistance of the electrometer. This RC network takes time to charge to a value and controls the behaviour of the sensor between pulse mode and current mode, as described in section 4.4.5. The results in chapter 5 show the capacitance can be manipulated by the use of positive AC feedback to minimise the effective capacitance of the front end and produce faster rise and fall times.
- Beta particles can be detected directly by the EPS in a vacuum. This is further evidence that the sensor is sensitive to the movement of beta particles, and the results seen in tests on americium are unlikely due to other factors.
- With appropriate converter layers, the EPS can be used to detect neutrons. Evidence of neutron collisions is seen from in those layers with high neutron cross sections but not those with low cross section. As further evidence that the signal seen in the tests is a result of neutron interaction, the neutron spectrum can be derived from the data captured from the lithium fluoride converter layer. The neutron spectrum was not however extrapolated from the results taken with the carborane layer.
- The sensor shows a consistent DC offset when irradiated by an americium source in a vacuum. Although the exact mechanism by which this offset appears is not confirmed, it is certainly due to the presence of the source, and as such the sensor can be said to detect the presence of alpha particles directly.

Confirmation of the EPS sensor for the detection of particles means that sensors can be made which function broadly in line with traditional detectors but can be made very small and at low cost. This is of interest in security applications.

6.4 Further Work

Here follows a recap of suggestions for further work on the detection of low-field NMR signals detailed in chapters 2 and 3 -

- The NMR experiment yielded no signals, and as outlined in chapter 3 the most likely causes were reduced with the aid of the automated testing procedure to either the homogeneity of the magnetic field or the low signal level produced by the experiment. To progress this research further the Helmholtz coil should be replaced with a high homogeneity DC field in which to conduct the experiment. The possibility of the low signal level may be eliminated by altering the detection electronics in the Ispin. The Ispin is known from the information provided in its datasheet to be the piece of equipment in the detection system with the highest noise floor.

Here follow suggestions for further work in the particle detection applications

- Although the testing provided clear evidence of a DC offset when in the presence of an alpha source, further investigation is needed to explain the mechanism by which this offset appears. Two suggestions are made as to how to test the conjecture that the offset is a result of delta electrons escaping the front electrode: firstly, the use of two different energy sources may be used in the same experiment. If the assumption is correct the higher energy source would result in a larger DC offset. Similarly an electrode covered with a significantly different ionisation potential to copper would also produce a change in the DC offset - higher ionisation potentials leading to a lower DC offset and vice-versa.
- The use of the EPS as a pulse-mode detector can be explored by reducing the front end RC time constant with feedback techniques. In this thesis the time constant was

not reduced far enough to detect the arrival of individual particles, but tests on the effect of feedback on rise and fall times prove the capability to alter the front end capacitance. The use of extra grids is often used in pulse-mode sensors to decrease the positional dependency of the signal [24]. The grid guard assembly could be modified to incorporate such a grid along with feedback to reduce the capacitance and produce a pulse-mode ionisation chamber with the capability of switching between pulse mode and current mode by the application of feedback, and also with the existing advantages of being low cost.

- Further investigation of the behaviour of the EPS with appropriate converter layers could yield a low cost EPS based neutron detector capable of providing detailed spectra of neutron radiation. This is of importance in security applications where portable detectors are needed, but also in industrial monitoring of nuclear power plants where large numbers of sensors might be beneficial in monitoring neutron flux throughout a reactor.

Bibliography

- [1] J. M. B. Kellogg, I. I. Rabi, N. F. Ramsey, and J. R. Zacharias, "The magnetic moments of the proton and the deuteron. the radiofrequency spectrum of h_2 in various magnetic fields," *Phys. Rev.*, vol. 56, pp. 728–743, Oct 1939. [Online]. Available: <http://link.aps.org/doi/10.1103/PhysRev.56.728>
- [2] C. Gorter and L. Broer, "Negative result of an attempt to observe nuclear magnetic resonance in solids," *Physica*, vol. 9, no. 6, pp. 591 – 596, 1942. [Online]. Available: <http://www.sciencedirect.com/science/article/pii/S0031891442800737>
- [3] I. I. Rabi, J. R. Zacharias, S. Millman, and P. Kusch, "A new method of measuring nuclear magnetic moment," *Phys. Rev.*, vol. 53, pp. 318–318, Feb 1938. [Online]. Available: <http://link.aps.org/doi/10.1103/PhysRev.53.318>
- [4] E. M. Purcell, H. C. Torrey, and R. V. Pound, "Resonance absorption by nuclear magnetic moments in a solid," *Phys. Rev.*, vol. 69, pp. 37–38, Jan 1946. [Online]. Available: <http://link.aps.org/doi/10.1103/PhysRev.69.37>
- [5] F. Bloch, "Nuclear induction," *Phys. Rev.*, vol. 70, pp. 460–474, Oct 1946. [Online]. Available: <http://link.aps.org/doi/10.1103/PhysRev.70.460>
- [6] F. Bloch, W. W. Hansen, and M. Packard, "The nuclear induction experiment," *Phys. Rev.*, vol. 70, pp. 474–485, Oct 1946. [Online]. Available: <http://link.aps.org/doi/10.1103/PhysRev.70.474>
- [7] E. L. Hahn, "Spin echoes," *Phys. Rev.*, vol. 80, pp. 580–594, Nov 1950. [Online]. Available: <http://link.aps.org/doi/10.1103/PhysRev.80.580>
- [8] Center for high field Nuclear Magnetic Resonance. [Online]. Available: <http://www.ens-lyon.eu/>

- [9] M. Greenfield, A. Ronemus, R. Vold, R. Vold, P. Ellis, and T. Raidy, "Deuterium quadrupole-echo {NMR} spectroscopy. iii. practical aspects of lineshape calculations for multiaxis rotational processes," *Journal of Magnetic Resonance (1969)*, vol. 72, no. 1, pp. 89 – 107, 1987. [Online]. Available: <http://www.sciencedirect.com/science/article/pii/0022236487901776>
- [10] "Electron spin resonance," pp. X001–X004, 1991. [Online]. Available: <http://dx.doi.org/10.1039/9781847553485>
- [11] B. Manz, A. Coy, R. Dykstra, C. Eccles, M. Hunter, B. Parkinson, and P. Callaghan, "A mobile one-sided {NMR} sensor with a homogeneous magnetic field: The nmr-mole," *Journal of Magnetic Resonance*, vol. 183, no. 1, pp. 25 – 31, 2006. [Online]. Available: <http://www.sciencedirect.com/science/article/pii/S1090780706002229>
- [12] *Picture of large NMR spectrometer*. Universität Düsseldorf. [Online]. Available: <http://www.uni-duesseldorf.de/MathNat/ipb/index.php?index=1317>
- [13] W. G. Lee, Y.-G. Kim, B. G. Chun, U. Demirci, and A. Khademhosseini, "Nano\microfluidics for diagnosis of infectious diseases in developing countries," *Advanced Drug Delivery Reviews*, pp. 449–457, 2010.
- [14] B. Blümich, Q. Gong, E. Byrne, and M. Greferath, "{NMR} with excitation modulated by frank sequences," *Journal of Magnetic Resonance*, vol. 199, no. 1, pp. 18 – 24, 2009. [Online]. Available: <http://www.sciencedirect.com/science/article/pii/S1090780709000792>
- [15] R. Dykstra, M. Adams, P. Callaghan, A. Coy, C. Eccles, M. Hunter, T. Southern, and R. Ward, "A portabe nuclear magnetic resonance sensor system," *Sensors and Transducers Journal*, vol. 90, pp. 255–266, 2008.
- [16] N. Goga, A. Pirnau, L. Szabo, R. Smeets, D. Riediger, O. Cozar, and B. Blumich, "Mobile NMR application to materials and biomedecine," *Journal of Optoelectronics and Advanced Materials*, vol. 8, no. 4, pp. 1430–1434, 2006.

- [17] R. McDermott, S. Lee, B. Haken, A. Trabesinger, A. Pines, and J. Clarke, "Microtesla MRI with a superconducting quantum interference device," *Proceedings of the National Academy of Sciences*, vol. 101, no. 21, pp. 7857–7861, 2004.
- [18] R. Korber, A. Casey, A. Shibahara, M. Piscitelli, B. P. Cowan, C. P. Lusher, J. Saunders, D. Drung, and T. Schurig, "Nuclear magnetic resonance on room temperature samples in nanotesla fields using a two-stage DC superconducting quantum interference device sensor," *Applied Physics Letters*, vol. 91, no. 14, 2007. [Online]. Available: <http://scitation.aip.org/content/aip/journal/apl/91/14/10.1063/1.2794028>
- [19] V. Zotev, A. Matlashov, P. Volegov, I. Savukov, M. Epsy, J. Mosher, J. Gomez, and R. K. Jr., "Microtesla MRI of the human brain combined with MEG," *Journal of Magnetic Resonance*, no. 194, pp. 115–120, 2008.
- [20] A. Aydin, "Application of electric potential sensors in nuclear magnetic resonance signal acquisition," PhD, University of Sussex, Engineering and Informatics, 2006.
- [21] S. Kumar and P. J. Prado, "Detection of concealed liquid explosives and illicit drugs in unopened bottles," in *Explosives Detection Using Magnetic and Nuclear Resonance Techniques*, ser. NATO Science for Peace and Security Series B: Physics and Biophysics, J. Fraissard and O. Lapina, Eds. Springer Netherlands, 2009, pp. 73–79. [Online]. Available: http://dx.doi.org/10.1007/978-90-481-3062-7_5
- [22] E. Gudmundson, A. Jakobsson, I. Poplett, and J. A. S. Smith, "Detection and classification of liquid explosives using nmr," in *Acoustics, Speech and Signal Processing, 2009. ICASSP 2009. IEEE International Conference on*, April 2009, pp. 3053–3056.
- [23] J. Thompson, "Reviews-on the theory of the conduction of electricity through gases by charged ions," *The Journal of Physical Chemistry*, vol. 5, no. 1, pp. 87–87, 1900.
- [24] O. Frisch, *British Atomic Energy Report*, 1944, vol. BR-49.
- [25] D. S. McGregor, Z. He, H. A. Seifert, D. K. Wehe, and R. A. Rojas, "Single charge carrier type sensing with a parallel strip pseudo-frisch-grid CdZnTe semiconductor radiation detector," *Applied Physics Letters*, vol. 72, no. 7, pp. 792–794, 1998.

- [Online]. Available: <http://scitation.aip.org/content/aip/journal/apl/72/7/10.1063/1.120895>
- [26] N. Takata and Z. Yin, "Diffusion loss of ions and charge collection volumes for thimble type ionisation chambers," *Radiation Protection Dosimetry*, vol. 81, no. 3, pp. 229–232, 1999.
- [27] M. Bellicoso, R. Machrafi, and L. Lu, "Simulator design and lab scale test of a gas filling station for Geiger Muller detectors," pp. 14–17, Dec 2013.
- [28] A. Al-Adili, F.-J. Hamsch, R. Bencardino, S. Pomp, S. Oberstedt, and S. Zeynalov, "On the Frisch–Grid signal in ionization chambers," *Nuclear Instruments and Methods in Physics Research Section A: Accelerators, Spectrometers, Detectors and Associated Equipment*, vol. 671, no. 0, pp. 103 – 107, 2012. [Online]. Available: <http://www.sciencedirect.com/science/article/pii/S016890021102256X>
- [29] H. Timmers, T. Ophel, and R. Elliman, "Simplifying position-sensitive gas-ionization detectors for heavy ion elastic recoil detection," *Nuclear Instruments and Methods in Physics Research Section B: Beam Interactions with Materials and Atoms*, vol. 161–163, no. 0, pp. 19–28, 2000. [Online]. Available: <http://www.sciencedirect.com/science/article/pii/S0168583X99006679>
- [30] M. Johnson, "Radiation protection instrument manual PNL-MA-562," U.S. Department of Energy, 2013.
- [31] L. P. Neves, A. P. Perini, G. P. dos Santos, M. Xavier, H. J. Khoury, and L. V. Caldas, "Characterization of a homemade ionization chamber for radiotherapy beams," *Applied Radiation and Isotopes*, vol. 70, no. 7, pp. 1291 – 1295, 2012, proceedings of the 8th International Topical Meeting on Industrial Radiation and Radioisotope Measurement Applications (IRRMA-8). [Online]. Available: <http://www.sciencedirect.com/science/article/pii/S0969804311006038>
- [32] O. Müller, J. Stötzel, D. Lützenkirchen-Hecht, and R. Frahm, "Gridded ionization chambers for time resolved x-ray absorption spectroscopy," *Journal of Physics: Conference Series*, vol. 425, no. 9, p. 092010, 2013. [Online]. Available: <http://stacks.iop.org/1742-6596/425/i=9/a=092010>

- [33] K. Wittenburg, "Beam loss monitors," 2008. [Online]. Available: <http://cds.cern.ch/record/1213279/files/p249.pdf>
- [34] Steinmeyer, "GM pancake detectors: everything you've wanted to know," *RSO magazine*, vol. 10, no. 5, pp. 7–17, 2005.
- [35] G. Mie, "Der elektrische strom in ionisierter luft in einem ebenen kondensator," *Annalen der Physik*, vol. 318, no. 5, pp. 857–889, 1904. [Online]. Available: <http://dx.doi.org/10.1002/andp.18943180502>
- [36] R. Seeliger, "The theory of the conduction of electricity in dense gases," *Annalen der Physik*, vol. 33, pp. 319–380, 1910.
- [37] J. Townsend, *Electricity in Gases*. Clarendon Press, 1915.
- [38] J. W. Boag and T. Wilson, "The saturation curve at high ionization intensity," *British Journal of Applied Physics*, vol. 3, no. 7, p. 222, 1952. [Online]. Available: <http://stacks.iop.org/0508-3443/3/i=7/a=305>
- [39] E. A. Sprinkle and P. A. Tate, "The saturation curve in cylindrical and spherical ionization chambers," *Physics in Medicine and Biology*, vol. 11, no. 1, p. 31, 1966. [Online]. Available: <http://stacks.iop.org/0031-9155/11/i=1/a=303>
- [40] R. Rosen and E. P. George, "Ion distributions in plane and cylindrical chambers," *Physics in Medicine and Biology*, vol. 20, no. 6, p. 990, 1975. [Online]. Available: <http://stacks.iop.org/0031-9155/20/i=6/a=011>
- [41] A. F. Bielajew, "The effect of free electrons on ionization chamber saturation curves," *Medical Physics*, vol. 12, no. 2, pp. 197–200, 1985. [Online]. Available: <http://scitation.aip.org/content/aapm/journal/medphys/12/2/10.1118/1.595783>
- [42] A. T. Cameron and W. Ramsay, "CXVIII-some properties of radium emanation," *J. Chem. Soc., Trans.*, vol. 91, pp. 1266–1282, 1907. [Online]. Available: <http://dx.doi.org/10.1039/CT9079101266>
- [43] A. Krebs, "Ein demonstrationsversuch zur emanationsdiffusion," *Annalen der Physik*, vol. 431, no. 5, pp. 330–332, 1941. [Online]. Available: <http://dx.doi.org/10.1002/andp.19414310504>

- [44] S. Curran and W. Baker, "A photoelectric alpha particle detector," *U.S. Atomic Energy Commission Rpt.*, vol. MDDC 1296, 1944.
- [45] K. Mukai, N. Tawa, K. Ikegami, T. Miyauchi, N. Anabuki, E. Miyati, H. Tsunemi, Y. Ogasaka, K. Tamura, R. Shibata, and K. Myaguchi, "Development of high resolution wide-band x-ray detector: Scintillator-deposited charge-coupled device," *8th International Conference of X-ray Microscopy*, pp. 201–203, 2005.
- [46] C. Guardiola, C. Fleta, D. Quirion, J. Rodríguez, M. Lozano, F. Teixidor, C. Viñas, A. R. Popescu, C. Domingo, and K. Amgarou, "First investigations of a silicon neutron detector with a carborane converter," *Journal of Instrumentation*, vol. 6, no. 11, p. P11001, 2011. [Online]. Available: <http://stacks.iop.org/1748-0221/6/i=11/a=P11001>
- [47] G. Thomas, "A boron-loaded liquid scintillation neutron detector using a single photomultiplier," *Nuclear Instruments and Methods*, vol. 17, no. 2, pp. 137 – 139, 1962. [Online]. Available: <http://www.sciencedirect.com/science/article/pii/0029554X62901507>
- [48] C. Combes, P. Dorenbos, R. Hollander, and C. van Eijk, "A thermal-neutron scintillator with n/gamma discrimination LiBaF₃ : Ce,Rb," *Nuclear Instruments and Methods in Physics Research*, vol. 416, pp. 364–370, 1998.
- [49] F. P. Doty, "Boron nitride solid state neutron detector," U.S. Patent US 6 727 504 B1, 28 September 2001. [Online]. Available: <http://www.google.com.br/patents/US6727504>
- [50] H. Y. Lee and J. K. Kim, "Development of a neutron sensitive PCP ionization chamber," *Journal of the Korean Nuclear Society*, vol. 6, no. 1, pp. 27–35, 1974.
- [51] P. Maruvada, R. D. Dallaire, and R. Pedneault, "Development of field-mill instruments for ground-level and above-ground electric field measurement under HVDC transmission lines," *Power Apparatus and Systems, IEEE Transactions on*, vol. PAS-102, no. 3, pp. 738–744, March 1983.
- [52] H. C. J., T. Clark, and R. Prance, "Electric potential probes - new directions in the remote sensing of the human body," *Measurement Science and Technology*, vol. 13,

- no. 2, p. 163, 2002. [Online]. Available: <http://stacks.iop.org/0957-0233/13/i=2/a=304>
- [53] C. J. Harland, T. D. Clark, and R. J. Prance, "Remote detection of human electroencephalograms using ultrahigh input impedance electric potential sensors," *Applied Physics Letters*, vol. 81, no. 17, pp. 3284–3286, 2002. [Online]. Available: <http://scitation.aip.org/content/aip/journal/apl/81/17/10.1063/1.1516861>
- [54] H. Prance, P. Watson, S. Beardsmore-Rust, C. Harland, and R. Prance, "Measurement of physiological parameters using ultra-high impedance electric potential sensors." National Physical Laboratory, 2009.
- [55] N. Steinhausen, H. Prance, and R. Prance, "Human computer interface based on eye movement (EOG) signals," *Association for the Advancement of Assistive Technology in Europe*, 2011.
- [56] S. Mukherjee, P. Watson, and R. J. Prance, "Non-contact measurement of local conductivity variations in carbon fibre based composite materials," *Journal of Physics: Conference Series*, vol. 307, no. 1, p. 012034, 2011. [Online]. Available: <http://stacks.iop.org/1742-6596/307/i=1/a=012034>
- [57] S. Mukherjee, "Broadband electric field sensing and its application to material characterisation and nuclear quadrupole resonance," PhD, University of Sussex, Engineering and Informatics, 2012.
- [58] P. Watson, R. J. Prance, S. T. Beardsmore-Rust, and H. Prance, "Imaging electrostatic fingerprints with implications for a forensic timeline," *Forensic Science International*, vol. 209, no. 1–3, pp. e41 – e45, 2011. [Online]. Available: <http://www.sciencedirect.com/science/article/pii/S0379073811001101>
- [59] Texas Instruments, *OPA657 datasheet*, 2001. [Online]. Available: <http://www.ti.com>
- [60] S. Beardsmore-Rust, "Remote applications of electric potential sensors in electrically shielded environments," PhD, Engineering and Informatics, Sussex University, 2010.

- [61] H. Prance, P. Watson, R. J. Prance, and S. T. Beardsmore-Rust, "Position and movement sensing at metre standoff distances using ambient electric field," *Measurement Science and Technology*, vol. 23, no. 11, p. 115101, 2012. [Online]. Available: <http://stacks.iop.org/0957-0233/23/i=11/a=115101>
- [62] S. Mukherjee, P. Watson, and R. J. Prance, "Microscopic resolution broadband dielectric spectroscopy," *Journal of Physics: Conference Series*, vol. 310, no. 1, p. 012003, 2011. [Online]. Available: <http://stacks.iop.org/1742-6596/310/i=1/a=012003>
- [63] *Quarks: Is that all there is?* Openstax CNX. [Online]. Available: <http://cnx.org/>
- [64] W. W. Paudler, *Nuclear magnetic Resonance: General Concepts and Applications*, 1st ed. John Wiley and Sons, 1987.
- [65] "Electron paramagnetic resonance: Theory," University of California, Davis, 2013. [Online]. Available: http://chemwiki.ucdavis.edu/@api/deki/files/9303/Zeman_Effect.jpg
- [66] T. Soderberg, *Organic Chemistry With a Biological Emphasis*. University of California, Davis, January 2013. [Online]. Available: <http://chemwiki.ucdavis.edu/>
- [67] T. Farrar, *Pulse and Fourier Transform NMR*, 1st ed. Academic Press, 1971.
- [68] R. K. Wangsness and F. Bloch, "The dynamical theory of nuclear induction," *Phys. Rev.*, vol. 89, pp. 728–739, Feb 1953. [Online]. Available: <http://link.aps.org/doi/10.1103/PhysRev.89.728>
- [69] J. Hornak, "Basics of NMR," Chester F. Carlson Centre for Imaging Science, 1997. [Online]. Available: <http://www.cis.rit.edu/htbooks/nmr/>
- [70] R. Freeman and H. D. W. Hill, "Fourier transform study of NMR spin-lattice relaxation by "progressive saturation"," *The Journal of Chemical Physics*, vol. 54, no. 8, pp. 3367–3377, 1971. [Online]. Available: <http://scitation.aip.org/content/aip/journal/jcp/54/8/10.1063/1.1675352>
- [71] D. Canet, G. C. Levy, and I. R. Peat, "Time saving in ^{13}C spin-lattice relaxation measurements by inversion-recovery," *Journal of Magnetic Resonance (1969)*, vol. 18,

- no. 1, pp. 199 – 204, 1975. [Online]. Available: <http://www.sciencedirect.com/science/article/pii/0022236475902383>
- [72] H. Torrey, "Transient nutations in nuclear magnetic resonance," *Physical Review*, vol. 76, no. 8, pp. 1059–1072, Oct 1949.
- [73] "Biological magnetic resonance data bank," Worldwide Protein Data Bank, 2013. [Online]. Available: <http://www.bmrb.wisc.edu/>
- [74] R. R. Ernst and W. A. Anderson, "Application of Fourier transform spectroscopy to magnetic resonance," *Review of Scientific Instruments*, vol. 37, no. 1, pp. 93–102, 1966. [Online]. Available: <http://scitation.aip.org/content/aip/journal/rsi/37/1/10.1063/1.1719961>
- [75] H. Y. Carr and E. M. Purcell, "Effects of diffusion on free precession in nuclear magnetic resonance experiments," *Phys. Rev.*, vol. 94, pp. 630–638, May 1954. [Online]. Available: <http://link.aps.org/doi/10.1103/PhysRev.94.630>
- [76] S. Meiboom and D. Gill, "Modified spin echo method for measuring nuclear relaxation times," *Review of Scientific Instruments*, vol. 29, no. 8, pp. 688–691, 1958. [Online]. Available: <http://scitation.aip.org/content/aip/journal/rsi/29/8/10.1063/1.1716296>
- [77] UC Davis chem-wiki, "CPMG signal acquisition," University of California, Davis, 2013. [Online]. Available: [http://chemwiki.ucdavis.edu/Physical_Chemistry/Spectroscopy/Magnetic_Resonance_Spectroscopies/Nuclear_Magnetic_Resonance/NMR%3A_Experimental/Solid_State_Experiments/Car-Purcel-Meiboom-Gill_\(CPMG\)_Echo_Train_Acquisition](http://chemwiki.ucdavis.edu/Physical_Chemistry/Spectroscopy/Magnetic_Resonance_Spectroscopies/Nuclear_Magnetic_Resonance/NMR%3A_Experimental/Solid_State_Experiments/Car-Purcel-Meiboom-Gill_(CPMG)_Echo_Train_Acquisition)
- [78] N. Bloembergen, E. M. Purcell, and R. V. Pound, *Relaxation Effects in Nuclear Magnetic Resonance Absorption*. American Physical Society, Apr 1948, vol. 73. [Online]. Available: <http://link.aps.org/doi/10.1103/PhysRev.73.679>
- [79] C. Wolff, "Synchronous detector," radartutorial.eu, 2013. [Online]. Available: <http://www.radartutorial.eu/10.processing/pic/IandQ.print.png>
- [80] Intersil, *EL8100 datasheet*, 2010. [Online]. Available: <http://www.intersil.com>

-
- [81] F. Connor, *Noise: introductory Topics in Electronics and Telecommunication*, 1st ed. Edward Arnold, 1973.
- [82] Texas Instruments, *OP827 datasheet*, 2006 revised 2012. [Online]. Available: <http://www.ti.com>
- [83] S. T. Inc., "I-spin NMR owner's manual," 2013. [Online]. Available: <http://www.spincore.com/CD/iSpin/iSpinManual.pdf>
- [84] *Model: AU-1447 description*. Miteq Inc. [Online]. Available: <https://www.miteq.com>
- [85] F. Terman, *Radio Engineering*. McGraw-Hill, 1937.
- [86] V. Siliconix, "Power mosfet," 2010. [Online]. Available: <http://www.vishay.com/docs/91127/sihfd110.pdf>
- [87] Fortney, *Principles of Electronics: Analog and Digital*, 1st ed. Harcourt Brace Janovich Inc., 1987.
- [88] J. D. Krauss and D. A. Fleisch, *Electromagnetics with Applications*, 5th ed. McGraw-Hill, 1999.
- [89] Calogic, *N-Channel JFET high frequency amplifier*. U310 datasheet. [Online]. Available: <http://www.datasheetcatalog.com/>
- [90] M. Levitt, *Spin Dynamics*, 2nd ed. John Wiley and Sons, 2008.
- [91] S. Vathyam, S. Lee, and W. Warren, "Homogeneous NMR spectra in inhomogeneous fields," *Science*, vol. 272, pp. 92–96, 1996.
- [92] B. Hutchins, "Musical engineers handbook," *Electronotes*, pp. 78–85, 1973.
- [93] S. Hollos and R. Hollos, *Signals from the subatomic world: how to build a proton magnetometer*. Abrazol Publishing, 2003.
- [94] L. Huggard, "Proton magnetometer," *Practical Electronics*, 1970.
- [95] W. Ruhunusiri and M. Jayananda, "Construction of a proton magnetometer," *Proceedings of the Technical Sessions*, no. 28, pp. 78–85, 2008.

- [96] International Rectifier, *IR6215 datasheet*, 1998. [Online]. Available: <http://www.irf.com>
- [97] J. Chung, M. Donahoe, C. Schmandt, I.-J. Kim, P. Razavai, and M. Wiseman, "Indoor location sensing using geo-magnetism," in *Proceedings of the 9th International Conference on Mobile Systems, Applications, and Services*, ser. MobiSys '11. New York, NY, USA: ACM, 2011, pp. 141–154. [Online]. Available: <http://doi.acm.org/10.1145/1999995.2000010>
- [98] M. Skakala, V. Zrubec, and J. Manka, "Active compensation for ambient magnetic noise in the unshielded environment," *Measurement Science and Technology*, vol. 4, no. 4, p. 468, 1993. [Online]. Available: <http://stacks.iop.org/0957-0233/4/i=4/a=005>
- [99] M. H. Afzal, V. Renaudin, and G. Lachapelle, "Assessment of indoor magnetic field anomalies using multiple magnetometers," in *Proceedings of the 23rd International Technical Meeting of The Satellite Division of the Institute of Navigation*, ser. GNSS 2010, 2010, pp. 525–533.
- [100] W. R. Leo, *Techniques for Nuclear and Particle Physics Experiments*, 2nd ed. Springer-Verlag, 1994.
- [101] R. Gilmore, *Single Particle Detection and Measurement*, 1st ed. Taylor and Francis, 1992.
- [102] W. Burcham, *Nuclear Physics an Introduction, 2nd Edition*, 2nd ed. Longman, 1973.
- [103] C. Grupen and B. Shwartz, *Particle Detectors*, 2nd ed. Cambridge University Press, 2008.
- [104] *Range of Alpha Particles*. University of Saskatchewan. [Online]. Available: http://physics.usask.ca/~bzulkosk/modphyslab/phys251manual/alpha_2011.pdf
- [105] R. C. Fernow, *Introduction to Exsperimental Particle Physics*, 1st ed. Cambridge University Press, 1987.
- [106] *Principle of an Ionisation Chamber*. European Nuclear Society. [Online]. Available: <http://www.euronuclear.org>

- [107] G. Knoll, *Radiation Detection and Measurement*, 4th ed. John Wiley and Sons, 1976.
- [108] S. Korff, *Electron and Nuclear Counters*, 2nd ed. D. Van Nostrand Company, 1955.
- [109] K. Kleinknecht, *Detector for Particle Radiation*, 1st ed. Cambridge University Press, 1985.
- [110] A. Perris and G. Zarris, "Specific primary ionisation for electrons, protons and alpha particles incident on water," *Physics in Medicine and Biology*, vol. 34, no. 8, p. 1113, 1989. [Online]. Available: <http://stacks.iop.org/0031-9155/34/i=8/a=012>
- [111] R. Singru, *Introduction to Experimental Nuclear Physics*, 2nd ed. Wiley Eastern, 1974.
- [112] J. Bushberg, J. Seibert, E. L. Jr., and J. Boone, *The essential physics of medical imaging*. Lippincott Williams and Wilkins, 2011.
- [113] Z. He, "Review of the Shockley–Ramo theorem and its application in semiconductor gamma-ray detectors," *Nuclear Instruments and Methods in Physics Research*, vol. 463, pp. 250–267, 2000.
- [114] W. Shockley, "Currents to conductors induced by a moving point charge," *Journal of Applied Physics*, vol. 9, no. 10, pp. 635–636, 1938. [Online]. Available: <http://scitation.aip.org/content/aip/journal/jap/9/10/10.1063/1.1710367>
- [115] S. Ramo, "Currents induced by electron motion," *Proceedings of the IRE*, vol. 27, no. 9, pp. 584–585, Sept 1939.
- [116] M. Weinhaus and J. Meli, "Collection efficiency of an ionisation chamber in a pulsed swept beam: collimator scatter effects," *Physics in Medicine and Biology*, vol. 31, no. 10, pp. 1147–1155, 1986.
- [117] T. Yamamoto, K. Oda, H. Kobayashi, and M. Kawanishi, "Collection efficiency of a parallel-plate ionization chamber exposed to pulsed x-rays," *Nuclear Instruments and Methods*, vol. 172, no. 3, pp. 447 – 454, 1980. [Online]. Available: <http://www.sciencedirect.com/science/article/pii/0029554X8090333X>
- [118] J. R. Greening, "Saturation characteristics of parallel-plate ionization chambers," *Physics in Medicine and Biology*, vol. 9, no. 2, p. 143, 1964. [Online]. Available: <http://stacks.iop.org/0031-9155/9/i=2/a=302>

- [119] M. Boutillon, "Volume recombination parameter in ionization chambers," *Physics in Medicine and Biology*, vol. 43, no. 8, p. 2061, 1998. [Online]. Available: <http://stacks.iop.org/0031-9155/43/i=8/a=005>
- [120] N. Takata and Matiullah, "Dependence of the value of m on the lifetime of ions in parallel-plate ionization chambers," *Physics in Medicine and Biology*, vol. 36, no. 4, p. 449, 1991. [Online]. Available: <http://stacks.iop.org/0031-9155/36/i=4/a=004>
- [121] A. Mabe, J. A. II, M. Urffer, S. Young, D. Penumadu, G. Schweitzer, and L.F. Miller, "Thin film polymer composite scintillators for thermal neutron detection," *Journal of Composites*, vol. 2013, no. 539060, April 2013.
- [122] *Range of Neutrons*. National Institute of Standards and Technology Center for Neutron Research. [Online]. Available: <http://www.ncnr.nist.gov/>
- [123] S. Glasstone and P. J. Dolan, *The Effects of Nuclear Weapons*. United States Department of Defense, 1977. [Online]. Available: <http://www.deepspace.ucsb.edu/wp-content/uploads/2013/01/Effects-of-Nuclear-Weapons-1977-3rd-edition-complete.pdf>
- [124] R. Nave, *Tritium Breeding*. Hyper Physics. [Online]. Available: <http://hyperphysics.phy-astr.gsu.edu/hbase/nucene/fusion.html>
- [125] Philips, "EM80 datasheet," 2007. [Online]. Available: <http://www.r-type.org/pdfs/em80.pdf>
- [126] Ortec, *Application note AN34: Energy Loss with Heavy Charged Particles*, 2006 revised 2012. [Online]. Available: www.ortec-online.com
- [127] N. I. of Standards and Technology, *ESTAR: stopping power and range tables for electrons*. [Online]. Available: <http://physics.nist.gov/PhysRefData/Star/Text/ESTAR.html>
- [128] J. Marsh, D. Thomas, and M. Burke, "High resolution measurements of neutron energy spectra from AmBe and AmB neutron sources," *Nuclear Instruments and Methods in Physics Research Section A: Accelerators, Spectrometers, Detectors and Associated Equipment*, vol. 366, no. 2-3, pp. 340 - 348, 1995. [Online]. Available: <http://www.sciencedirect.com/science/article/pii/0168900295006133>

Appendix A

Labview VIs

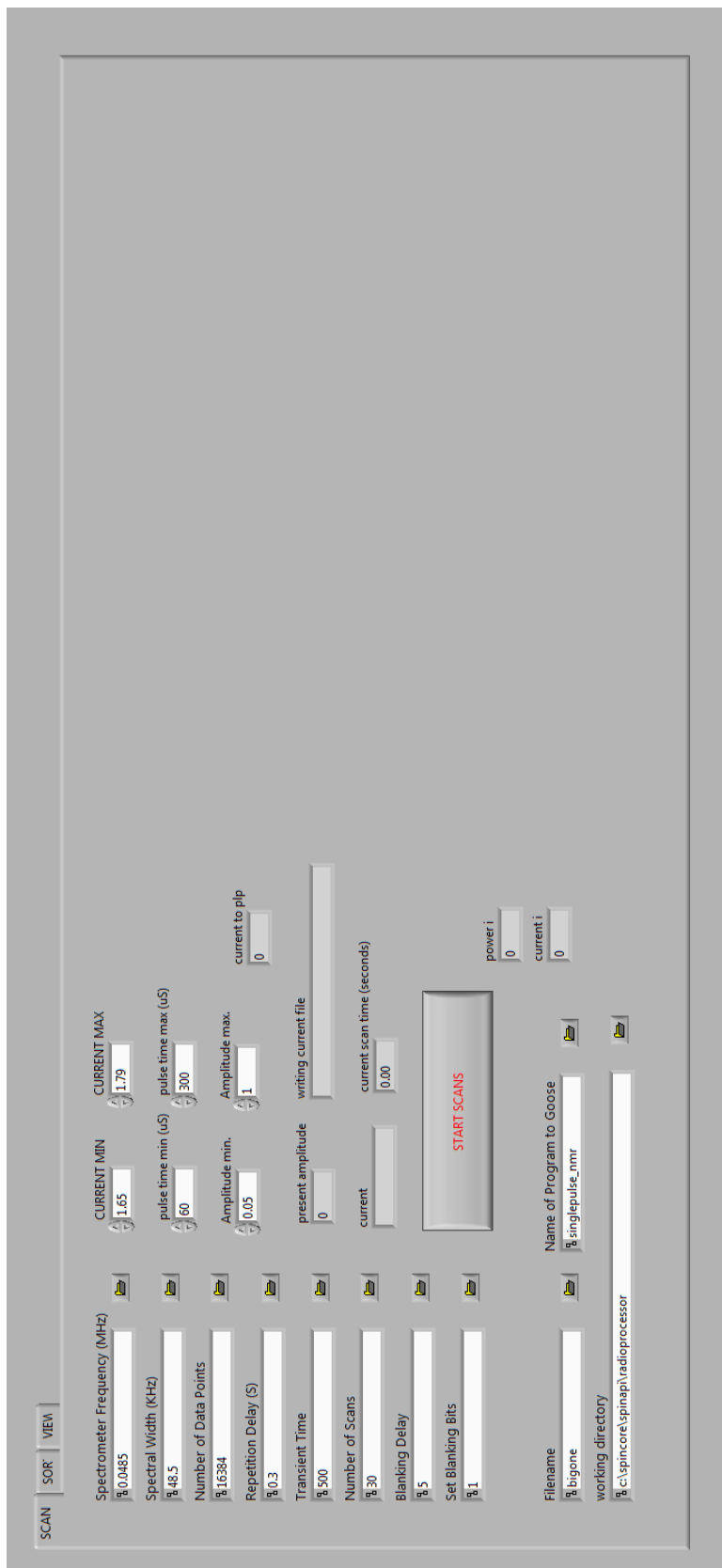


FIGURE A.1: Front view of the Labview VI designed to control the low-field NMR experiment. Section 1 of 3.

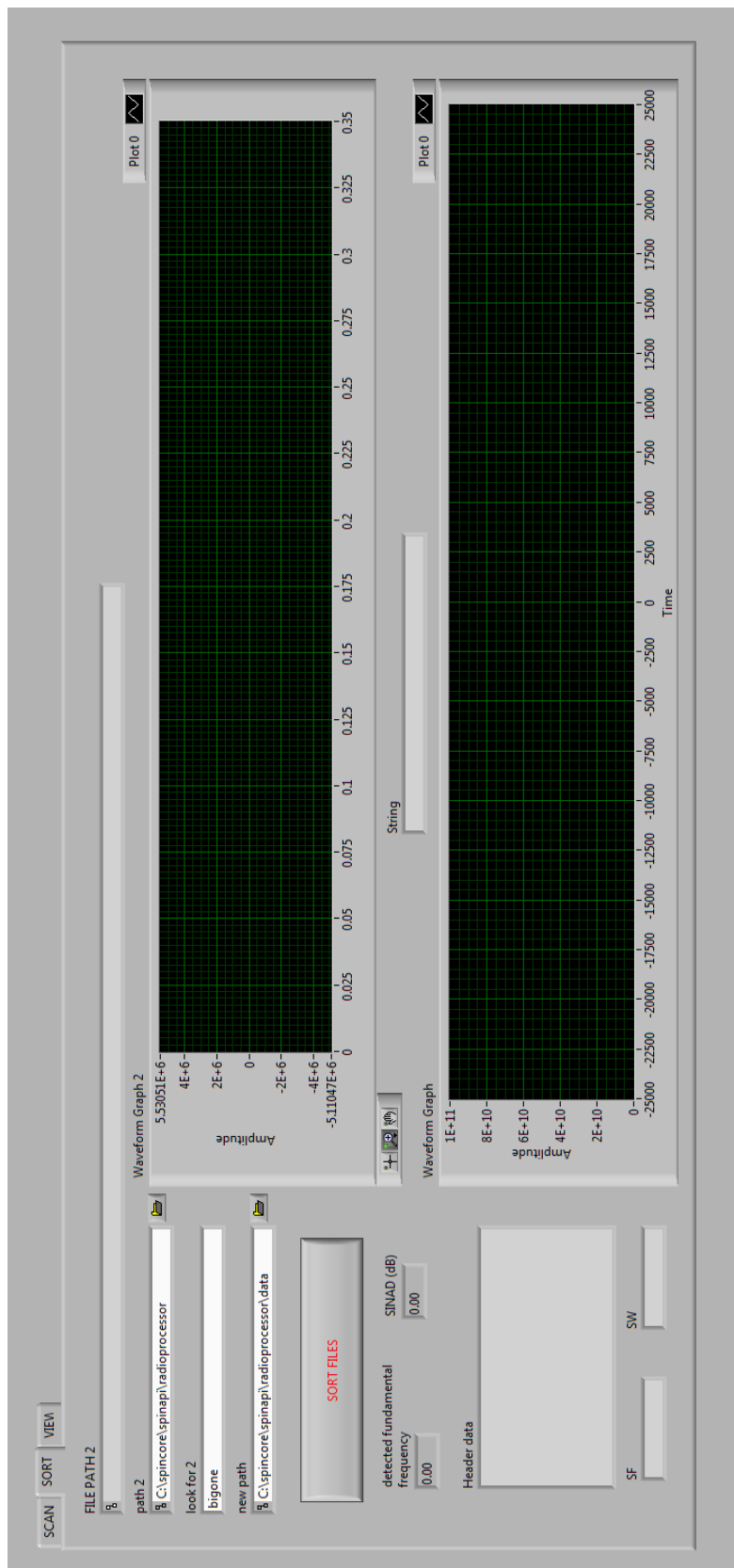


FIGURE A.2: Front view of the Labview VI designed to control the low-field NMR experiment. Section 2 of 3.

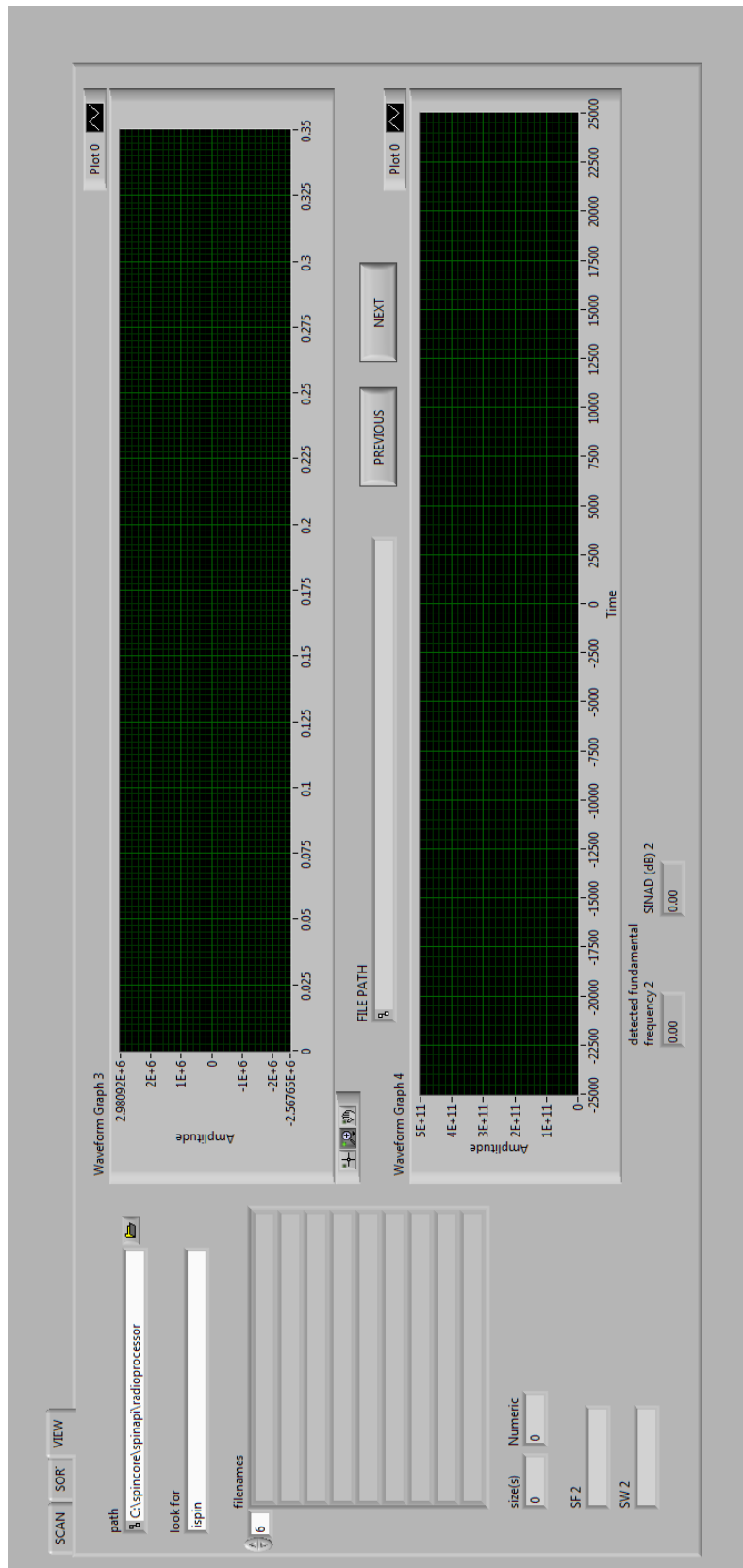


FIGURE A.3: Front view of the Labview VI designed to control the low-field NMR experiment. Section 3 of 3.

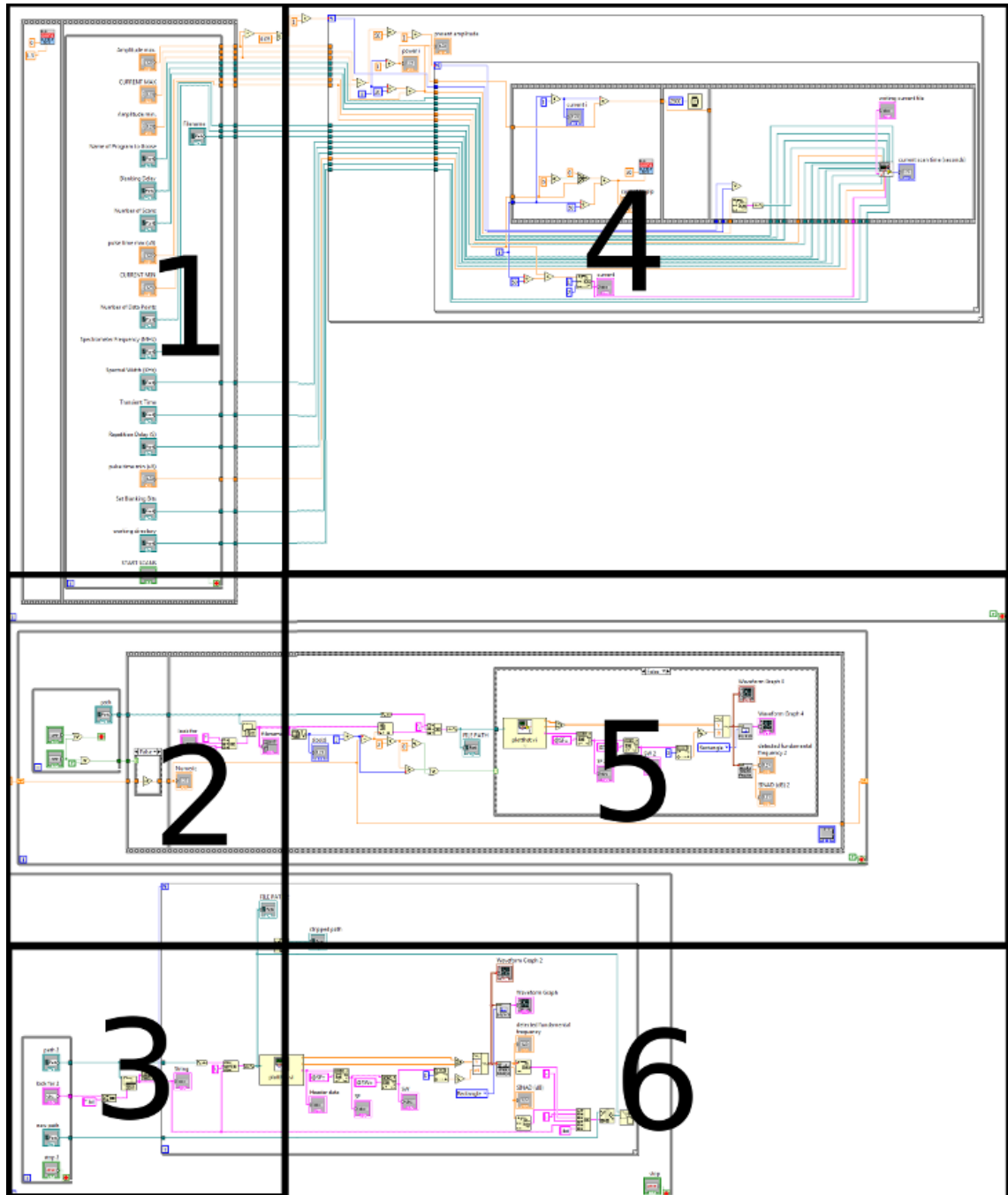


FIGURE A.4: Top shell of the Labview VI created to control the NMR experiment. Sections 1 to 6 are pictured in the next pages.

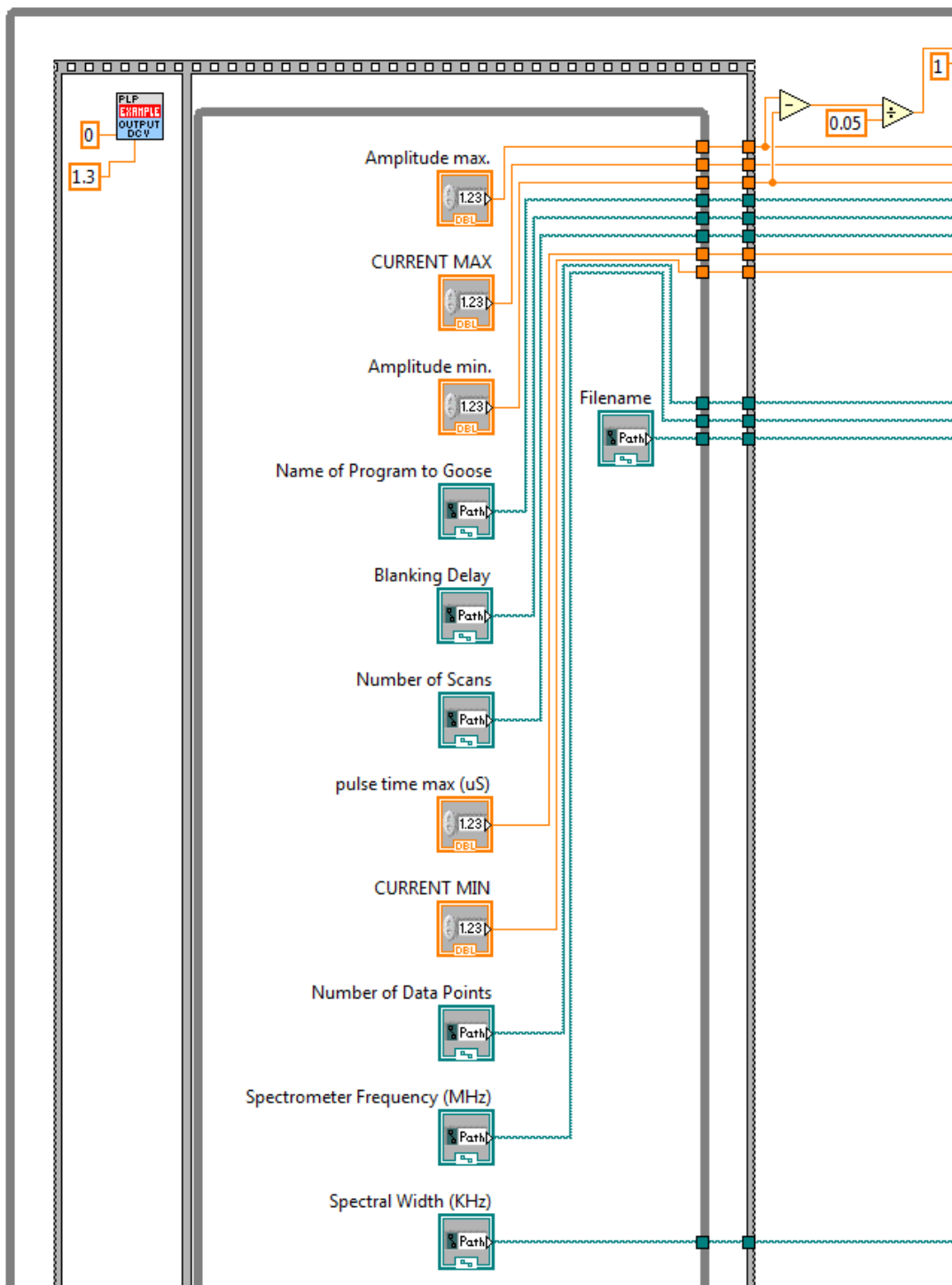


FIGURE A.5: Top shell of the Labview VI created to control the NMR experiment. Sections 1 of 6

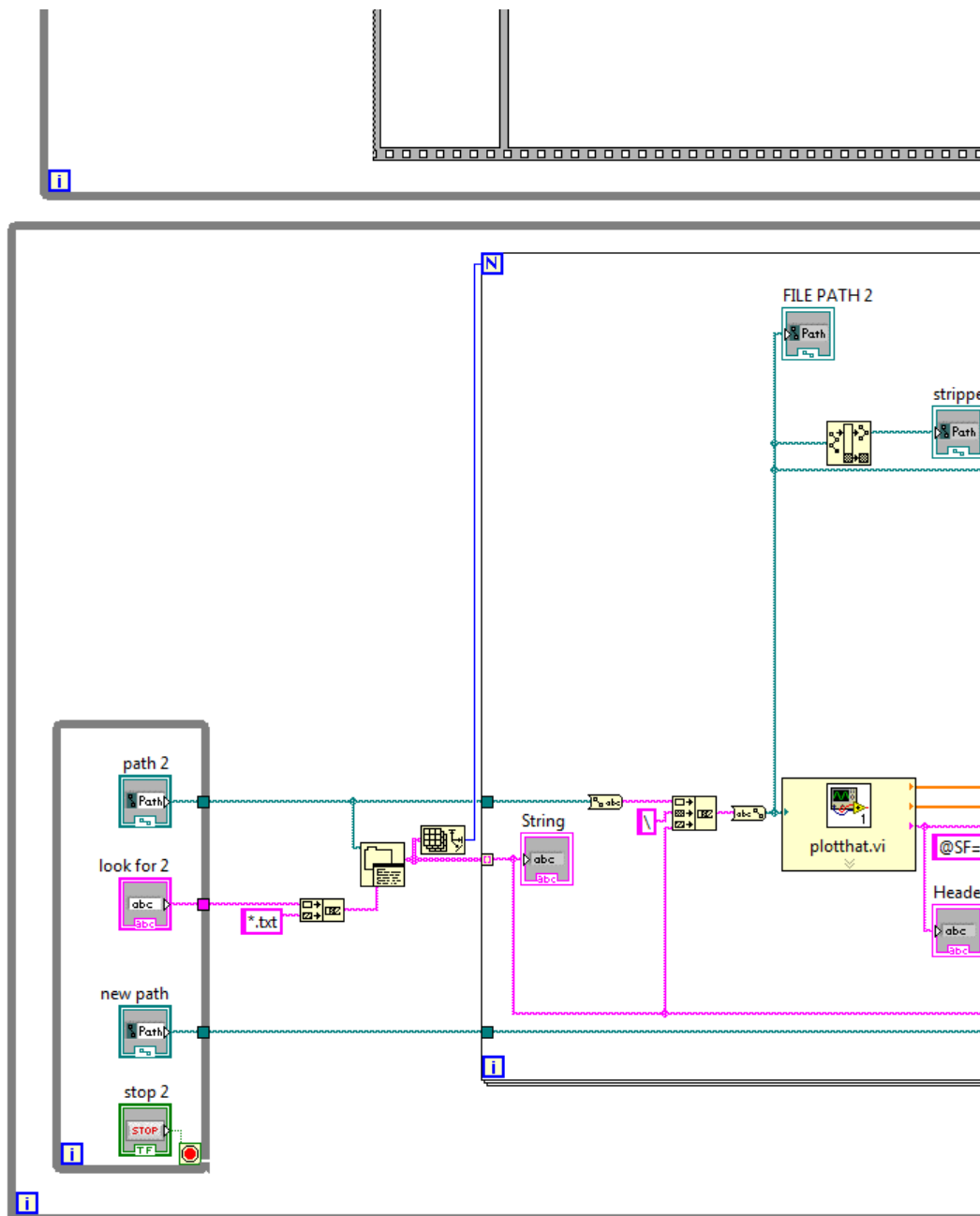


FIGURE A.7: Top shell of the Labview VI created to control the NMR experiment. Sections 3 of 6

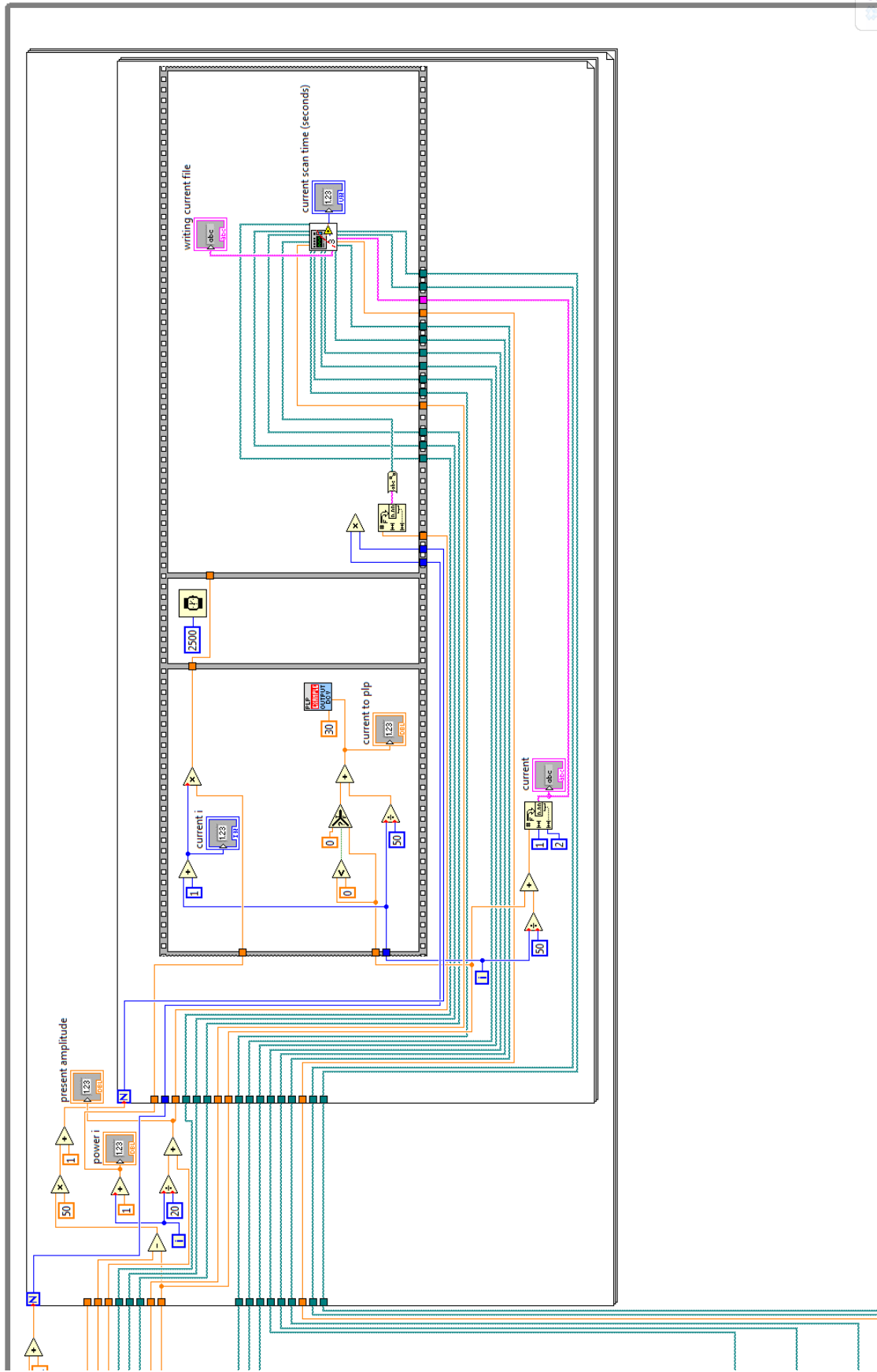


FIGURE A.8: Top shell of the Labview VI created to control the NMR experiment. Sections 4 of 6

Screenshots

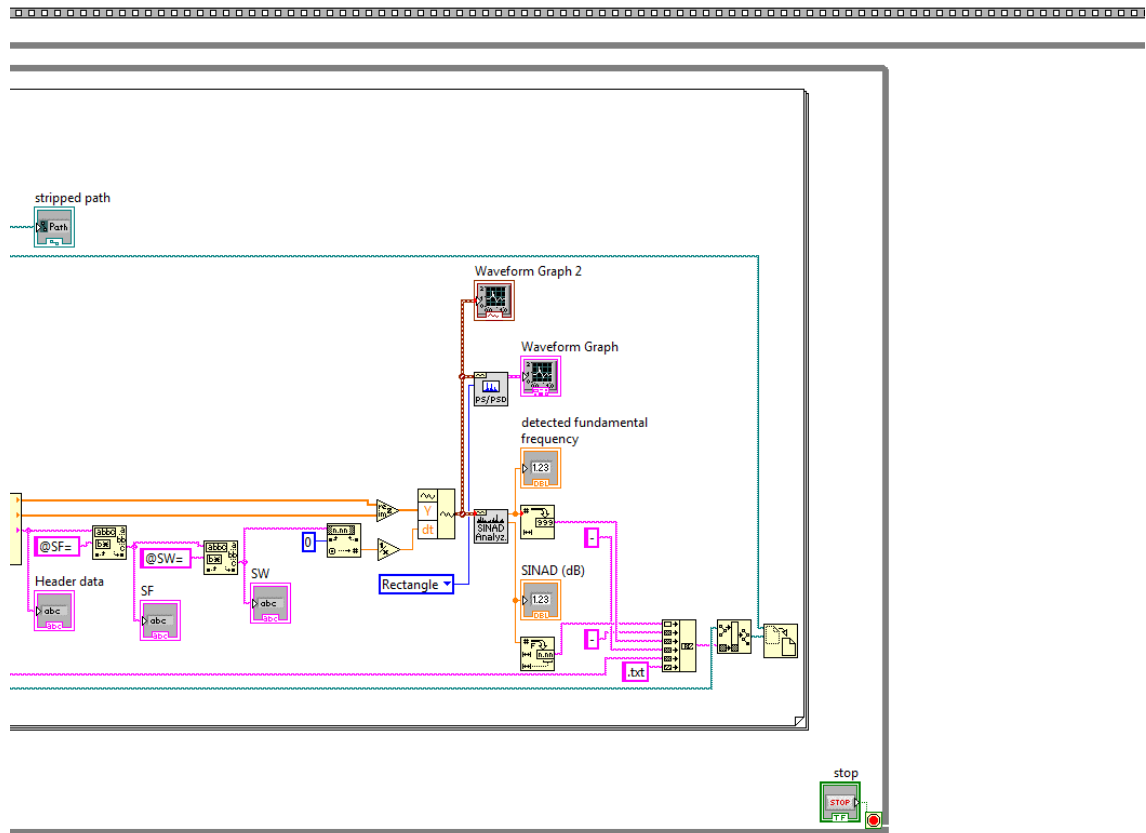


FIGURE A.10: Top shell of the Labview VI created to control the NMR experiment. Sections 6 of 6

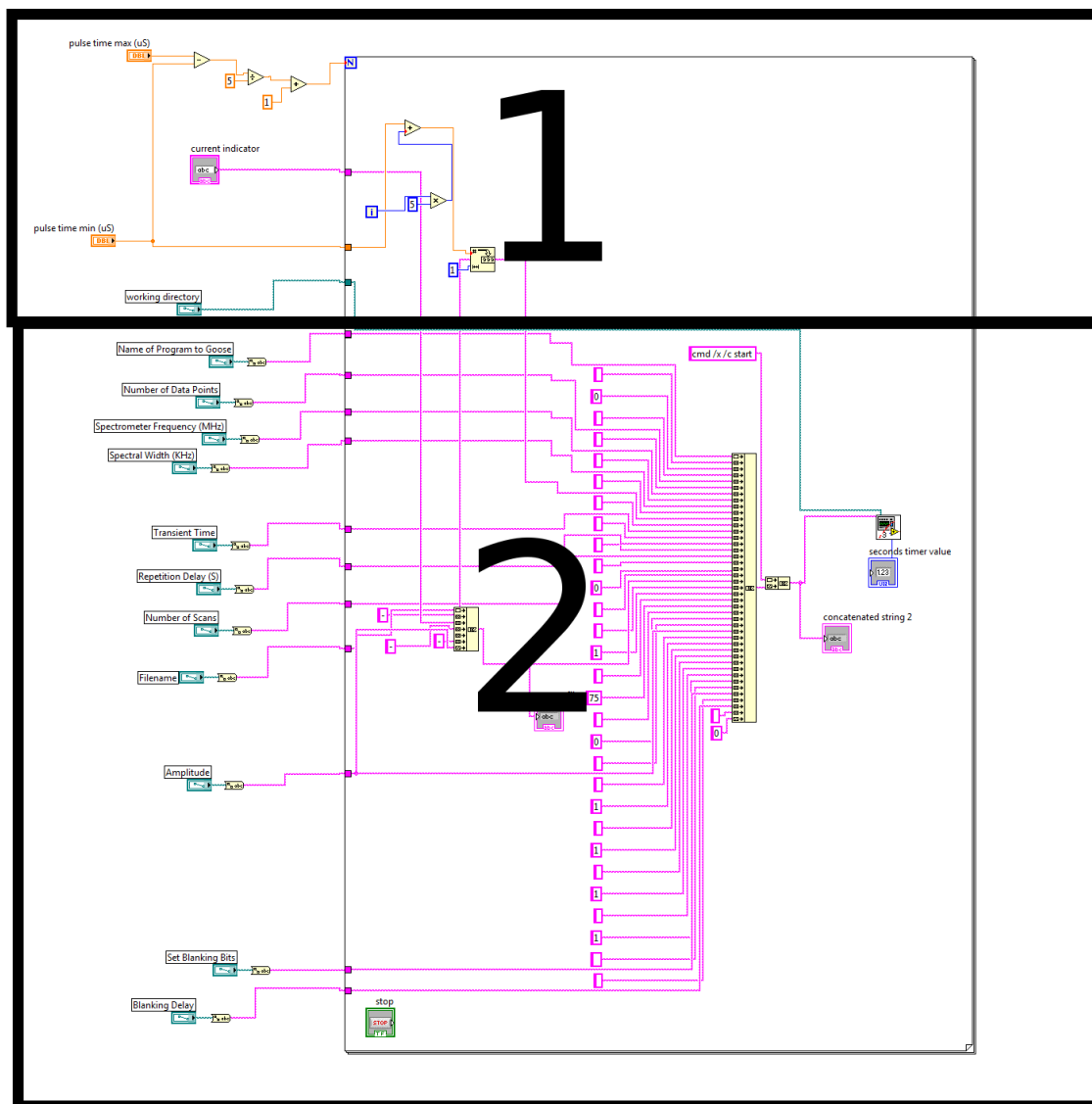


FIGURE A.11: Inner shell of the Labview VI designed to control the low-field NMR experiment. 1 and 2 are shown in the following pages

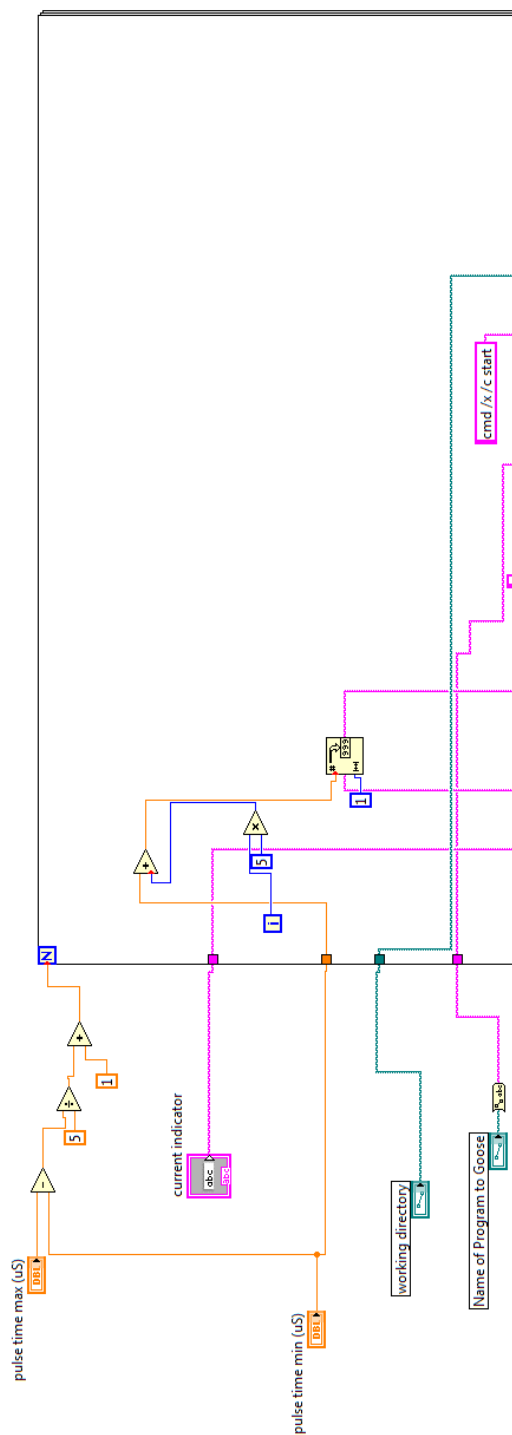


FIGURE A.12: Inner shell of the Labview VI designed to control the low-field NMR experiment. Section 1 of 2

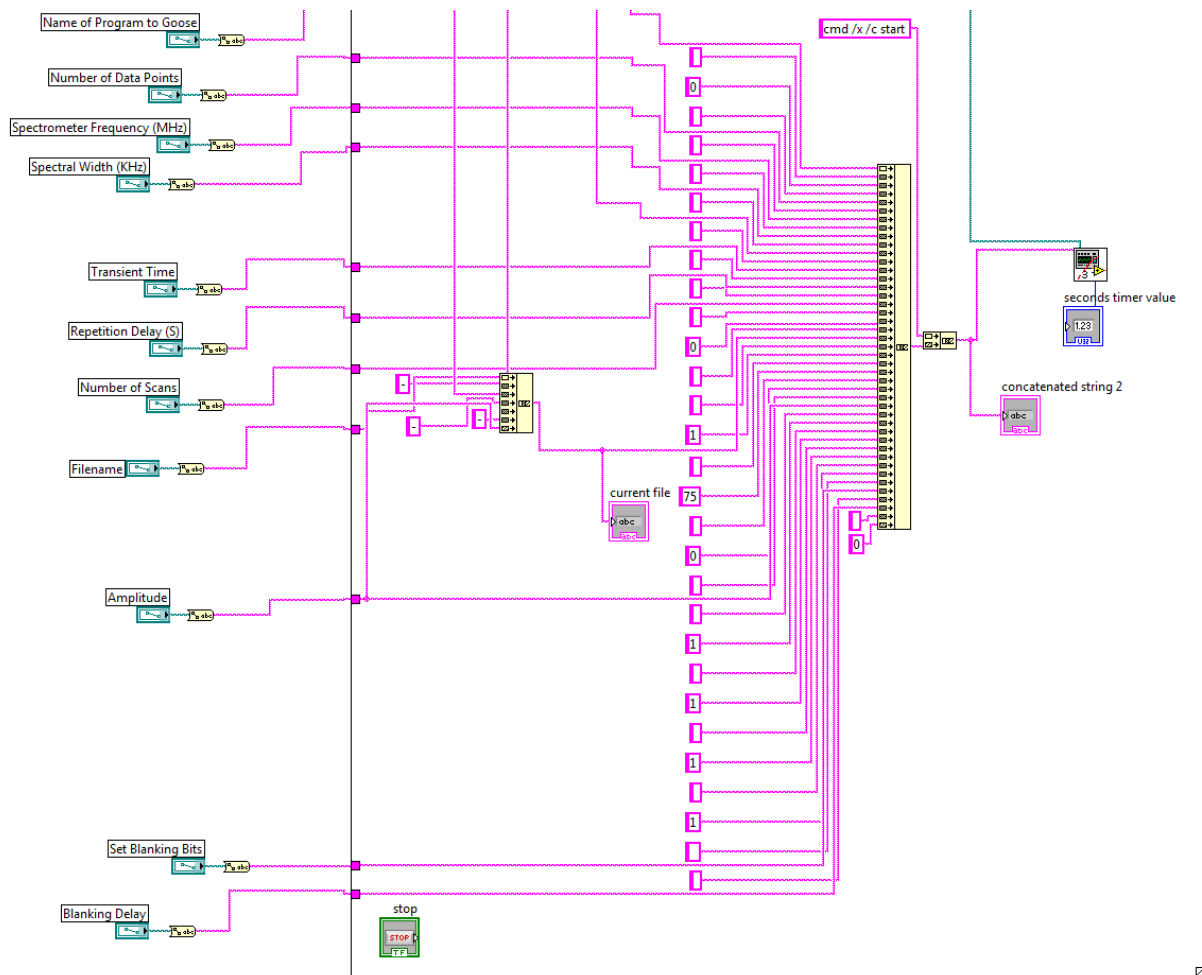


FIGURE A.13: Inner shell of the Labview VI designed to control the low-field NMR experiment. Section 2 of 2

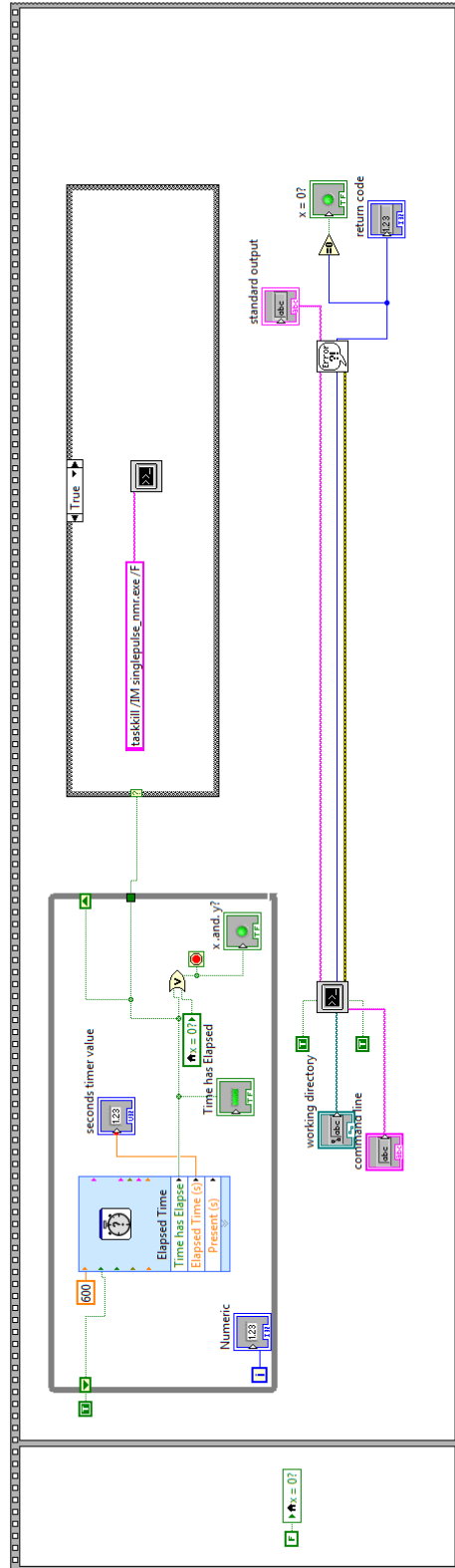


FIGURE A.14: Most inner shell of the Labview VI designed to control the low-field NMR experiment.

Appendix B

Start-Stop Oscillator Design

```

//include files*****
#include<avr/interrupt.h>
#include<avr/io.h>
#include<util/delay.h>
#include"portab_cv.h"

//function prototypes*****
void load_dac(void);
void initialize_ports(void); //initializes ports

//main program*****

#define MUX_EN SBIT(PORTC, 1)
#define DAC_LD SBIT(PORTE, 4)
#define DAC_CLK SBIT(PORTE, 2)
#define DAC_CS SBIT(PORTE, 1)
#define DAC_SDI SBIT(PORTE, 3)
#define DAC_CLR SBIT(PORTE, 5)

#define HIGH 0x01
#define LOW 0x00

//global variables
unsigned int sinetable[13] = {128,
187,
232,
254,
247,
212,
158,
97,
43,
8,
1,
23,
68
};

unsigned char countit;
void main(void)
{
initialize_ports();
while(1)
{
PORTD=0b10000000;
countit=0;
}
}
////////////////////////////////////
ISR(PCINT1_vect)
{
while (PINC^=0x01)
{
if (countit>12)
{
countit=0;
}
else
{
}

PORTD=sinetable[countit];
countit++;
}
}
void initialize_ports(void)
{
DDRE=0xff; // data direction = output
PORTB=0x00;

DDRC=0x00; //all pins on portc output except C0
PORTC=0x00;

DDRD=0xff;
PORTD=0x00;

TCCR0A=0b00000010;
TCCR0B=0x01;
SREG=0x01<<7;

PCICR=0x01<<1;
PCIFR=0x01<<1;
PCMSK1=0x01;

countit=0;
}

```

FIGURE B.1: Start stop oscillator program. Built on an Atmel328p to test the function of the ispin averaging.

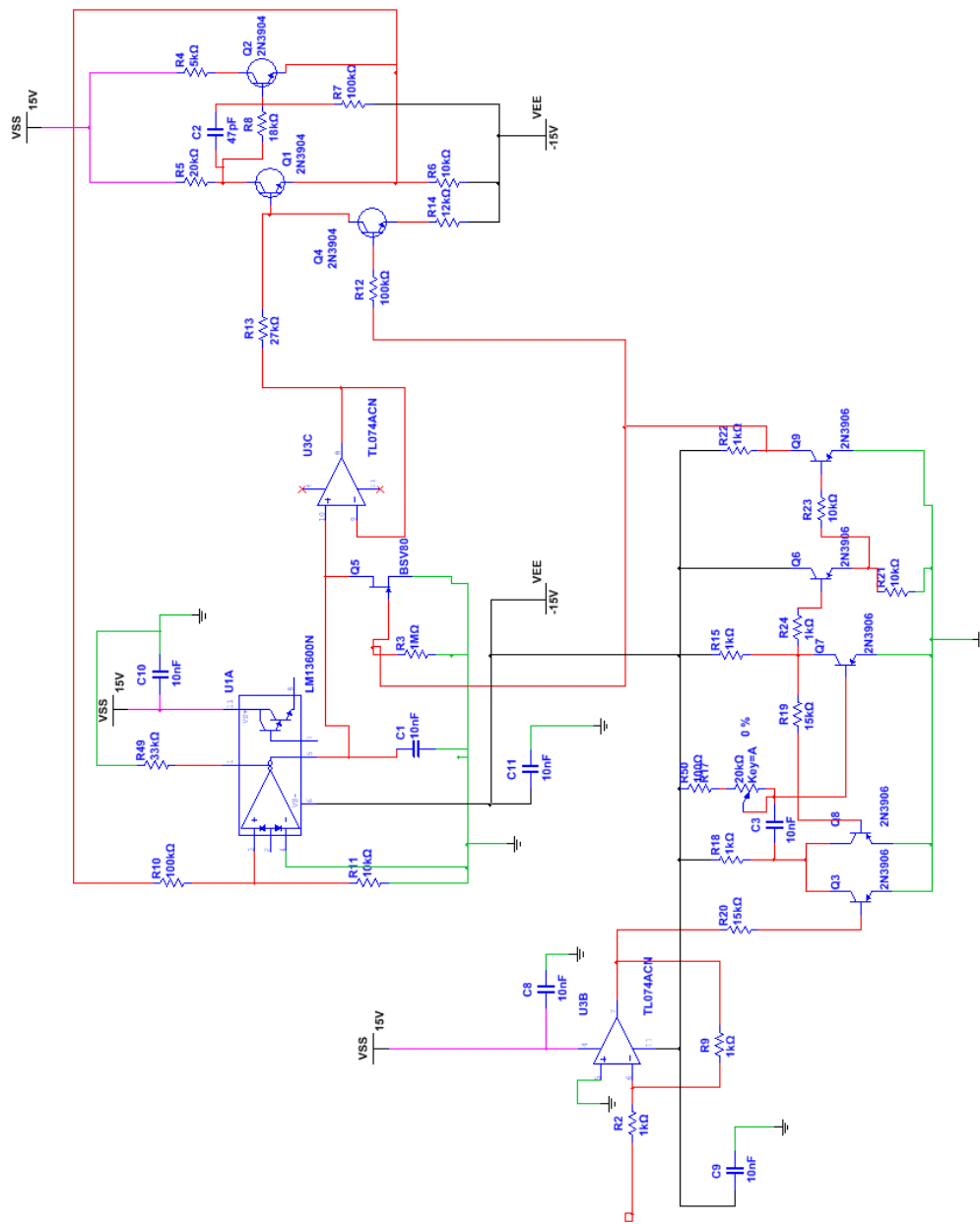


FIGURE B.2: Start stop oscillator schematic. Built on an Atmel328p to test the function of the ispin averaging.